Ph.D. Dissertation of Engineering

A Study on a Frequency Domain Approach for Fatigue Analysis of Wide-banded Non-Gaussian Processes

비정규 광대역 과정에 대한 주파수 영역 피로 해석 기법에 관한 연구

August 2019

Graduate School of Engineering
Seoul National University
Naval Architecture & Ocean Engineering

Hyeon-jin Kim

A Study on a Frequency Domain Approach for Fatigue Analysis of Wide-banded Non-Gaussian Processes

비정규 광대역 과정에 대한 주파수 영역 피로 해석 기법에 관한 연구

지도교수 장 범 선

이 논문을 공학박사 학위논문으로 제출함

2019년 7월

서울대학교 대학원

조선해양공학과

김 현 진

김현진의 공학박사 학위논문을 인준함

2019년 7월

위 원 장	노 명일	(인)
부위원장	장 범선	(인)
위 원	김 유일	(인)
위 원	박 준범	(인)
위 원	박 태윤	(인)

Abstract

Ships and offshore structures are cyclically exposed to various environmental loads induced by wind, wave and current during its entire life. Even though internal stress due to the loads does not reach yield stress of material, the structures are damaged by the cyclic load and it might result in fatigue failure. Unlike ultimate limit state analysis considering only extreme a load case, all environmental conditions occurring design life should be considered in fatigue limit state (FLS) analysis so it requires huge amount of computational costs. Spectral fatigue analysis based on frequency domain has been widely utilized to more efficiently predict fatigue life of products.

Spectral analysis evaluates a probability density function of stress amplitude as a function of spectral moments and predict fatigue life of structures by utilizing it. In many practices, hot spot stresses are modelled as narrow-banded Gaussian process and under this assumption, the probability density function follows the Rayleigh distribution. However, there are just few structural responses which satisfy this assumption actually due to nonlinear load, multiple excitation and geometry complexity. Many fatigue analysis methods in frequency domain for wide-banded Gaussian process were developed to evaluate fatigue damages and approximate marginal distribution of stress amplitude. Some of them could predict fatigue damages with great accuracy in wide-banded Gaussian problem.

Non-normality is another important factor in fatigue analysis. Transformation technique which defines the relation between non-Gaussian and the underlying Gaussian random process has been studied to extend the approximation models derived in Gaussian random process to non-Gaussian problem. However, it requires complete information of cycle distribution such as a joint distribution of stress mean and amplitude, only few models derived in Gaussian random process could be used to analyze non-Gaussian random process. Moreover, the existing approximate models for joint distribution of stress cycles seems to give inaccurate results or require multi-dimensional integration to get the cycle distribution.

In this present work, an approximate model for conditional probability density function of stress mean given amplitude in wide-banded Gaussian process is proposed. This model is combine with the existing three models for marginal distribution of stress amplitude to get the joint distribution of stress mean and amplitude. The accuracy of proposed joint distribution is verified by numerical simulation for engineering critical assessment on TLP tendons

The proposed joint distribution is extend to non-Gaussian region through Hermite function. The accuracy of the proposed model in prediction on fatigue damages due to non-Gaussian loadings is verified in various conditions having different bandwidth and non-Gaussian values. In addition, to examine the applicability of the model in the real engineering problem, the fatigue analyses for the typical nonlinear problems, wind and Morison loads, are performed. Particularly, in the numerical example of Morison load, the effect of

non-normality on fatigue damage is discussed through comparison with the linearization coefficient approach. Although the accuracy of the proposed model is dependent on the selection of approximate model marginal distribution of stress amplitude, it is verified that the proposed model can improve the fatigue analysis results in wide-band non-Gaussian problems.

Keyword : fatigue analysis, joint probability density function, random process, power spectrum, Hermite function, non-normality, bandwidth effect

Student Number : 2014-30334

List of Contents

List of Figures

List of Tables

NOMENCLATURE

BT	: Benasciutti−Tovo
DK	: Dirlik
IF	: irregularity factor
JB	: Jum−Beom
LCC	: level−crossing counting
RC	: range counting
RFC	: rainflow counting
WL	: Wirsching−Light
a	: crack depth [mm]
$a(z,t)$	: particle acceleration
$a'(z,t)$	: particle acceleration in intermittent flow
b	: normalized observation height $(= h/\sigma_\eta)$
$b_{\mathrm{app}}^{\mathrm{Tovo}}, b_{\mathrm{app}}^{\mathrm{BT}}$	: weighting factor
c	: crack length [mm]
$D(T)$	: fatigue damage in time period T
$\overline{D}$	: expected damage intensity
f_m	: reduction factor for mean stress correction
F_l	: linearized Morison force
F_P	: force maxima
$G(\cdot)$	: transformation function between Gaussian and non−Gaussian processes
h	: observation height
$h(u,v)$	: joint probability density function of counted cycles as function of peak and valley
$H(u,v)$	: cumulative distribution of counted cycles as function of peak and valley

K	: stress intensity factor
K_{op}	: stress intensity factor at which crack opens
$\bar{K}_D$	: Linearization coefficient $(= K_d\beta)$
ΔK	: stress intensity factor range
ΔK_{ef}	: effective stress intensity factor range
m	: stress mean [MPa]
$N_T(u,v)$	: count distribution
$N(T)$	: number of cycles counted in time period T
$p_m(m)$	: marginal distribution of mean
$p_{m\|s}(m\|s)$	: conditional probability density function of mean
$p_s(s)$	: marginal distribution of amplitude
$p_{s,m}(s,m)$	: joint probability distribution of mean and amplitude
$P_p(u)$	: probability density function of peaks in Gaussian process
$P_v(v)$	: probability density function of valleys in Gaussian process
r	: stress range [MPa]
R	: stress ratio
s	: stress amplitude [MPa]
s_{eff}	: effective stress amplitude [MPa]
T	: time period
u	: peak of counted cycle
$u(z,t)$	: particle velocity
$u'(z,t)$	: particle velocity in intermittent flow
U	: ratio of effective stress intensity factor range to stress intensity factor range
v	: valley of counted cycle

v_0	: mean−upcrossing rate
v_p	: mean number of peaks
$X(t), Z(t)$	: random processes (Gaussian and non−Gaussian processes)
α_i	: ith bandwidth parameters for process $X(t)$
β	: Borgman linearization coefficient
β_i	: ith bandwidth parameters for derivative process $\dot{X}(t)$
γ_3, γ_4	: skewness, kurtosis
$\Gamma(\cdot)$	: gamma function
$\theta_1, \theta_2, \theta_3$	: shape parameters of logit−log model
$\eta(\mathrm{x}, \mathrm{t})$	: surface elevation
$\mu_T(u, v)$	: expected count distribution
σ_a	: standard deviation of particle acceleration
σ_c	: maximum compression stress
σ_e	: endurance limit [MPa]
$\sigma_{m\|s}$	: standard deviation of conditional probability density function of mean
σ_t	: maximum tension stress
σ_u	: standard deviation of particle velocity
σ_{ut}	: ultimate strength [MPa]
σ_X, σ_Z	: standard deviation of a random process $X(t), Z(t)$
σ_η	: standard deviation of wave elevation

Chapter 1. Introduction

1.1. Study Background

Ships and offshores structures are exposed cyclically to various environmental loads like wave, wind and current during its service life. Even though structural responses induced by such loads do not reach a limit state of material, these structures get damaged by these cyclic loads and might be destroyed when cumulative damage reaches one. This structural failure is defined as fatigue failure. It is very important to secure enough fatigue life in design stage due to high cost on maintenance and repair of ships and offshore structures so very accurate and efficient fatigue analysis procedure is required.

Fatigue damage is defined as a function of stress amplitude, the number of each stress cycle and some material constants. The first step of fatigue analysis is calculating the fatigue damage of each stress cycle. Then, damage accumulation rule is applied to sum the damage of each cycle. There are various cycle counting methods and damage accumulation rules. In general, rainflow counting method and Palmgren-Miner's linear damage rule have been widely used in most industries [Dowling (1972)].

The information of stress cycles such as stress amplitude and the number of cycles could be extracted directly from stress time history by cycle counting method or calculated by probability density function of stress cycles. The former is called time domain approach [Newland (1984), Lee et al (2005)]. Time history of stress is usually

calculated from CAE simulations and can also be obtained by experiments. Depending on performance of solver in CAE, time domain approach could reflect nonlinearity from coupling effect or geometrical complex. However, it takes too much time to calculate the time series data per one load case, it is not possible to consider all environmental load cases in time domain. Many studies have proposed supportive measures to reduce computational cost and time by excluding insignificant load cases or reducing the number of simulation and duration of each simulation [Mohammadi et al (2016), Peng et al (2017)].

The frequency domain approach defines probability density function of stress cycles and calculates the information of stress cycles from it. If time history of stress follows stationary narrow-banded Gaussian process, it has been known that the probability density function of stress amplitude could be assumed the Rayleigh distribution [Houston and Skopiniski (1956)]. This assumption has been widely accepted with linear wave theory and linear structural analysis. However, in real engineering problem, most of structural responses are non-stationary wide-banded non-Gaussian processes. When multiple excitations simultaneously act on offshore structures such as TLP tendon or mooring line, the frequency components of each loads should be reflected in the structural responses so they are wide-banded processes rather than narrow-banded processes [Ochi (1986), Zou et al (1999), Gao and Moan (2007)]. Also, when the effect of nonlinear loads such as Morison and wind load are significant, structural responses seem to follow

non-Gaussian process [Kanegaokar and Haldar (1987), Jensen (1990), Spidsoe and Karunakaran (1997), Gong and Chen (2014), Ding and Chen (2014, 2015), Schottler et al (2017)]. Storm might occur during operation and the statistical properties of structural responses could be significantly changed before and after storm [Morandi et al (2004)]. Like these various situations, it is necessary to deal with non-stationary wide-banded non-Gaussian process in real engineering problems.

Many studied have been performed to modify the limitations on the spectral analysis. Most of them tried to extend the results derived in narrow-banded Gaussian processes. When hot spot stress is wide-banded process, probability density function of stress amplitude is no longer Rayleigh distribution. Rychlik (1993) proved that application of narrow-band assumption on wide-banded processes tend to overestimate the rainflow fatigue damage.

In 1980s, a correction factor was introduced to reflect the effect of bandwidth on fatigue damage and the fatigue damage was expressed as the product of the correction factor and predicted fatigue damage based on the narrow-band assumption [Wirsching and Light (1980), Lutes and Larsen(1990)]. This models were very simple and easy to use but the predicted fatigue damages deviated from time simulation results and they did not give any information of stress cycle distribution. Dirlik (1985) proposed an alternative model on marginal distribution of stress amplitude for wide-banded Gaussian processes. It was constructed by vast amount of simulation results and consisted of three different distribution function. Other

researchers have also suggested their own approximate functions to modify the Dirlik's model [Zhao and Baker (1992), Petrucci and Zuccarello (2004), Park et al (2014)]. Although some of them predicted fatigue damages including bandwidth effect with certain accuracy, their works could be limitedly used in only Gaussian process. Benasciutti and Tovo (2005) proposed an approximate model on joint probability density function of stress mean and amplitude to express whole information of cycle distribution in wide-banded Gaussian process. They also introduced transformation function which linked non-Gaussian and Gaussian process to extend their work derived in Gaussian process to non-Gaussian problem. As another way to predict the joint distribution function, the Markov method was devised by Frendhal and Rychlik (1993). It assumed that a sequence of turning points followed Markov process. By calculating a transition probabilities from maximum to the following minimum, it could predict the joint distribution of peak and valley of rainflow-counted stress cycles.

Non-Gaussianity is another important factor which has a significant effect on fatigue damage and its effect has been reviewed by many researchers [Rizzi et al (2011), Kihm et al (2013)]. Sarkani et al (1994) warned that spectral analysis technique based on the Gaussian assumption might significantly underestimate probability of high amplitude cycles. The models for handling non-Gaussianity in frequency domain have been developed by utilizing the approximate models derived in Gaussian process. Some literatures addressed how to handle non-normality in frequency domain and suggested

analytical estimation formula which were based on the extension of the narrow-banded assumption [Winterstein (1985, 1988), Winterstein et al (1994), Kihl et al (1995)]. Thereafter, a number of studies have been carried out on the transformation function that converts a Gaussian processes into non-Gaussian processes with equivalent first and second moments [Lawrence and Lewis (1985), Grigoriu (1995)]. Based on this, a framework for analyzing a wide-banded non-Gaussian process in the frequency domain has been established. Recently, correction factors considering non-Gaussianity have been studied based on kurtosis control simulation technique [Braccesi et al (2009), Cianetti et al (2018)].

As described above, many models for a wide-banded non-Gaussian process have been developed approximately or theoretically, and a precise model derived in Gaussian process is required as the basis of these methods. Information about the whole cycle distribution is needed to extend the results to non-Gaussian processes through the transform function, but only few models provide it. The approximate model for joint probability distribution function might also provide distorted information about stress mean, and it can result in significant errors in evaluation on fatigue damages for non-Gaussian processes. That is, to increase the accuracy of the fatigue analysis result for non-Gaussian process, it is necessary to accurately estimate the joint probability density function of stress mean and amplitude in Gaussian process.

1.2. Purpose of Research

The purpose of this study is to propose an approximate model for joint probability distribution function of stress mean and amplitude in Gaussian process. The proposed model needs to be given in explicit form to eliminate additional computational cost. This model could be utilized to engineering critical analysis (ECA) which requires stress cycle distribution and to fatigue analysis on wide-banded non-Gaussian processes with transformation technique. Especially, this model concentrates on describing conditional probability density function of stress mean given amplitude so it is expected that this mode could increase the accuracy of spectral analysis in non-Gaussian process problem.

There are two different approaches to assess fatigue life of structures. The first one is traditional S-N curve based approach and the other one is fracture mechanics based approach. Recently, in case of TLP tendons or topside structures, many ship owners have required ECA results. Chapter 2 addresses about the basics and detail procedure of two approaches. The fatigue analysis is basically performed by predicting the probability density function of stress cycles extracted from time series data by cycle counting method. Chapter 2 also introduces several cycle counting methods.

The bandwidth effect on fatigue damage in Gaussian process has been studied and many approximate models have been also proposed. In this present work, an approximate model of joint probability density function of stress mean and amplitude is proposed by

combining existing models for stress amplitude and newly proposed model for conditional probability function of stress mean. Therefore, the details of the existing models should be understood in advance. In chapter 3, brief description of some models for wide-banded Gaussian processes is addressed.

The detailed procedure for deriving the conditional probability density function of stress mean is explained in chapter 4. It is assumed that the conditional probability density model of stress mean follows zero-mean normal distribution. The only unknown variable is standard deviation and regression analysis is performed to approximate the unknown value. The results of sensitivity analysis to find input variables and nonlinear regression analysis to determine the explicit formula for standard deviation are discussed in this chapter.

The reason that probability density functions derived in Gaussian process is important is that it could be extended to non-Gaussian problem through transformation technique. In chapter 5, the detailed information of transformation function is explained and how to extend probability models derived in Gaussian process to non-Gaussian problem. The new model is applied to fatigue analysis on non-Gaussian time signal generated considering various 3rd and 4th statistical moments and joint probability density functions in non-Gaussian process calculated by the existing and new model are compared.

Two numerical examples are introduced to verify the accuracy and applicability of the proposed model in chapter 6. The proposed

model is applied in fatigue crack growth analysis on TLP tendon. In fatigue crack growth analysis, stress ratio R of each stress cycle is required to reflect crack closure effect on crack growth rate. The stress ratio R is the ratio of peak to valley in stress cycles so joint distribution of stress cycles should be needed to obtain the R values of each cycle. The predicted crack growth results by existing and newly proposed models are compared. The other example is a fatigue analysis on offshore wind turbine structures. The time series of stress at tower base are calculated by fully coupled analysis considering wind and wave loads. The fatigues damage at tower base are predicted by both time and frequency domain approaches.

Morison equation consists of two force term. First one is drag force and the other is inertia force. Because drag force is proportional to the square of particle velocity, Morison equation is known as a nonlinear force. A linearization coefficient which aims to linearize the nonlinear drag term in Morison equation was proposed by Borgman (1967) to evaluate directly Morison force spectrum from velocity and acceleration spectra. In linear wave theory, particle velocity and acceleration are assumed to be Gaussian process so the linearized Morison force is also Gaussian process so the fatigue damage results could not consider the non-normality. In chapter 7, fatigue analyses on fixed cylinder under Morison force are performed by proposed model considering non-normality and spectral analysis through the linearization coefficient. By comparing the results, the effect of non-normality on fatigue damages is discussed.

Chapter 2. Basics of fatigue analysis

2.1. S-N curve based fatigue analysis

The mechanism of fatigue failure is related to initial crack growth. Inherent small crack (micro crack) in metal surface propagates as the crack opens and closes due to cyclic loading. Several small crack can meet each other to form macro crack. Many metallurgical factor such as microscopic non homogeneity or grain structure, stress concentration due to geometry and welding have been knowns as important factors when predicting crack propagation phenomenon. The analytical models for understanding fundamental microscopic aspect of crack propagation has been studied for a long time, however, there is no quantitative ways to predict fatigue life of material in microscopic scale. This means that the process of initiation of micro cracks that finally will form macroscopic cracks in the material is not accounted for in detail in the analytical model,

Laboratory experiments have been tried to quantify fatigue damage induced by constant amplitude loadings. Wohler (1870) summarized vast amount of experimental data about railroad axles and he emphasized on the importance of stress range not peak value and the concept of endurance limits. Basquin (1910) proposed a log-log relationship called S-N curve using Wohler' s test data. The S-N curve in Eq. (2.1) is a plot of alternating stress S versus cycles to failure N. The most common procedure for generating the S-N data is constant amplitude test. It was the standard fatigue design method

for a long time and some classifications serve their own S−N curve data in regulations. Fig. 1 shows an example of S−N curve data in DNV−RP−C203. Based on the S−N curve, it is possible to calculate the fatigue damage of each stress cycle with specific stress range.

$$\log N = \log \bar{a} - \mathrm{m}\log(\Delta\sigma) \tag{2.1}$$

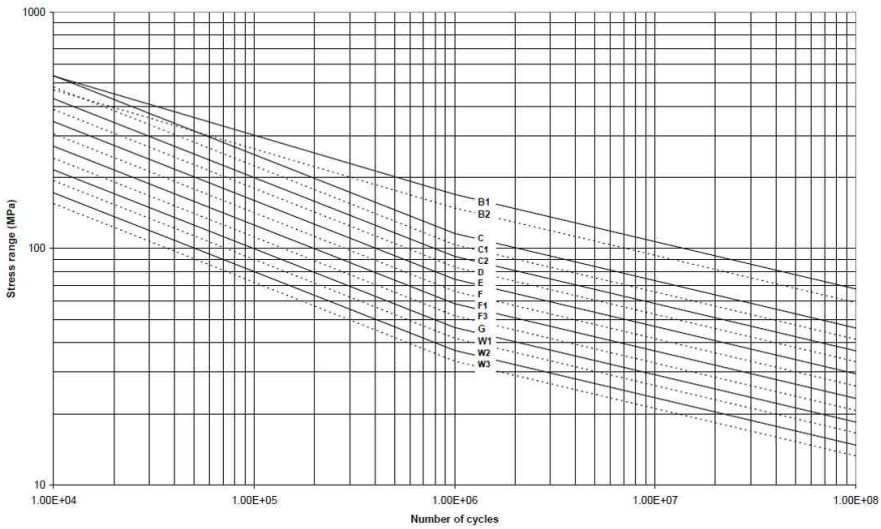

Fig. 1 S−N curves in sea water with cathodic protection [DNV (2011)]

Mean stress is another important factor which has an effect on fatigue damage. Mean stress is equal to the average of the maximum and minimum stress during a fatigue load cycle. Much of fatigue data is generated assuming a zero mean stress, which means that the load cycle is completely reversed. The stress ratio, also referred to as R, is defined as the minimum stress over the maximum stress and is used to quantify the mean stress. A stress ratio of −1 represents a fully reversed loading. However, fully reversed loading is rarely

observed in engineering practice and the mean stress may not be non−zero in most cases. The best way to consider the effect of mean stress is making S−N curve with non−zero stress ratio value but it requires too much cost and time. Some diagram which plotted alternating stress versus mean stress have been proposed and Dowling (2004) reviewed several diagrams [Goodman (1919), Morrow (1968), Smith et al (1970), Walker (1970)]. Modified Goodman equation shown in Eq. (2.2) and Fig. 2 is a famous formula to describe the relationship between them.

$$\frac{s}{\sigma_e} + \frac{m}{\sigma_u} = 1 \tag{2.2}$$

where, $\mathrm{s: stress\ \ amplitude, m: stress\ \ mean}, \sigma_u\mathrm{: ultimate\ \ strength}$

$\sigma_e\mathrm{: endurance\ \ limit}$

Other factor such as size, type of loading, surface finish, surface treatments, temperature and environment should be considered in fatigue analysis [Bannantine et al (1990)]. Their effects on fatigue damages were reflection in form of modifying factor in alternative stress amplitude.

In real practice, time series of stress is irregular random processes. Fatigue damages of various amplitude stress cycles could be calculated by the S−N based approach but there is no information about summing fatigue damages of each cycles in the methods. Damage accumulation rules which aim to sum up each fatigue damage of stress cycle with different stress amplitude have been developed. Fatemi and Yang (1998) reviewed various damage accumulation

rules and grouped them into six categories: linear damage rule; nonlinear damage curve and two-stage linearization approaches; life curve modification methods; approaches based on crack growth concepts; continuum damage mechanics models; and energy-based theories. The linear damage summation rule was proposed by Miner (1945). He suggested that total fatigue damage of an irregular random loading could be expressed by just summing up all fatigue damages of each stress cycle. Although this method has some deficiencies such as load-level independence, load-sequence independence and lack of load-interaction accountability, this method has been dominantly used in design due to its simplicity. Finally, total fatigue damage based on S-N curve based approach is expressed as a function of stress range (or amplitude), the number of cycles and constants of S-N curves shown in Eq. (2.3).

$$D = \sum_{i=1}^{n} D_i = \sum_{i=1}^{n} \frac{n_i}{N_i} = \sum_{i=1}^{n} \frac{n_i}{\bar{a}} (\Delta\sigma_i)^m \tag{2.3}$$

2.2. Fracture mechanics based fatigue analysis

Another point of view in assessment of fatigue failure is the fracture mechanics based fatigue analysis. A material fracture when applied stress at crack tip reaches enough level to break the bonds that hold material atoms together. The strength of bond is induced by the attractive forces between atoms. Thus, depending on the relationship between applied stress at crack tip and strength of bond,

inherent crack will propagate or not.

Griffith (1920) proposed an idea that a flaw in material will propagate if the total energy of the system is lowered with crack propagation based on the principle of minimum total potential energy. In other words, when the energy required to make new crack in material is lower than to crack propagation, the crack will be extended. Irwin (1948) extended Griffith's theory to ductile materials. He explained that plastic deformation should be considered in energy calculation and even it is more dominant than surface energy term for ductile materials. The strain energy release rate, G, which is the total energy absorbed during cracking per unit increase in crack length, was defined by him. Irwin (1952) derived the local stress near crack tip in an isotropic linear elastic material using Airy's stress function in polar coordinated as shown in Eq. (2.4).

$$\sigma_{ij} = \left(\frac{K}{\sqrt{r}}\right) f_{ij}(\theta) + \sum_{m=0}^{\infty} A_m r^{\frac{m}{2}} g_{ij}^{(m)}(\theta) \tag{2.4}$$

where, σ_{ij} : stress tensor, K: constant, r, θ: position in polar coordinate

f_{ij} : leading term, $A_m, g_{ij}^{(m)}$: amplitude and function of θ for mth term

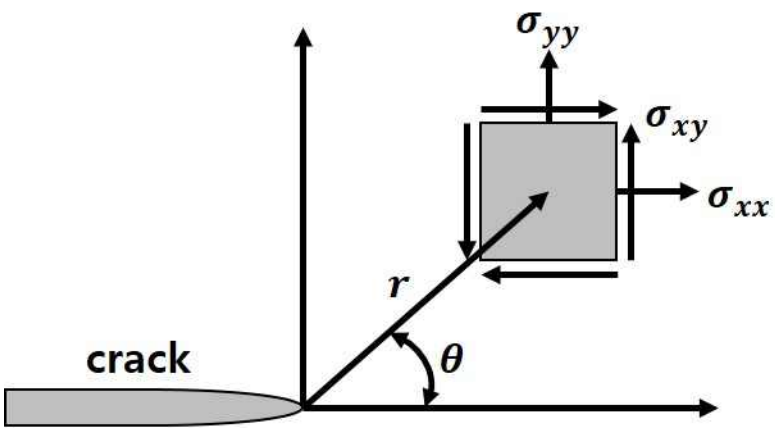

Fig. 2 Definition of the coordinate axis near crack tip

Based on Eq. (2.4), the leading term is proportional to $1/\sqrt{r}$ so it will approach infinity at crack tip where r is zero. Because other higher-order term remains finite at crack tip, stresses at crack tip varies with $1/\sqrt{r}$.

The constant of the leading term in Eq. (2.4), K, is called stress intensity factor. This factor depends on loading, crack shape, crack size and geometric boundaries. The general form of K could be expressed as Eq. (2.5).

$$K = f(g)\sigma\sqrt{\pi a} \tag{2.5}$$

where, σ: nomial stress, a: crack length, $f(g)$: correction factor

The correction factor in Eq. (2.5) depends on specimen and crack geometry. Many studied have been performed to evaluate the correction factors in various specimen and flaw types. Many solutions for a wide variety of problems and published in hand books or international regulations [Tada et al (1973), Rooke and Cartwright

(1976), Murakami (1987), Gray (1992), BSI (2015)]. If there is available solution for stress intensity factor, the stress intensity factor could be calculated through numerical approaches like finite element analysis and weight function techniques [Rice (1972), Rice (1989)] or experimental approaches. As the stress intensity factor reaches a critical value, Kc, unstable facture occurs. The critical value of material is called the fracture toughness. This value is characteristic value of materials and depends on the temperature and specimen thickness.

Initial crack will propagate under cyclic environmental loads. The law between the crack growth rate da/dN and the range of stress intensity factor that the difference between maximum and minimum stress intensity values during a stress cycle, $\Delta K = K_{max} - K_{min}$ is determined experimentally. The overall relationship between da/dN and ΔK in log−log scale could be illustrated as a sigmoidal curve. This curve is divided three distinct regions as shown in Fig. 3.

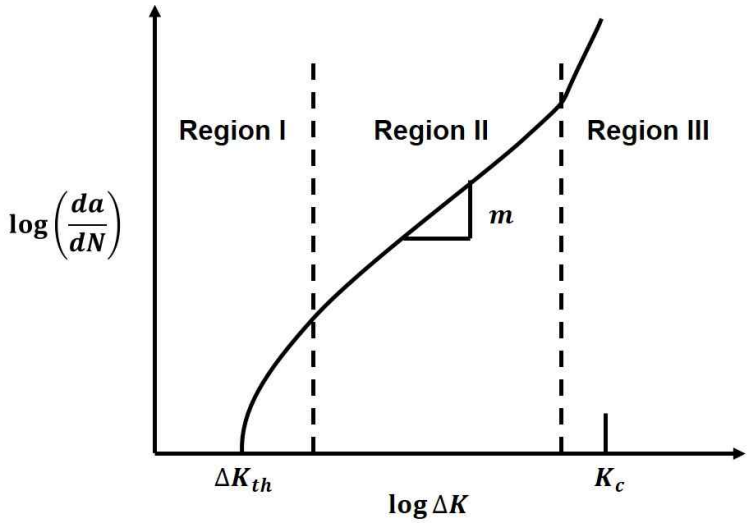

Fig. 3 Schematic crack growth relationships

At region I, where the stress intensity factor range is low, the crack growth rate is zero until the stress intensity factor range reaches threshold value ΔK_{th}. This means that crack does not propagate under cyclic loads which is below ΔK_{th}. The relationship between crack growth rate and stress intensity factor range in log-log scale is linear in region II where occupies the majority of product lifetime. Finally, the crack growth rate in region III increases rapidly after the stress intensity factor reaches the critical value, K_c.

Because region II is dominant in determining the fatigue life, it seems to be sufficient to assume that it is possible to only consider region II in prediction of fatigue life. The most famous law in explaining the linear relationship observed in region II is Paris law show in Eq. (2.6).

$$\frac{da}{dN} = C(\Delta K)^m \tag{2.6}$$

where, C, m: marterial constants

This power-law relationship for fatigue crack growth is widely used to fatigue crack propagation analysis in engineering practice. Other studies has tried to describe whole relationship including region I and III [Forman et al (1967), Klesnil and Lukas (1972), Donahue et al (1972), Forman and Mettu (1992)]. In region II, the crack growth rate is an only function of the stress intensity factor range, but stress ratio R should be considered in other region and the empirical formulas considering entire regions include the effect of stress ratio R in their formulas.

Elber (1970) accidentally discovered the presence of crack closure phenomenon. He performed many fracture experiments with cracked specimens and compared it with standard formulas for corresponding specimens. At high loads, the results of experiments agreed well with the formulas but testing results was close to that of an uncracked specimen. He observed that the surfaces of fatigue cracks contact each other when the remotely applied load is still tensile and did not open until a sufficiently high tensile load is applied. He introduced effective stress intensity factor range to reflect the crack closure in fatigue crack analysis as shown in Eq. (2.7).

$$\Delta K_{eff} \equiv K_{max} - K_{op} \tag{2.7}$$

where, K_{op}: the stress intensity at which the crack open

He also defined an effective stress intensity ratio, U like Eq.

(2.8).

$$U \equiv \frac{\Delta K_{eff}}{\Delta K} = \frac{K_{max} - K_{op}}{K_{max} - K_{min}} \tag{2.8}$$

By substituting the effective stress intensity factor range into the Paris law, a modified Paris law is derived as shown in Eq. (2.9).

$$\frac{da}{dN} = C\left(\Delta K_{eff}\right)^m \tag{2.9}$$

He tried to make an empirical formula for ΔK_{eff} and measured the closure stress intensity in 2023-T3 aluminum at various load levels and stress ratio R. The following equation in Eq. (2.10) was obtained from the experiments.

$$U = 0.5 + 0.4R \ \ (-0.1 \leq R \leq 0.7) \tag{2.10}$$

Many researches have pointed out that Elber's linear representation seemed to be insufficient to capture an apparent non-linear behavior. Improved version of empirical formulas have been suggested by subsequent studies [Newman Jr (1984), Schijve (2004), Correia et al (2016)].

The results mentioned in above are derived in constant amplitude loading condition. As mentioned in the previous chapter, real structures experience irregular loadings during their life time so damage accumulation rule needed to analyze these variable amplitude

loadings. In case of variable amplitude loadings, it is known that loading history is an important factor in determining crack growth rates. However, it is cumbersome to quantify the effect of loading history. For simplicity, it is often assumed that the loading history effect could be ignored and there are many practical situation where such assumption is reasonable.

The linear damage model is suitable for variable amplitude loading when this assumption is reasonable. This model calculates the total crack growth by just summing all crack growth induced by each loading cycle. Then, the incremental of crack size Δa is expressed as shown in Eq. (2.11) if it is assumed that $\Delta a \ll a$.

$$\Delta \mathrm{a} = \left(\frac{da}{dN}\right)_1 N_1 + \left(\frac{da}{dN}\right)_2 N_2 + \cdots \tag{2.11}$$

By substituting Eq. (2.5) and (2.6) into Eq. (2.11), the above equation becomes Eq. (2.12).

$$\begin{aligned} \Delta \mathrm{a} &= \mathrm{C}[(\Delta K_1)^m N_1 + (\Delta K_2)^m N_2 + \cdots] \\ &= Cf(g)(\pi a)^{\frac{m}{2}}[(\Delta\sigma_1)^m N_1 + (\Delta\sigma_2)^m N_2 + \cdots] \end{aligned} \tag{2.12}$$

The procedure of crack propagation analysis for lifetime prediction (N_f) under variable amplitude loadings based on the linear damage rule is summarized in Fig. 4.

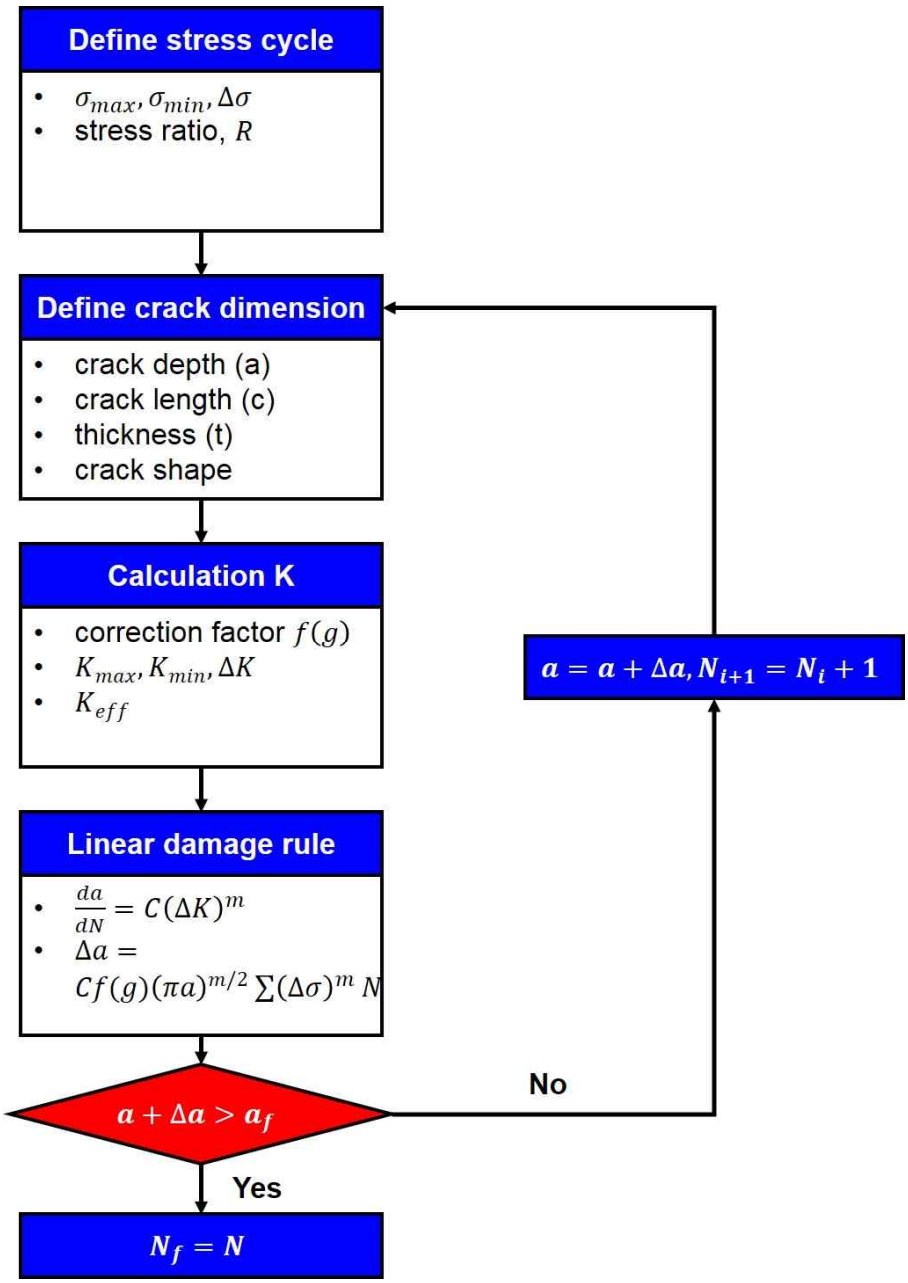

Fig. 4 A procedure for lifetime prediction using fracture mechanics based approach

2.3. Counting methods

In the previous chapters, two distinct ways to evaluate fatigue damages due to irregular random loads. These methods commonly need the information of stress range (or amplitude) and the number of observed stress cycles. This information could be extracted from time history of random process by using cycle counting methods. The cycle counting method is used to summarize irregular load-versus-time histories by providing the number of times cycles of various amplitude occur. Various cycle counting methods have been proposed and the principles of these methods are reviewed in this chapter.

To begin with, some basics properties of an irregular loading is described in Fig. 5. Peak is the point at which sign of the first derivative of random process changes positive to negative. On the other hands, valley is the smallest value between two successive peaks. Fatigue damage induced by variable amplitude loading is assumed to be affected by only a sequence of peak and valley. Thus, continuous form of irregular random loading could be expressed as a sequence of turning points where sign of the first derivative changes like Eq. (2.13).

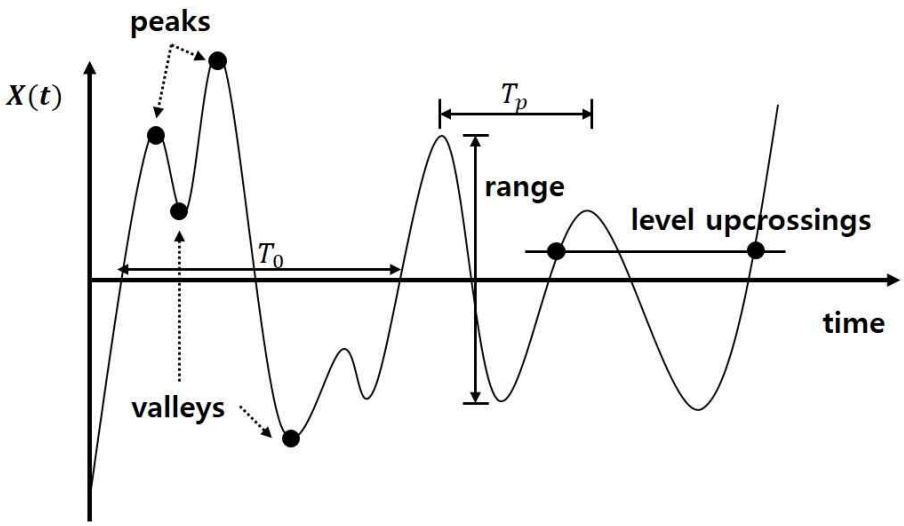

Fig. 5 Description of an example of an irregular random process

$$x(t) = \{m_0, M_0, m_1, M_1, m_2, M_2 \dots\} \tag{2.13}$$

where, m_i: i − th valley, M_i: i − th peak

A cycle is defined as a pair of peak and valley and cycle counting method is an algorithm for matching these peaks and valleys to form cycles. Amplitude (or range) and mean value of cycle defined in Eq. (2.14) and (2.15) are important properties in fatigue analysis

$$s = \frac{M_i - m_i}{2} \rightarrow r = 2s = M_i - m_i \tag{2.14}$$

$$m = \frac{M_i + m_i}{2} \tag{2.15}$$

where, s: amplitdue, r: range, m: mean

Several counting methods are proposed and the properties of each methods was reviewed in the literature [Dowling (1972), ASTM

(2005)]. In this chapter, general four counting methods widely used in practice are introduced: level-crossing counting (LCC), peak-valley counting (PVC), range counting (RC) and rainflow counting methods (RFC). An example of discretized random process is shown in Fig. 6 and the counting results of each method are summarized in Fig. 7.

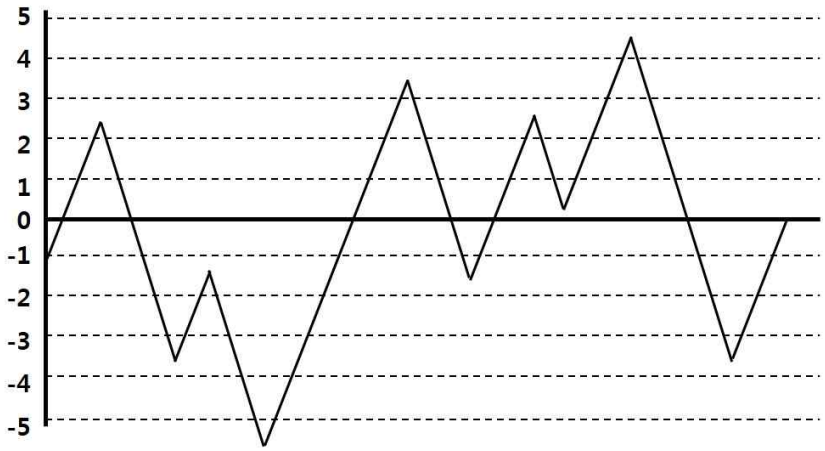

Fig. 6 An example of discretized random process

Level-crossing count	
Range	Counts
9	1
6	1
5	1
1	1

Peak-valley count	
Range	Counts
10	1
7	1
6	1
4	1

Range count		
Range	Counts	Events
2	1	C-D, H-I
3.5	1	A-B, K-L
4	1.5	D-E, G-H I-J
5	0.5	F-G
6	0.5	B-C
8	0.5	J-K
9	0.5	E-F

Rainflow count		
Range	Counts	Events
3.5	0.5	A-B
8	0.5	B-E
2	1	C-D
10	0.5	E-J
5	1	F-G
2	1	H-I
8	0.5	J-K
3.5	0.5	K-L

Fig. 7 The cycle counting results of the given example

Level-crossing count method (LCC) was developed in the 1950s by the aircraft industry to count velocity and accelerations that exceeded certain levels. The counting results of LCC is suggested in Fig. 7. This method records the crossings of random process with fixed levels. Above reference level defined as zero in Fig. 7, only crossing points with positive slope are recorded and negative sloped crossings are registered below the reference level.

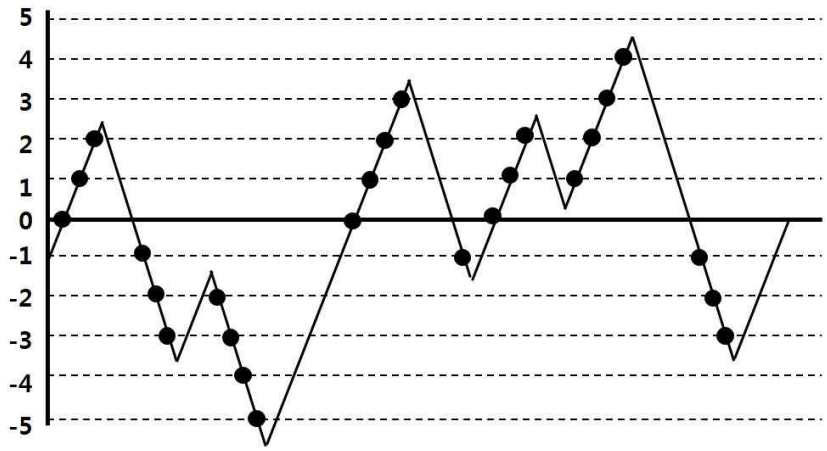

Fig. 8 Result of level-crossing counting (LCC) method

At the reference level, crossings with positive slope are recorded. The cycle is determined that the most damaging cycle count for fatigue analysis. It means that the first cycle consists of the highest peak and the lowest valley in the set of recorded crossings and the second cycle is also constructed at the same manner with available peaks and valleys except used values.

Peak-valley counting identifies all peaks above the reference level and negative valley below the reference level of random process. The cycles are constructed at the same manner of LCC. The most damaging cycle for fatigue analysis is derived from the set of recorded peaks and valleys until all element of the set are used. The sequence of peaks and valleys are not considered when the cycles are constructed.

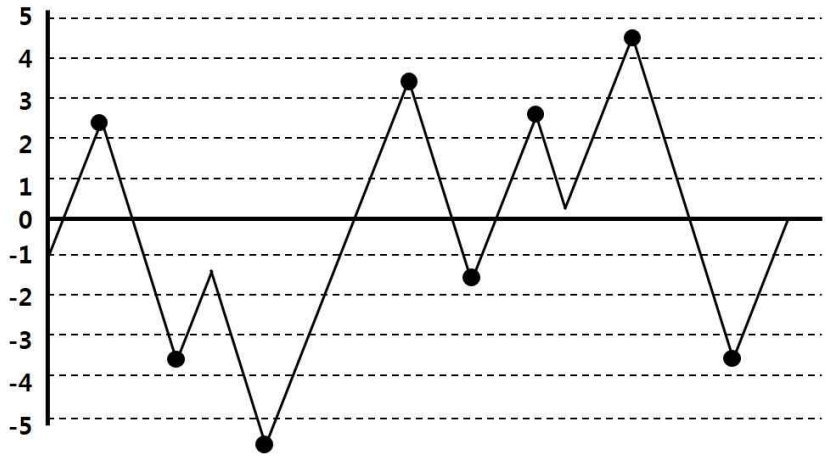

Fig. 9 Result of peak counting (PC) method

Unlike peak-valley count method, the range count method identifies all peaks and valleys without considering the reference level. A peak and the following valley is paired to form one-half cycle and a valley and the following peak also is grouped into one-half cycle. The important feature of this method is the principle of defining cycles considering the sequence of turning points.

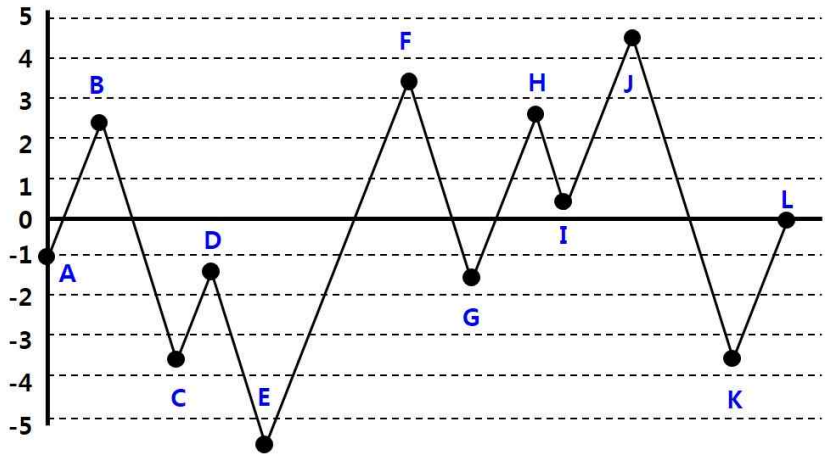

Fig. 10 Result of range counting (RC) method

Dowling (1972) compared cycle counting results for fatigue analysis and concluded that the rainflow counting method was the most accurate method. Rainflow count method was proposed by Matsuishi and Endo (1968) and different several version of RFC algorithm were proposed [Downing and Socie (1982), Rychlik (1987) Amzallag et al (1994)]. The original algorithm proposed by Matsushi and Endo called pagoda-roof algorithm is explained in Fig. 11.

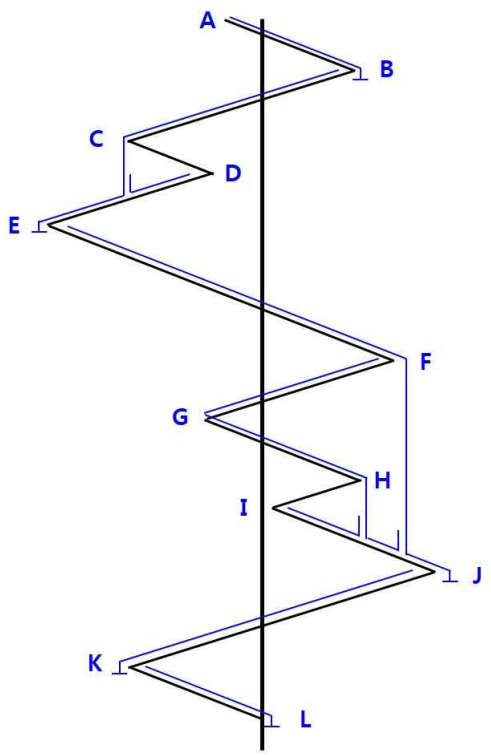

Fig. 11 Result of rainflow counting method (pagoda-roof)

The time history of random process is plotted vertically in Fig. 11. The principle of pagoda-roof algorithm could be described as a flow of raindrop. Imagine that a raindrop on point A. The raindrop will move through below three rule.

A) If the raindrop starts from a valley, it will move until it reaches the smaller valley than its starting point. Then, one-half rainflow cycle is defined a pair of the starting point (valley) and the largest value (peak) during its travel.

B) If the raindrop starts from a peak, it will move until it reaches the larger peak than its starting point. Then, one-half rainflow cycle is defined a pair of the starting point (peak) and the

smallest value (valley) during its travel.

C) The raindrop must stop when it meets the raindrop from a roof above.

For example, the raindrop which starts from point A will stop when it reaches point C which is smaller than point A. One-half rainflow cycle (A-B) is counted. The raindrop which falls in point D will meet the raindrop from the above roof so it must stop at point C. It will make one rainflow cycle (D-C). The detailed results of rainflow cycle is summarized in Fig. 7. The other algorithms such as 3-point algorithm, 4-point-algorithm and non-recursive definition have different principles but all algorithms give the same counting results. In practical, rainflow count method has been accepted the most accurate method so fatigue damages predicted by the time domain approach with rainflow count method have been considered to be the exact solutions.

Chapter 3. Frequency domain methods for Gaussian random loadings

3.1. Introduction

Under stationary narrow-banded Gaussian process assumption, Crandall & Mark (1973) theoretically proved the fact that the probability density function of stress amplitude follows the Rayleigh distribution. The estimated fatigue damage under the assumption could be expressed by the Rayleigh distribution into S-N curve and the Miner rule. However, the assumption are seldom verified in most practical engineering problems. Many studies have been performed to overcome the limitation of the conventional spectral technique derived under the assumptions. Bandwidth of a random process is an important factor that have on effect of fatigue damage induced by the random process. Rychlick (1993) pointed out that the formula derived under narrow-band assumption for estimating fatigue damage tends to overestimate fatigue damages under wide-band processes. Therefore, modification methods have been suggested.

From early 1980s, correction factors for bandwidth effect have been investigated [Wirsching & Light (1980), Lutes & Larsen (1990), Wu (1992)]. They expressed the correction factor as a function of bandwidth parameters and the slope of S-N curve. Then, the estimated fatigue damage for wide-band process was just defined as the multiplication of the correction factor and the estimated fatigue

damage derived under narrow-band assumption. However, many literatures pointed out that this approaches tended to overestimate fatigue damages in small bandwidth ranges. Others have been tried to make approximate models for probability density function (PDF) of stress amplitude in Gaussian processes [Dirlik (1985), Gall and Hancock (1985), Zhao & Baker (1992), Kim & Kim (1994), Petrucci & Zuccarello (2004), Park et al (2014)]. Most of them utilized mixture models which consisted of several parametric probability density functions such as Rayleigh and Weibull distributions. Literatures compared the existing approximate models and concluded that some of them gave very accurate results in Gaussian processes.

Benasciutti & Tovo (2005) gave interesting point of view for the approximate probabilistic models derived in Gaussian processes. They tried to extend the probabilistic model derived in Gaussian processes to non-Gaussian problems and explained that the probabilistic models could be extend to non-Gaussian problems with transformation techniques. However, the entire information of rainflow counted cycle distribution should be required to use the transformation techniques. Therefore, they utilized joint probability distribution function proposed by Tovo (2002) of peaks and valleys forming rainflow cycles.

Unlike above models that have been derived based on approximate background, Frendhal & Rychlik (1993) proposed Markov method for evaluating rainflow matrix in given random processes. It was assumed that the sequence of turning points followed Markov chain. Based on the assumption, the transition

matrix between local maximum and the following minimum was estimated approximately by Slepian model and the rainflow matrix was derived by simple matrix manipulation. In this chapter, basic knowledge for several approximate models for wide-band Gaussian processes are reviewed.

3.2. Random process and spectral representation

A random process is a time-varying function that assigns the outcome of a random experiment or simulation to each time instant. Irregular loading and hot spot stresses are representative examples of random processes in fatigue analysis. Let X(t) is an irregular loading acting on offshore structures. X(t) is assumed as a stationary ergodic process which has a zero mean value. X(t) could be expressed uniquely in time domain by its auto-correlation function as shown in Eq. (3.1).

$$R_X(\tau) = \mathrm{E}[X(t) \cdot X(t+\tau)] \tag{3.1}$$

where, $R_X(\tau)$: auto − correlation function of X(t), E[·]: expected value

τ: time lag

The random process X(t) could be transformed to frequency domain through Wiener-Khinchin theorem and it is called power spectral density or power spectrum $S_X(\omega)$ in Eq. (3.2).

$$S_X(\omega) = \int_{-\infty}^{\infty} R_X(\tau)\, e^{-i\omega\tau}\, d\tau \quad \leftrightarrow R_X(\tau) = \int_{-\infty}^{\infty} S_X(\omega)\, e^{i\omega\tau}\, d\omega \tag{3.2}$$

where, $S_X(\omega)$: two − sided power spectral density

In general, only positive frequency components in two−sided power spectral density are utilized and it is called as one−sided power spectral density expressed in Eq. (3.3).

$$S_X^+(\omega) = W_X(\omega) = \begin{cases} 2S_X(\omega) & \text{when } 0 \le \omega < \infty \\ S_X(0) & \text{when } \omega = 0 \end{cases} \tag{3.3}$$

where, $W_X(\omega)$: one − sided power spectral density

Mathematical moments of one−sided power spectral density $W_X(\omega)$ are called as spectral density as shown in Eq. (3.4).

$$m_k = \int_0^{\infty} \omega^k W_X(\omega) d\omega \qquad k = 0,1,2 \ldots \tag{3.4}$$

where, m_k: k − th order spectral moment of $W_X(\omega)$

There are important relationship between spectral moments of $W_X(\omega)$ and statistical properties of X(t). By substituting zero into time lag () in Eq. (3.1) and (3.2), the relationship between m_0 and σ_X is derived as Eq. (3.5).

$$m_0 = \sigma_X^2 \tag{3.5}$$

where, σ_X: variance of X(t)

In the same manner, the variances for derivative of X(t) could be expressed as Eq. (3.6).

$$m_2 = \sigma_{\dot{X}}^2, \qquad m_4 = \sigma_{\ddot{X}}^2 \tag{3.6}$$

Some other characteristics of random process X(t) are defined as spectral moments. In Gaussian assumption, the expected rate of mean-upcrossings which means the expected number of mean-upcrossings in unit time is derived as Eq. (3.7).

$$v_0 = \frac{1}{2\pi}\sqrt{\frac{m_2}{m_0}} \tag{3.7}$$

where, v_0: mean − upcrossing rate

And the expected number of peaks in unit time is defined as Eq. (3.8).

$$v_p = \frac{1}{2\pi}\sqrt{\frac{m_4}{m_2}} \tag{3.8}$$

where, v_0: mean number of peaks

An important time-domain property of random process is the irregularity factor (IF) which is defined as the ratio the mean-upcrossing rate to mean number of peaks as shown in Eq. (3.9).

$$\boldsymbol{F} = \frac{v_0}{v_p} \tag{3.9}$$

The irregularity factor means the expected number peaks located between successive two mean-upcrossings. In narrow-band process where most power spectral densities are concentrated on narrow frequency range, only one peak exists in successive mean-upcrossings. In other words, the irregularity factor approaches to one in narrow-band process. In wide-band process, irregularity factor goes to zero and it means that there are many peaks between two successive mean-upcorssings.

Another important parameter which indicate the bandwidth of random process is bandwidth parameters α_i in Eq. (3.10). In most literatures, the 1st and 2nd bandwidth parameters have been widely used to analyze bandwidth effect on fatigue damages.

$$\alpha_i = \frac{m_i}{\sqrt{m_0 m_{2i}}} \rightarrow \alpha_1 = \frac{m_1}{\sqrt{m_0 m_2}}, \alpha_2 = \frac{m_2}{\sqrt{m_0 m_4}} \tag{3.10}$$

Bandwidth parameters range from zero to unity. When X(t) is close to wide-band process, α_i approaches to zero. In narrow-band process, α_i goes to unity. An example of narrow and wide band process are suggested in Fig. 12. It is mathematically proven that i^{th} bandwidth parameter is always larger than j^{th} bandwidth parameter where i is smaller than j ($\alpha_i \geq \alpha_j$ when $i \leq j$).

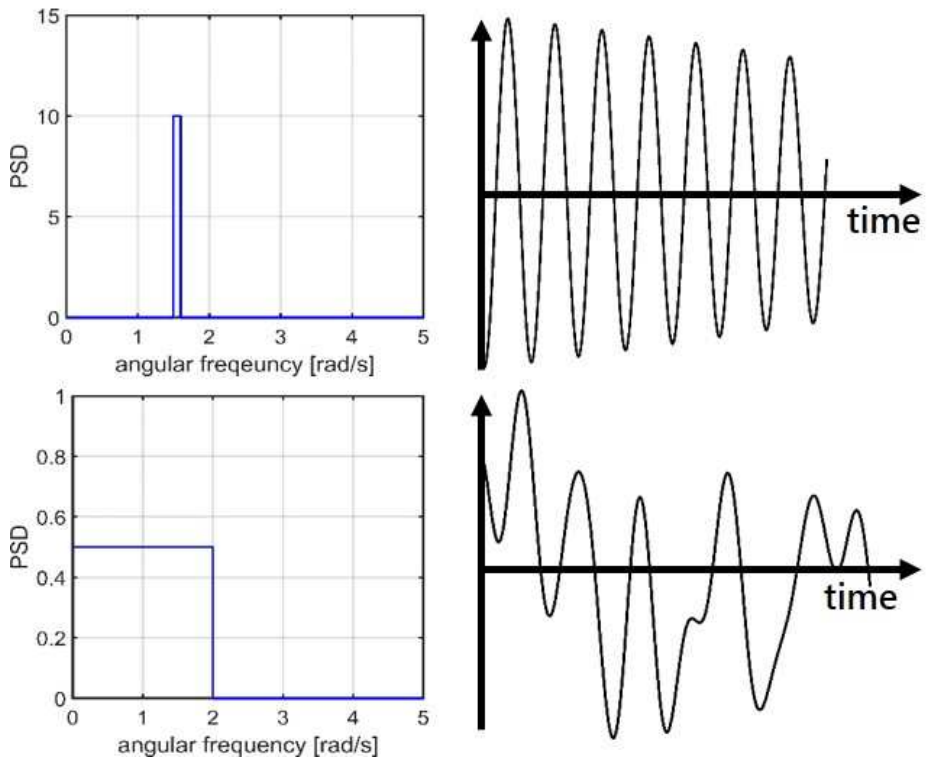

Fig. 12 Examples of narrow-band (upper) and wide-band (lower) process and their power spectral densities

In Gaussian process, it was proved that the irregularity factor and the 2nd bandwidth parameter were the same [Lutes and Sarkani (1997)]. Although they are not identical in non-Gaussian process, they seem to be quite similar.

Another version of bandwidth parameter in Eq. (3.11) and (3.12) was used [Vanmarcke (1972), Wirsching and Light (1980)].

$$q_X = \sqrt{1 - \frac{m_1^2}{m_0 m_2}} = \sqrt{1 - \alpha_1^2} \quad \text{[Vanmarcke (1972)]} \quad (3.11)$$

$$\varepsilon = \sqrt{1 - \frac{m_2^2}{m_0 m_4}} = \sqrt{1 - \alpha_2^2} \quad \text{[Wirsching \& Light (1980)]} \quad (3.12)$$

The bandwidth parameters (β_i) of the 1st derivative of the random process X(t) could be defined as similar way in Eq. (3.10). Benascuitti & Tovo (2005) expressed them as in Eq. (3.13).

$$\beta_i = \frac{m_{i+2}}{\sqrt{m_2 m_{2i+2}}} \rightarrow \beta_1 = \frac{m_3}{\sqrt{m_2 m_4}}, \beta_2 = \frac{m_4}{\sqrt{m_2 m_6}} \quad (3.13)$$

Petrucci et al. (2000) utilized another expression of β_i and explained the statistical meaning of the parameter.

$$q_{\dot{X}} = \sqrt{1 - \frac{m_3^2}{m_2 m_4}} = \sqrt{1 - \beta_1^2} \quad (3.14)$$

The probability density function of peaks ($p_p(u)$) was derived by Lutes and Sarkani (1997) when the random process X(t) was assumed to be a zero-mean Gaussian process as shown in Eq. (3.15).

$$p_p(u) = \frac{\sqrt{1-\alpha_2^2}}{\sqrt{2\pi}\sigma_X} exp\left(-\frac{u^2}{2\sigma_X^2(1-\alpha_2^2)}\right) + \frac{\alpha_2 u}{\sigma_X^2} exp\left(-\frac{u^2}{2\sigma_X^2}\right)\Phi\left(\frac{\alpha_2 u}{\sigma_X\sqrt{1-\alpha_2^2}}\right) \quad (3.15)$$

where, $\Phi(\cdot)$: the standard normal distribution $\left(= \frac{1}{\sqrt{2\pi}}\int_{-\infty}^{\infty} e^{-\frac{t^2}{2}} dt\right)$

Under symmetrical process assumption, the probability density function of valleys could be expressed as Eq. (3.16).

$$p_v(v) = p_p(-v) \tag{3.16}$$

Fig. 13 shows examples of the probability density functions of peaks with different irregularity factors. When irregularity factor goes to one, which means the random process X(t) follows a narrow-band process, the probability density function of peaks approaches to the Rayleigh distribution. In addition, the probability density function would be the Normal distribution as the irregularity factor is close to zero.

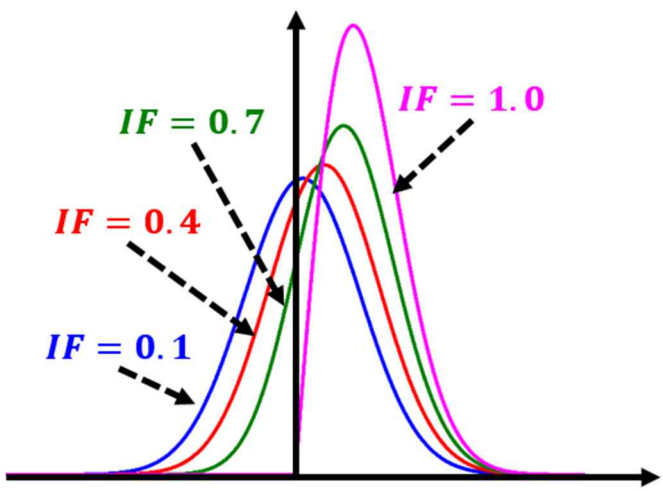

Fig. 13 The probability density functions of peaks with different irregularity factors

Fatigue damage depends on amplitude and mean values of stress cycles. Stress cycles consist of peaks and valleys and several cycle counting methods mentioned in 2.3 have their own algorithms for pairing peaks and valleys. Because the rainflow cycle counting algorithm has been known as the most accurate method for fatigue damage assessment, many literatures have been tried to establish the relationship between rainflow cycle counted results and spectral description of a random process X(t). For a zero-mean Gaussian process X(t), it was proven that the probability density function of rainflow cycles followed the Rayleigh distribution by Miles (). However, in wide-band processes, the exact expression between spectral parameters and rainflow cycle distribution has been not derived in theoretical background until now.

Let x(t), $0 \le t \le T$, is a realization of random process X(t). Peaks and valleys of x(t) where the slope of X(t) change are defined as M_k and m_k respectively and a stress cycle consisting of M_k and m_k is expressed as $(M_{k,}m_k)_{t_i}$ where t_i is the time when M_k occurs. Frendhal & Rychlik (1993) defined a counting distribution of a cycle count $N_T(u,v)$ as Eq. (3.17).

$$N_T(u,v) = \#\left\{(M_{k,}m_k)_{t_i}; t_i < T \ \ and \ \ u > M_{k,} > v > m_k\right\} \quad (3.17)$$

The counting distribution is the observed number of cycles with peak higher than u and valley lower than v during time length T. They compared the counting distribution of several cycle counting methods

and pointed out that the diagonals $N_T^{RFC}(u,u)$ and $N_T^{PV}(u,u)$ were identical and equal to the number of downcrossings of the level u by the x(t). Another important fact they found was that the counting distribution of a peak−valley counting method is equal to the number of peaks higher than u such that the following valley is lower than v. In case of rainflow counting method, it is less obvious that counting distribution is equal to the number of downcrossings of the level u followed by a downcrossing of the level v without passing u in between. In other words, the relationship between counting distribution of two counting methods is derived by Eq. (3.18).

$$N_T^{PV}(u,v) < N_T^{RFC}(u,v) \tag{3.18}$$

It means that the observed number of stress cycles whose peaks are larger than u and valleys are lower than v in the rainflow counting method is always larger than that of the peak−valley counting method. Thus, fatigue damage estimated by the rainflow counting method is always bigger than the peak−valley counting method as Eq. (3.19).

$$\bar{D}^{PV} < \bar{D}^{RFC} \tag{3.19}$$

where, $\bar{D}$: damage rate (= damage in unit time)

A counting intensity $\mu(u,v)$ which indicates the expected number of cycles with peaks higher than u and valleys lower than v in unit time was also defined as the expected value of the counting distribution $N_T(u,v)$ as Eq. (3.20).

$$\mu_T(u,v) = E[N_T(u,v)] \rightarrow \mu(u,v) = \lim_{T\rightarrow\infty} \frac{\mu_T(u,v)}{T} \tag{3.20}$$

Benasciutti & Tovo (2005) suggested another descriptor for expressing statistical distribution of counted cycles based on probability density concept. They defined joint probability distribution $\mathrm{h(u,v)}$ of peaks and valleys forming rainflow cycles. By using The joint cumulative probability distribution $\mathrm{H}(u,v)$ which means the occurrence probability of stress cycles consisting peaks lower than u and valleys lower than v is defined as Eq. (3.21).

$$H(u,v) = \int_{-\infty}^{u}\int_{-\infty}^{v} h(x,y)dxdy \tag{3.21}$$

The joint probability distribution of stress mean and amplitude $p_{a,m}(s,m)$ could be obtained by substituting Eq. (2.14) and (2.15) into Eq. (3.21) as shown in Eq. (3.22).

$$p_{s,m}(\mathrm{s,m}) = 2\mathrm{h}(m+s, m-s) \tag{3.22}$$

Marginal distribution of stress mean or amplitude is easily derived by integrating Eq. (3.23).

$$p_s(s) = \int_{-\infty}^{\infty} p_{s,m}(s,m)\,dm, \quad p_m(m) = \int_{0}^{\infty} p_{s,m}(s,m)\,ds \tag{3.23}$$

In Eq. (2.3), accumulated fatigue damage is expressed as a function of constants in S−N curve, the mth power of stress range and the number of stress cycles. Therefore, the expected fatigue damage could be expressed as Eq. (3.24).

$$E[D] = E\left[\sum_{i=1}^{n} \frac{n_i}{\bar{a}} (\Delta\sigma_i)^m\right] = \frac{E[n]}{\bar{a}} E[(\Delta\sigma)^m] \qquad (3.24)$$

In stationary process, the expected number of stress cycles $\mathrm{E}[n]$ is expressed as a multiplication of the expected intensity of counted cycles and time length. In complete counts where the number of all counted cycles is equal to the number of peaks, the expected intensity is the same as v_p. Then, Eq. (3.24) could be rewritten as Eq. (3.25).

$$E[D] = \frac{E[n]}{\bar{a}} E[(\Delta\sigma)^m] = \frac{v_p}{\bar{a}} \int_0^\infty p_a(r) r^m \, dr \qquad (3.25)$$

where, $r = \text{stress range } (= 2s)$

In short, the expected fatigue damage could be obtained by substituting the marginal distribution of stress amplitude into Eq. (3.25).

3.3. Approximate models for wide-banded Gaussian processes

In previous chapter, it is known that if we know the marginal

distribution of stress amplitude, the expected value of fatigue damage could be calculated by Eq. (3.25).

When the random loading x(t) follows narrow-band process where irregularity factor is one, the probability density function of peak goes to the Rayleigh distribution from Eq. (3.15). Furthermore, the intensity of counted cycles can be assumed to be the mean upcrossing rate v_0 defined in Eq. (3.7). Under the symmetry process condition, the probability density function of stress range is also the Rayleigh distribution so the expected value of fatigue damages could be derived by substituting the Rayleigh distribution into Eq. (3.25).

$$E[\bar{D}^{NB}] = \frac{v_0}{\bar{a}}\left(\sqrt{2m_0}\right)^m \Gamma\left(1+\frac{m}{2}\right) \tag{3.26}$$

where, $\Gamma(\cdot)$: gamma function

The formula for fatigue damage under stationary narrow-band Gaussian process assumption in Eq. (3.26) has been widely used to fatigue life assessment in many real engineering problems. However, strictly speaking, it should be applied exactly only for the random process x(t) which perfectly satisfies the assumptions. If it is deviated from the narrow-band assumptions, the expression might significantly overestimate fatigue damages. Fig. 14 shows the ratio of actual fatigue damages of wide-band random processes having different irregularity factors to estimated fatigue damages from the narrow-banded assumption.

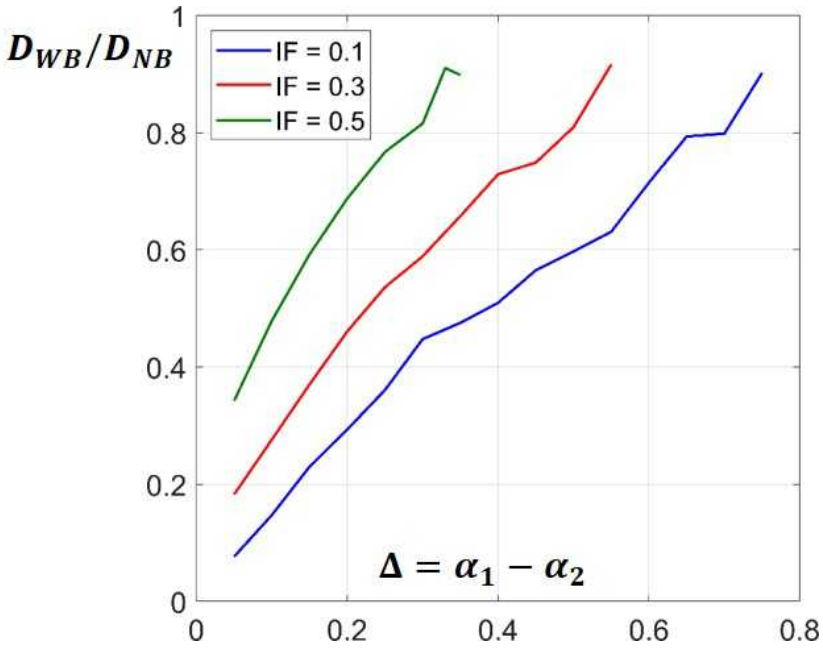

Fig. 14 The ratio of actual fatigue damage to estimated fatigue damage calculated under narrow-band assumption with different irregularity factors

When the irregularity factor is 0.1 (blue solid line), the estimated fatigue damages from the narrow-banded assumption seem to overestimate the exact value up to 10 times. Thus, the effect of bandwidth on fatigue damage should be investigated to reduce the error from the narrow-band assumption.

Many studies have been performed since 1980 and until now no analytical model for marginal distribution of stress amplitude is derived for general wide-banded Gaussian processes. Thus, most proposed model for handling bandwidth effect have been derived based on approximate approaches.

■ Correction factor

Wirsching & Light (1980) suggested a correction factor to reflect the bandwidth effect on fatigue life. The expected rainflow damage $\bar{D}_{W\,L}^{RFC,G}$ was defined the multiplication the estimated damage under narrow-band assumption $\bar{D}^{NB}$ and proposed correction factor for bandwidth parameters as shown in Eq. (3.27).

$$\bar{D}_{W\,L}^{RFC,G} = \rho_{W\,L}\bar{D}^{NB} \tag{3.27}$$

The correction factor was defined as a function of bandwidth parameter and the slope of S-N curve as shown in Eq. (3.28).

$$\rho_{W\,L} = a(m) + [1 - a(m)](1 - \varepsilon)^{b(m)} \tag{3.28}$$

where, $a(m) = 0.926 - 0.033m, b(m) = 1.587m - 2.323, \varepsilon = \sqrt{1 - \alpha_2^2}$

When a_2 goes to one, which means the random process x(t) is close to narrow-band process, $\rho_{W\,L}$ also approaches one. Thus, the estimated $\bar{D}^{RFC}$ is equal to $\bar{D}^{NB}$ in this case. From the literature review, this model seems to give good agreements when the process is close narrow-band process. However, it tends to overestimate $\bar{D}^{RFC}$ as a_2 goes to zero [Benasciutti & Tovo (2005)].

■ Approximation on PDF of amplitude $(p_{RFC}(s))$

Dirlik (1985) proposed another approach. Unlike the WL model,

he tried to make an approximate model for probability density function of rainflow stress amplitude in wide-banded Gaussian processes. He performed a lot of number of time simulations using two idealized spectra to make the approximate model. Normalized spectral moments were defined as Eq. (3.29).

$$M_{RR}(m) = \frac{\int_0^\infty z^m p_a(z)dz}{\int_0^\infty \frac{z^m e^{-z^2}}{2} dz} \tag{3.29}$$

where, $M_{RR}(m)$: m − th normalized moment of rainflow range

The first step of the approximation was to determine the shape of probability density function. He used a mixture model to reflect different shape of rainflow counted results in low, mid-range and large range regions. The mixture model consisted of one exponential and two Rayleigh distribution as shown in Eq. (3.30). Then, the parameters needed to define each distribution were approximated as functions of normalized moment of rainflow range.

$$p_{DK}^{RFC,G}(s) = \frac{1}{\sqrt{m_0}}\left[\frac{D_1}{Q}e^{-\frac{Z}{Q}} + \frac{D_2 Z}{R^2}e^{-\frac{Z^2}{2R^2}} + D_3 Z e^{-\frac{Z^2}{2}}\right] \tag{3.30}$$

where, $Z = \frac{s}{\sqrt{m_0}}$, $x_m = \frac{m_1}{m_0}\sqrt{\frac{m_2}{m_4}} = \alpha_1\alpha_2$, $D_1 = \frac{2(x_m - \alpha_2^2)}{1+\alpha_2^2}$,

$$D_2 = \frac{1 - \alpha_2 - D_1 + D_1^2}{1 - R}, \quad D_3 = 1 - D_1 - D_2$$

$$Q = \frac{1.25(\alpha_2 - D_3 - D_2 R)}{D_1}, \quad R = \frac{\alpha_2 - x_m - D_1^2}{1 - \alpha_2 - D_1 + D_1^2}$$

By substituting Eq. (3.30) into Eq. (3.25), the expected rainflow damage $\bar{D}_{DK}^{RFC,G}$ is expressed as Eq. (3.31).

$$\bar{D}_{DK}^{RFC,G} = \frac{\nu_p}{\bar{a}} m_0^{m/2} \left[D_1 Q^m \Gamma(1+m) + 2^{m/2} \Gamma\left(1+\frac{m}{2}\right)(D_2|R|^m + D_3) \right] \quad (3.31)$$

By far, the Dirlik model is known as one of the most accurate approximate model in fatigue analysis for wide-band Gaussian processes. After he proposed the approximate model, other researchers have proposed different mixture models to describe the probability density function of rainflow amplitude [Gall and Hancock (1985), Zhao-Baker (1992), Kim & Kim (1994), Park et al. (2014)] .

Park et al. (2014) proposed a mixture model consisting of a half-Gaussian for small amplitude region and two Rayleigh distributions for mid and high amplitude regions. He pointed out that Dirlik model tended to underestimate fatigue damage as bandwidth parameter goes to zero. They used a half-Gaussian distribution to describe rainflow amplitude probability in small range region instead of an exponential distribution in Dirlik model and adjusted the parameters in each distribution. The approximate model is given in Eq. (3.32).

$$p_{DK}^{RFC,G}(s) = c_G \frac{2}{\sqrt{2\pi}\sigma_G} e^{\left(-\frac{z^2}{2\sigma_G^2}\right)} + c_{R1} \frac{z}{\sigma_{R1}^2} e^{\left(-\frac{z^2}{2\sigma_{R1}^2}\right)} + c_{R2} z e^{\left(-\frac{z^2}{2}\right)} \quad (3.32)$$

where, $c_G = 1 - c_{R1} - c_{R2}, c_{R1} = \frac{C_{M\,RR(2)} - C_{M\,RR(3)}}{\sigma_{R1}^2(1-\sigma_{R1})}, \sigma_{R1} = \alpha_2$

$c_{R2} = \frac{-\sigma_{R1} C_{M\,RR(2)} + C_{M\,RR(3)}}{(1-\sigma_{R1})}, \sigma_G = \frac{1}{V_1 c_G}\left(C_{M\,RR(1)} - c_{R1}\sigma_{R1} - c_{R2}\right)$

$C_{M\,RR(1)} = \alpha_1, C_{M\,RR(2)} = \alpha_{0.95}\alpha_{1.97}, C_{M\,RR(2)} = \alpha_{0.54}\alpha_{0.93}\alpha_{1.95}$

The expected rainflow damage $\overline{D}_{RFC}^{JB}$ is expressed as Eq. (3.33).

$$\overline{D}_{JB}^{RFC,G} = \frac{v_p}{\overline{a}}\left(2\sqrt{2}m_0\right)^m \left[\begin{array}{c} \frac{c_G}{\sqrt{\pi}}\sigma_G^m \Gamma\left(\frac{m+1}{2}\right) + c_{R1}\sigma_{R1}^m \Gamma\left(\frac{m+2}{2}\right) \\ +c_{R2}\Gamma\left(\frac{m+1}{2}\right) \end{array}\right] \quad (3.33)$$

■ Approximation on JPD of mean and amplitude $(p^{RFC}(s,m))$

Benasciutti & Tovo (2005) pointed out that some approximate models for probability density function of rainflow amplitude predict fatigue damage in wide-band Gaussian process very accurately. However, these models did not account for any information of stress mean so it is not possible to these models to further extension to non-Gaussian problems. They explained that the entire information of cycle distribution such as count intensity $\mu(u,v)$ or joint distribution of peaks and valley $h(u,v)$ to extend the probabilistic models derived in Gaussian process. Therefore, they suggested joint probability distribution of peaks and valleys in Gaussian processes.

They utilized the fact that the expected rainflow damage $(\overline{D}_{RFC})$ is always located between the level crossing counted$(\overline{D}_{LCC})$ and the range counted damage$(\overline{D}_{RC})$.

$$\overline{D}^{RC} < \overline{D}^{RFC} < \overline{D}^{LCC} \quad (3.34)$$

In case of range counted joint probability distribution of peaks

and valley, there is no theoretical model but an approximate model was proposed by Tovo (2002) which gives the same fatigue damage evaluated by range count method as shown in Eq. (3.35).

$$h^{RC,G}(u,v) = \frac{1}{2\sqrt{2\pi}m_0\alpha_2^2} e^{-\frac{u^2+v^2}{4m_0(1-\alpha_2^2)}} e^{-\frac{(u-v)^2}{4m_0(1-\alpha_2^2)}\frac{1-2\alpha_2^2}{2\alpha_2^2}} \left[\frac{u-v}{\sqrt{4m_0(1-\alpha_2^2)}}\right] \tag{3.35}$$

The corresponding joint probability distribution of stress mean and amplitude $p_{a,m}^{RC}(\mathrm{s},\mathrm{m})$ and the marginal distribution of range count amplitude $p_a^{RC}(\mathrm{s})$ are given in Eq. (3.36) and (3.37).

$$p_{s,m}^{RC,G}(\mathrm{s},\mathrm{m}) = \frac{1}{\sqrt{2\pi m_0(1-\alpha_2^2)}} e^{-\frac{m^2}{2m_0(1-\alpha_2^2)}} \frac{s}{m_0\alpha_2^2} e^{-\frac{s^2}{2\alpha_2^2 m_0}} \tag{3.36}$$

$$p_s^{RC,G}(\mathrm{s}) = \frac{s}{m_0\alpha_2^2} e^{-\frac{s^2}{2\alpha_2^2 m_0}} \tag{3.37}$$

In level-crossing count method, as described in chapter 2, only positive peaks are paired to only negative valleys which have the same magnitude of peaks. The remaining turning points such as negative peaks and positive valleys are paired to valleys and peaks which have the same magnitude and sign and they form non-damaging cycles. This fact leads to the following distribution of peaks and valleys counted level-crossing count algorithm.

$$h^{LCC,G}(u,v) = \begin{cases} [p_p(u) - p_v(u)]\delta(u+v) + p_v(u)\delta(u-v) & \text{if } u > 0 \\ p_p(u)\delta(u-v) & \text{if } u \le 0 \end{cases} \quad (3.38)$$

where, $\delta(\cdot)$: Dirac delta function

As shown in Eq. (3.38), damaging cycles that have non-zero amplitude are only evaluated in the first term when u is positive. The joint probability distribution of mean and amplitude and marginal distribution of LCC amplitude are given in Eq. (3.39) and (3.40).

$$p_{s,m}^{LCC,G}(s,m) = \begin{cases} [p_p(s) - p_v(s)]\delta(m) + p_v(m)\delta(s) & \text{if } s+m > 0 \\ p_p(m)\delta(s) & \text{if } s+m \le 0 \end{cases} \quad (3.39)$$

$$p_s^{LCC}(\mathrm{s}) = [p_p(s) - p_v(s)] = \alpha_2 \frac{s}{m_0} e^{-\frac{s^2}{2m_0}} \quad (3.40)$$

As seen in Eq. (3.40), the total probability sum of marginal distribution of LCC amplitude is equal to α_2. As mentioned above, the remaining probability $(1-\alpha_2)$ is assumed to concentrate on the origin in this model.

Finally, the rainflow joint probability distribution of peaks and valleys $(h_{RFC}(u,v))$ was defined as the linear interpolation of two joint probability distributions as Eq. (3.41).

$$h^{RFC,G}(u,v) = b_{app} h^{LCC,G}(u,v) + (1 - b_{app}) h^{RC,G}(u,v) \quad (3.41)$$

where, b_{app}: interpolation coefficient

Tovo (2002) calculated the correlation between b_{app} and spectral parameters based on reasonable assumptions and calibrated on numerical simulations. The formula proposed by Tovo is shown in Eq. (3.42)

$$b_{app}^{Tovo} = \min\left\{\frac{\alpha_1 - \alpha_2}{1 - \alpha_1}, 1\right\} \tag{3.42}$$

In further research, Benasciutti & Tovo (2005) re-evaluated the interpolation coefficient and suggested more accurate b_{app} as shown in Eq. (3.43)

$$b_{app}^{BT} = \frac{(\alpha_1 - \alpha_2)\left[1.112\left(1 + \alpha_1\alpha_2 - (\alpha_1 + \alpha_2)\right)e^{2.11\alpha_2} + (\alpha_1 - \alpha_2)\right]}{(\alpha_2 - 1)^2} \tag{3.43}$$

Fig. 15 shows an example of marginal distribution estimated by DK, JB and BT models. BT model tends to underestimate probability density in low amplitude region due to the LCC algorithm. In given example, DK model gives the best agreement on the actual data distribution. Three approximate model seem to give accurate representation of actual data in mid and high amplitude regions.

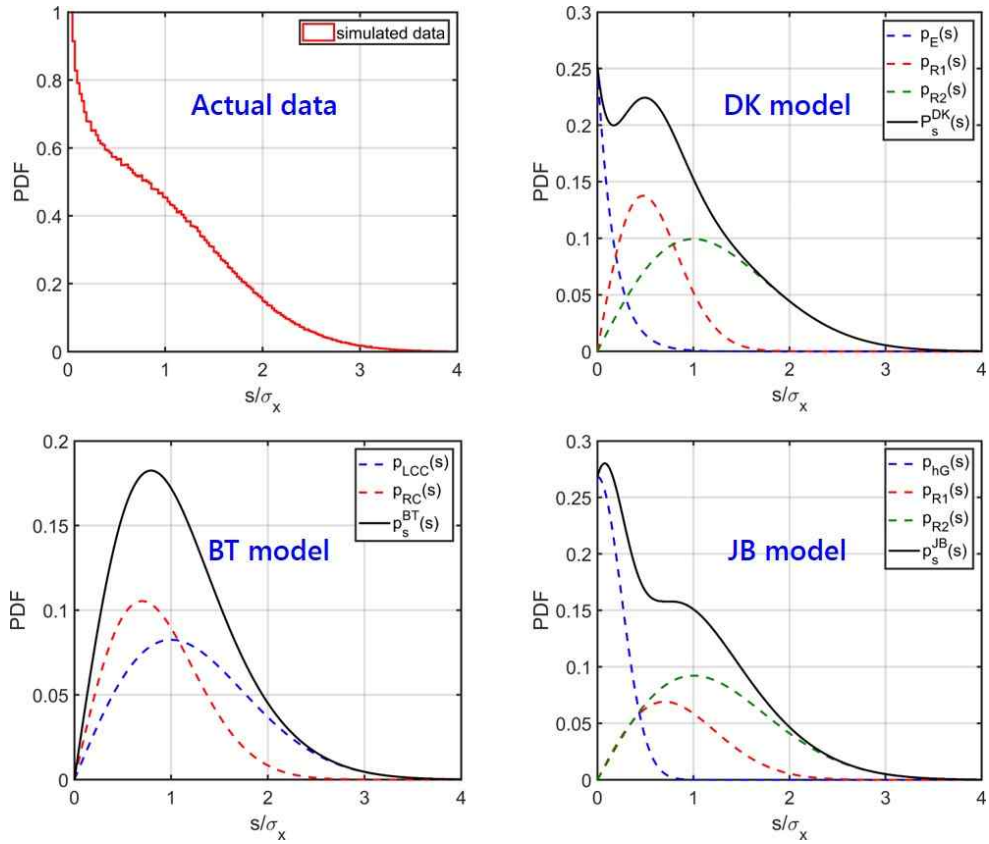

Fig. 15 Marginal distributions of rainflow amplitude estimated by DK, BT and JB models $(\alpha_1, \alpha_2) = (0.85, 0.7)$

Fig. 16 shows an example of joint probability distribution estimated by BT models. Two joint probability distribution model are marked in the scatter plot. As mentioned above, all probability of LCC joint probability distribution are located at the line $(m = 0)$. It makes a difference to actual data. In given example, BT model tend to distort the information of mean distribution and most probability are concentrated on the line where mean is zero. Although, this fact has no effect on the expected rainflow damage in Gaussian problems which just depends on the marginal distribution of rainflow amplitude,

it might affect the accuracy of fatigue damage assessment in non-Gaussian problem. The details are handled in Chapter 6.

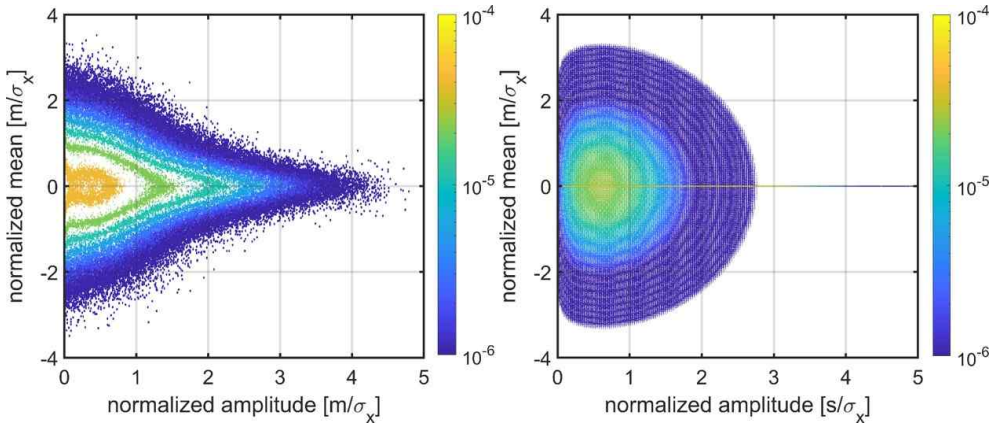

Fig. 16 Estimated joint probability distribution of peaks and valleys by BT model (right) and scatter plot of actual data (left).

Chapter 4. Construction of a new regression model for joint probability distribution of stress mean and amplitude in Gaussian process

4.1. Introduction

As explained in previous chapter, the joint distribution function of amplitude and mean is required to further extension to non-Gaussian problems. And also the joint probability distribution derived in Gaussian processes itself is required to crack propagation analysis with considering crack closure effect which requires stress ratio R.

Some approximate models have been already suggested by Benasciutti & Tovo(2005), Frendhal & Rychlik (1993). The joint probability distribution estimated by the BT model tend to distort mean distribution so most probabilities are concentrated where mean is zero. It is not a big deal when estimating fatigue damages in Gaussian problems which require only the marginal distribution of rainflow amplitude but in case of non-Gaussian problem it could have on large effect on the estimated rainflow damages. The detail results will be explained in Chapter 6.

Markov method proposed by Frendhal & Rychlik (1993) has been one of the most accurate model for estimating the rainflow joint probability distribution and many literatures have reviewed the Markov method [Rychlik et al (1995), Lindgren & Broberg (2004)]. The rainflow matrix whose elements are rainflow count intensity

$\mu_{RFC}(u,v)$ was derived by the peak−valley count intensity $\mu_{PV}(u,v)$ with a simple matrix manipulations. The peak−valley count intensity $\mu_{PV}(u,v)$ could be obtained approximately from Slepian model. This method gives quite accurate estimation on the joint probability distribution but it has also some limitations. It has no explicit formula for $\mu_{PV}(u,v)$ and it should be calculated from multi−dimensional numerical integration. They also suggested efficient way to calculate numerical integration. In case of narrow−band process, it is possible to use large step for numerical integration so require time for Markov method is greatly reduced. However, in case of wide−band process where a large number of peaks occur between successive up−crossing, estimated fatigue damage could be greatly overestimated without very fine step for integration. This problem could be overcome by introducing the rainflow filter that eliminates unwanted high frequency components. But until now, the rainflow filter for general cases in frequency domain has been not successfully derived.

In this chapter, another approximate model for joint probability distribution of mean and amplitude is suggested by the author. Two aspects should be considered in deriving the new model. First, it should be evaluated joint probability distribution efficiently. It means that the model should not require any numerical iteration to reduce computational time. Second, the model should give better representation of actual data than the existing models.

The new model is derived by approximate way. It requires a large amount of time simulation data so the procedure of time simulations is introduced in this chapter at first. Then, the form of the

approximate model used in this work is determined from investigation on the time simulation data. Finally, regression analysis to make relationship between parameters defining the approximate model and spectral parameters of give power spectral densities is performed to derive a simple formula for joint probability distribution in Gaussian processes.

4.2. Approximation on conditional probability density function of rainflow mean given amplitude

4.2.1. Procedure for time simulation

The first step to make an approximate model for joint probability distribution is to perform time simulations for obtaining a large number of time series data x(t). The five different shapes of spectra shown in Fig. 17 proposed by Benasciutti & Tovo (2005) are used in this simulations. 0th spectral moment (m_0) of all stress spectra are taken as 10 in this study to compare the time series data from different shapes of spectra.

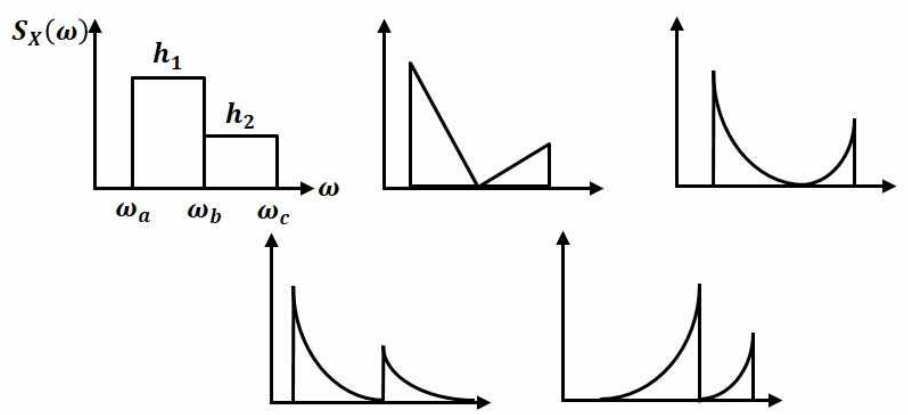

Fig. 17 Five stress spectra used in simulations

Shape parameters $(h_1, h_2, \omega_a, \omega_b, \omega_c)$ of each stress spectra are calculated to cover various range of bandwidth parameters. Among them, ω_a, ω_c are taken as $\frac{2\pi}{1000}$ and 2π respectively and other parameters are calculated based on optimization for matching target bandwidth parameters. The range of bandwidth parameters are summarized in Fig. 18 & 19. In case of bandwidth parameters of x(t), α_1 ranges from 0.05~0.85 and corresponding α_2 ranges from 0.1~0.7. The total number of stress spectra used in this simulation is 371 and the detail information on the shape parameters obtained from optimization are summarized in Appendix. A.

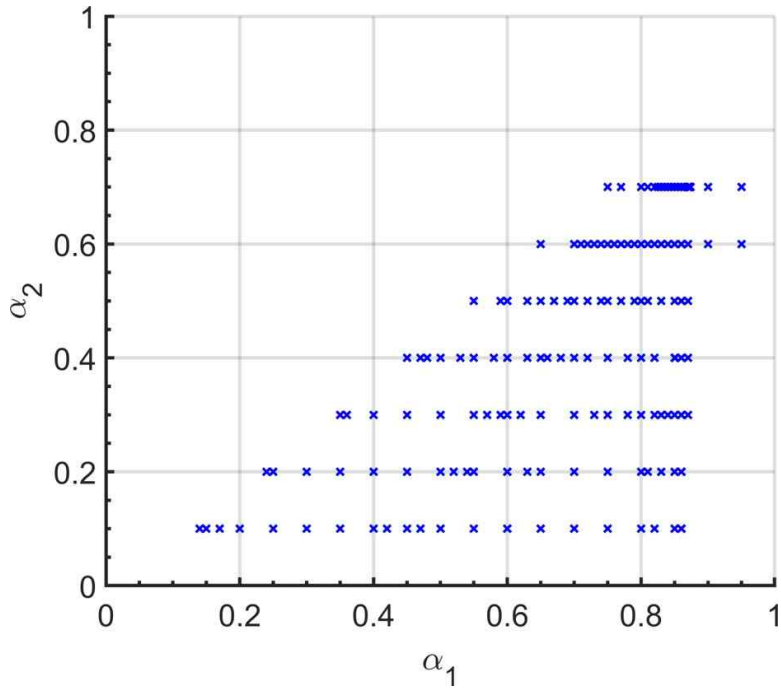

Fig. 18 The scatter plot of bandwidth parameters of x(t)

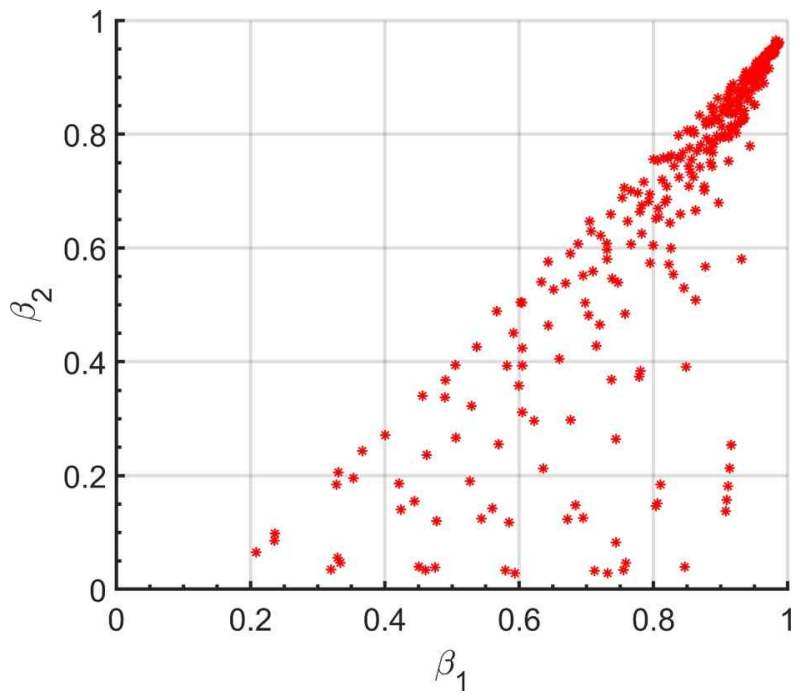

Fig. 19 The scatter plot of bandwidth parameters of the $\dot{x}$(t)

The well-known spectral representation is based on a discretized model of the target power spectral density function for the desired process. The simulation consists of the superposition of harmonic functions such as sine or cosine functions at discrete frequencies. There are two ways to determine amplitudes of each harmonic function: deterministic amplitude and random phase (DARP) and random amplitude and random phase (RARP) [Li and Kareem (1993)]. A zero mean stationary Gaussian process x(t) is simulated by RARP as shown in Eq. (4.1).

$$\mathrm{x}(t) = \sum_{i=1}^{n} (A_i \cos \omega_i t + B_i \sin \omega_i t) \tag{4.1}$$

where, $\mathrm{E}[A_i^2] = \mathrm{E}[B_i^2] = S(\omega_i)\Delta\omega, \mathrm{E}[A_i B_i] = 0, \mathrm{S}(\omega)$: power spectrum

In Eq. (4.1), the amplitudes of harmonic functions (A_i, B_i) are independent Gaussian random variables whose variances are equal to area near the discrete frequency ω_i. In DARP, the amplitude is determined by Eq. (4.2).

$$\mathrm{x}(t) = \sum_{i=1}^{n} (C_i \cos(\omega_i t + \phi_i)) \tag{4.2}$$

where, $C_i = \sqrt{2S(\omega_i)\Delta\omega}$

ϕ_i is random variable of uniform distribution between 0 to 2π. As the number of harmonic functions used in simulation increases, the realization random process will go to a Gaussian process through the

central limit theorem. Grigoriu (1993) commented that spectral representation through RARP is always Gaussian process regardless of the number of discrete frequency n while DARP approaches Gaussian process as n approaches infinity. Moreover, DARP is strongly ergodic while RARP is ergodic in the weak sense. Gurley (1997) compared two realization approaches and said that both models are adequate for the simulation of random processes under the condition that the number of frequencies is enough large and that $\Delta\omega$ is small enough to model the desired power spectral density.

In this present work, DARP is used to simulate random time signal x(t) and the number of frequencies is taken as 10,000. Time step and duration are also important parameters in simulation. Park (2011) tried to determine maximum sampling rate by comparing relative fatigue damages with different sampling rate. They concluded that 0.1 s is the maximum sampling rate and it is also applied in the present simulations. The simulation length for one short-term analysis is taken as 3 hours. Fig. 20 shows detail procedure for time simulation.

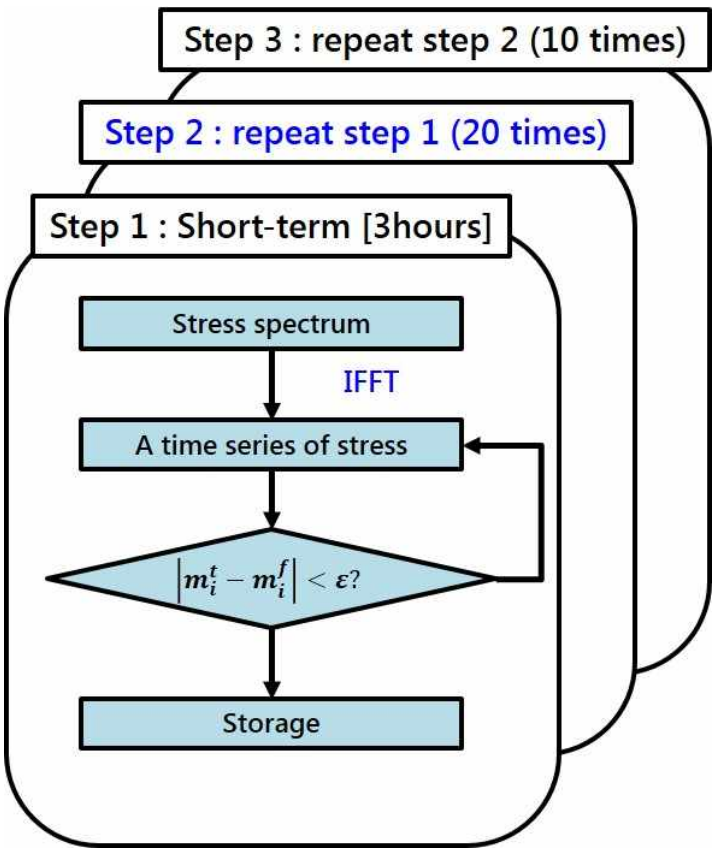

Fig. 20 Procedure for time simulation

Time simulation through DARP is performed during 3 hours and it is called short-term analysis. Then, statistical properties of generated random process $\sigma_X, \sigma_{\dot{X}}, \sigma_{\ddot{X}}$ are compared to corresponding target spectral parameters from the given power spectral density. The relationships between them are given in Eq. (3.5) and (3.6). 5% errors are allowed between them and if the generated time history do not satisfy the criteria, the time series data is disregarded.

Due to inherent uncertainty in time simulation, short-term analysis should be repeated in several times. Park et al (2014) defined one data block as 20 times of short-term analyses to get

stable results. Every short-term analysis, the random phases (ϕ_i), frequency step ($\Delta\omega$) and representative frequency of each bin (ω_i) should be changed to avoid repeatability of time signal. Finally, 10 data blocks are calculated in each stress spectrum.

4.2.2. Determination on the form of approximate model

By the laws of conditional probability as seen in Eq. (4.3), joint probability distribution of mean and amplitude $\left(p_{s,m}^{RFC,G}(s,m)\right)$ is calculated by multiplying marginal distribution of rainflow amplitude $\left(p_{s}^{RFC,G}(s)\right)$ and conditional probability density function of rainflow mean given amplitude $\left(p_{m|s}^{RFC,G}(m|s)\right)$.

$$p_{s,m}^{RFC,G}(s,m) = p_{s}^{RFC,G}(s) \times p_{m|s}^{RFC,G}(m|s) \tag{4.3}$$

Many approximate models derived in Gaussian processes have concentrated on the marginal distribution of rainflow amplitude and some model give a good agreement on actual data. Thus, in this works, we tried to find an approximate model for conditional probability density function of rainflow mean given amplitude. After making model for $p_{m|s}^{RFC,G}(m|s)$, $p_{s,m}^{RFC,G}(s,m)$ could be estimated by the proposed model with the existing model for $p_{s}^{RFC,G}(s)$.

Fig. 21 shows some examples of scatter plots of normalized rainflow mean and amplitude in various stress spectra having

different bandwidth parameters.

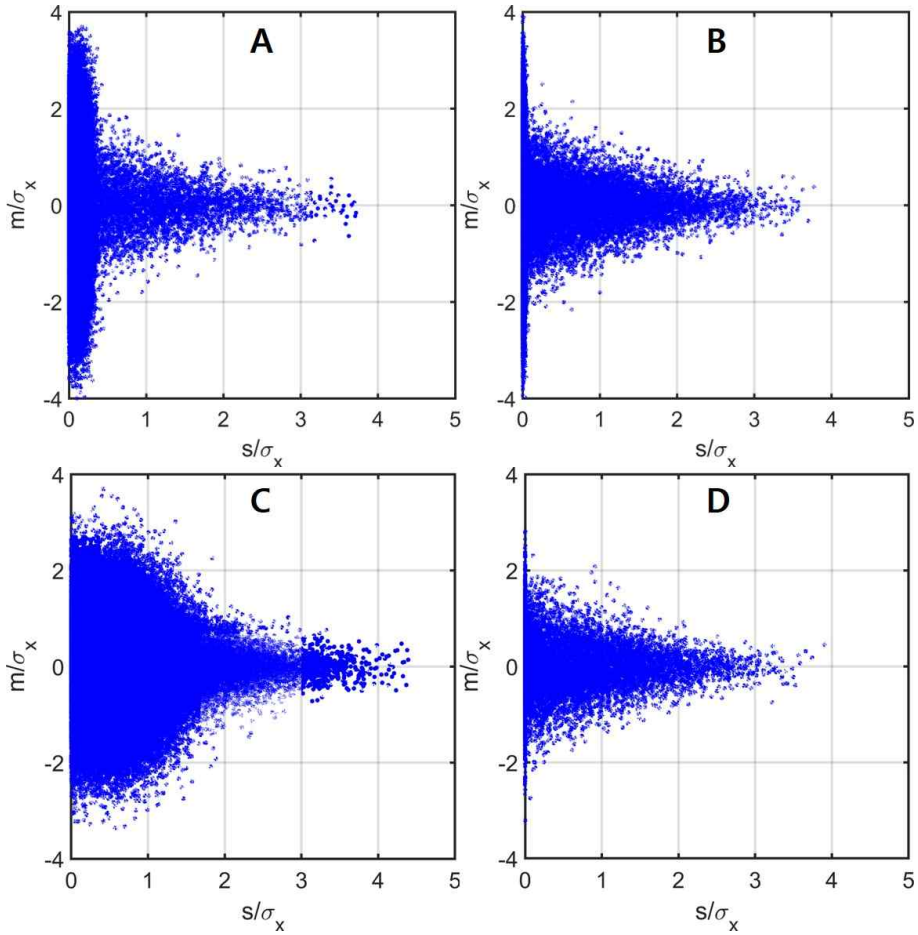

Fig. 21 Scatter plots of rainflow mean and amplitude in various stress spectra having different bandwidth parameters. [(α_1, α_2) = (0.25, 0.1) [A]; (0.75, 0.1) [B]; (0.6, 0.5) [C]; (0.83, 0.5) [D];]

In random processes that are close to wide-band processes expressed in the 1st and 2nd cases, large amount of stress cycles seems to concentrate on small amplitude region. There are many peaks between successive upcrossings in wide-band process so the number of stress cycles is larger than in narrow-band process.

Although the 1st and 2nd stress spectra have the same irregularity factor, two scatter plots are totally different. It means that the 1st bandwidth parameter (α_1) also has on effect on the joint probability distribution. When it goes to one, observed number of stress cycles in large amplitude region seem to increase. In contrast to the 1st and 2nd case, the random histories generated form the 3rd and 4th stress spectra are close to narrow-band process. When it goes to narrow-band process, observed number of stress cycles in large amplitude region increase because small number of peaks exist between upcrossings.

The extracted stress cycles are grouped into sample set where rainflow cycles have the same level of normalized rainflow amplitude. Histograms are plotted in each sample set and probability distribution fitting is tried to find the best-fit model for the histograms. Fig. 22 shows examples of histograms. Among various types of distribution, zero-mean normal distribution is the best fitting model for conditional probability density function of rainflow mean. Therefore, in this work, $p_{m|s}^{RFC,G}(m|s)$ is assumed to be zero-mean normal distribution as Eq. (4.4).

$$p_{m|s}^{RFC,G}(m|s) = \frac{1}{\sqrt{2\pi\sigma_{m|s}^2}} e^{-\frac{x^2}{2\sigma_{m|s}^2}} \tag{4.4}$$

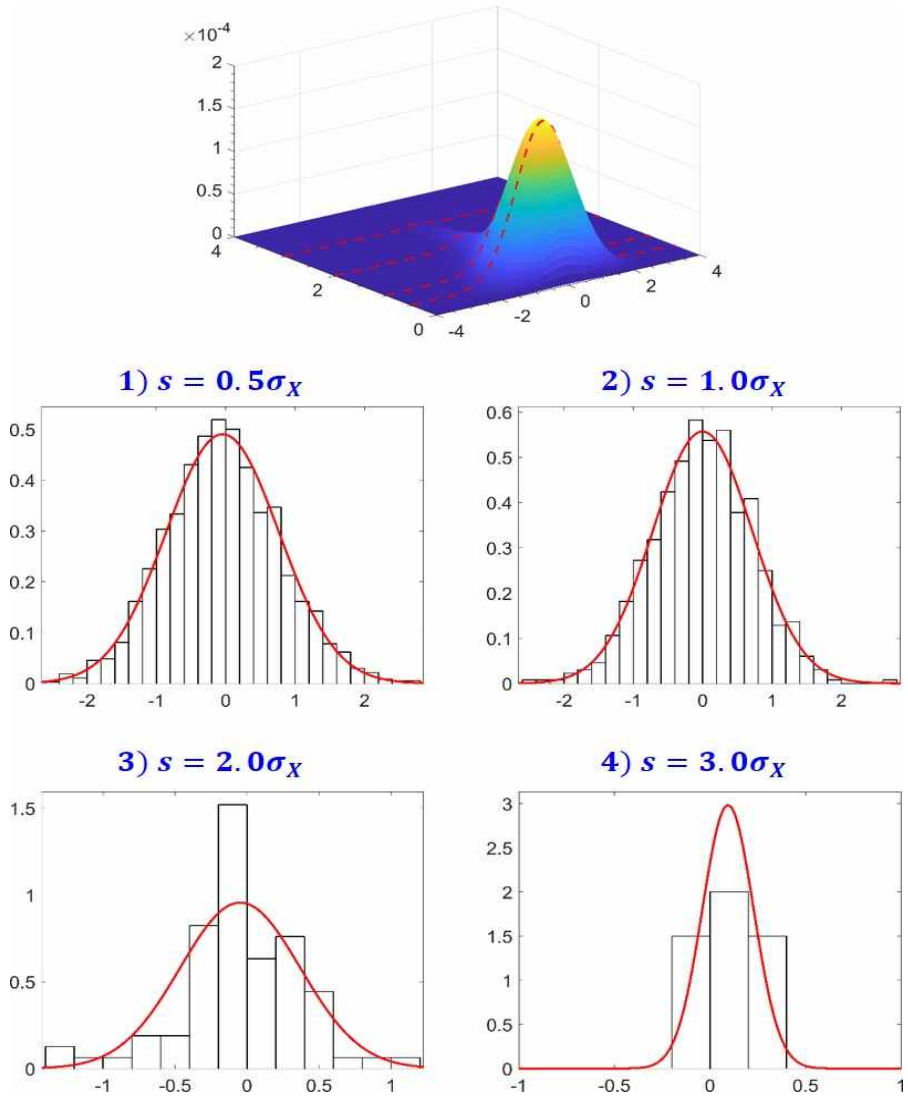

Fig. 22 Histogram plots of rainflow mean at different normalized amplitude and normal distribution fitting results

4.2.3. Regression analysis on standard deviation

The only unknown variable is standard deviation $(\sigma_{m|s})$. Fig. 23 shows $\sigma_{m|s}$ of stress spectra in Fig. 21. The observed shapes of $\sigma_{m|s}$ in different stress spectra seem to be totally changed. Thus, to

determine the conditional PDF of rainflow mean, it is needed to derive the relationship between $\sigma_{m|s}$ and spectral parameters from given power spectral density.

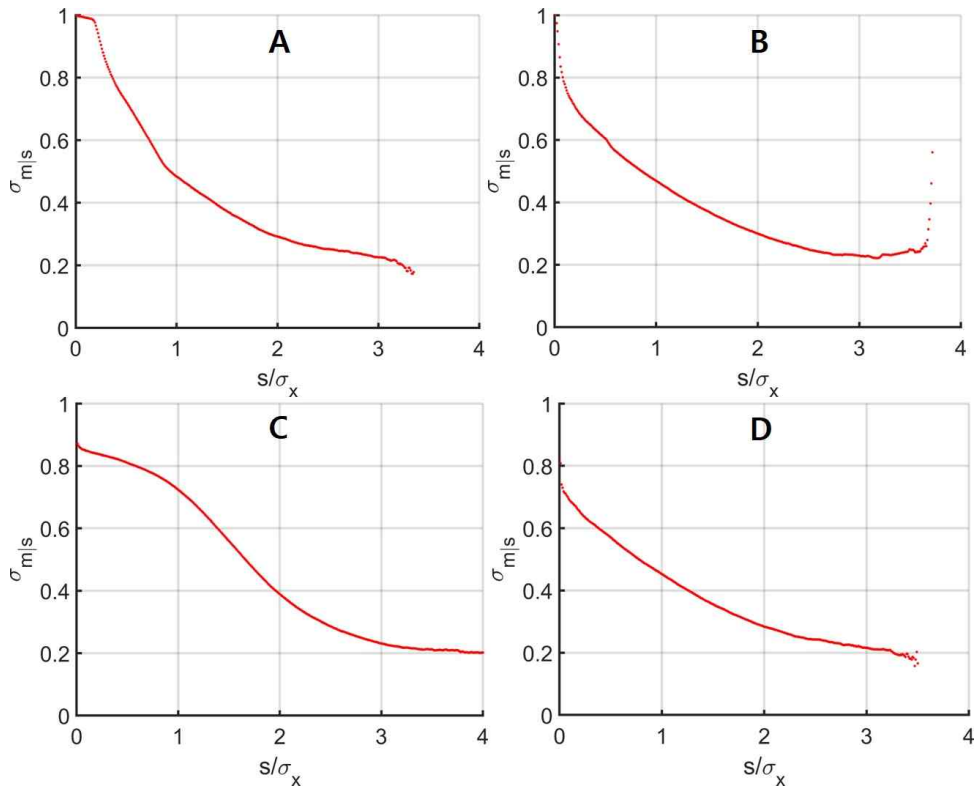

Fig. 23 Standard deviations of conditional PDF of mean in various stress spectra having different bandwidth parameters [(α_1, α_2) = (0.25, 0.1) [A]; (0.75, 0.1) [B]; (0.6, 0.5) [C]; (0.83, 0.5) [D];]

At first, sensitivity analysis is performed to find important parameters which have a large effect on the $\sigma_{m|s}$ value. From other literature for probabilistic models in Gaussian process, the 1st and 2nd bandwidth parameters (α_1, α_2) are investigated at first. Fig. 24 shows the changes in $\sigma_{m|s}$ with different α_1 values. When α_1 goes to unity,

$\sigma_{m|s}$ tends to decrease rapidly in small amplitude region. In high amplitude region, $\sigma_{m|s}$ seems to be converged the same value regardless of α_1. The y−intercept value seems to be not change with different α_1 values.

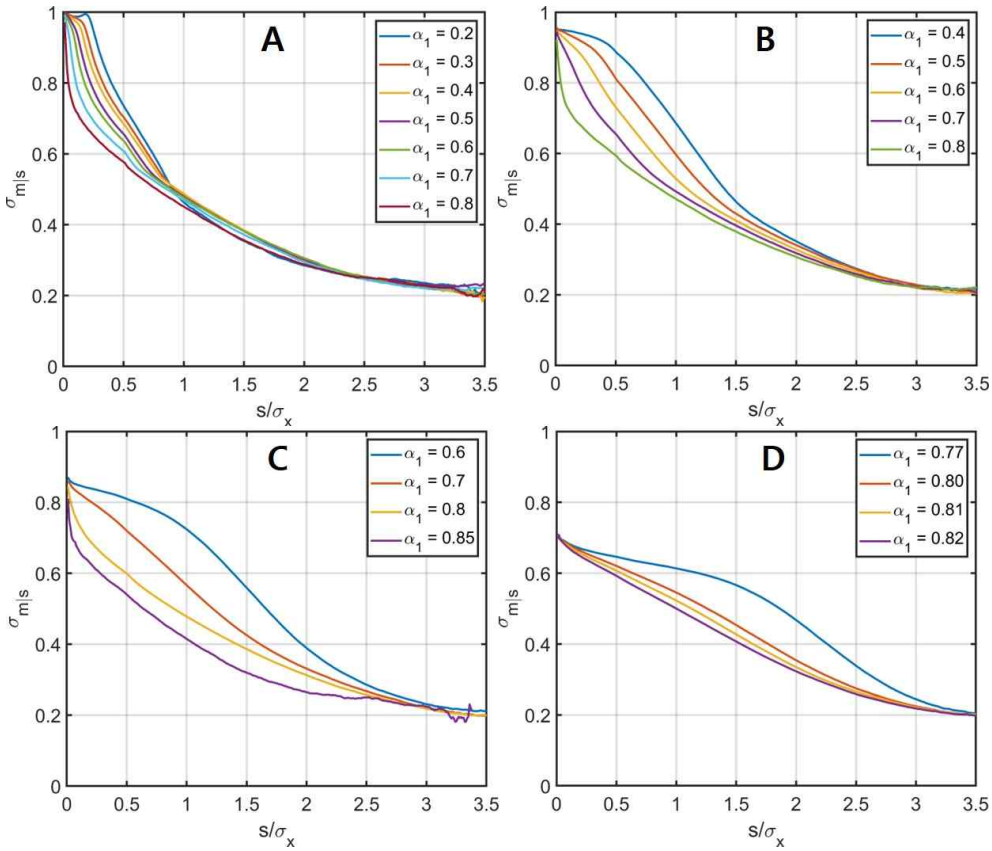

Fig. 24 The changes in $\sigma_{m|s}$ with different α_1 values

[α_2 = 0.1 [A]; 0.3 [B]; 0.5 [C]; 0.7 [D];]

On the other hand, y−intercept value tend to decreases as α_2 increases as seen in Fig. 25. α_2 also affects the slope of $\sigma_{m|s}$ in mid amplitude region.

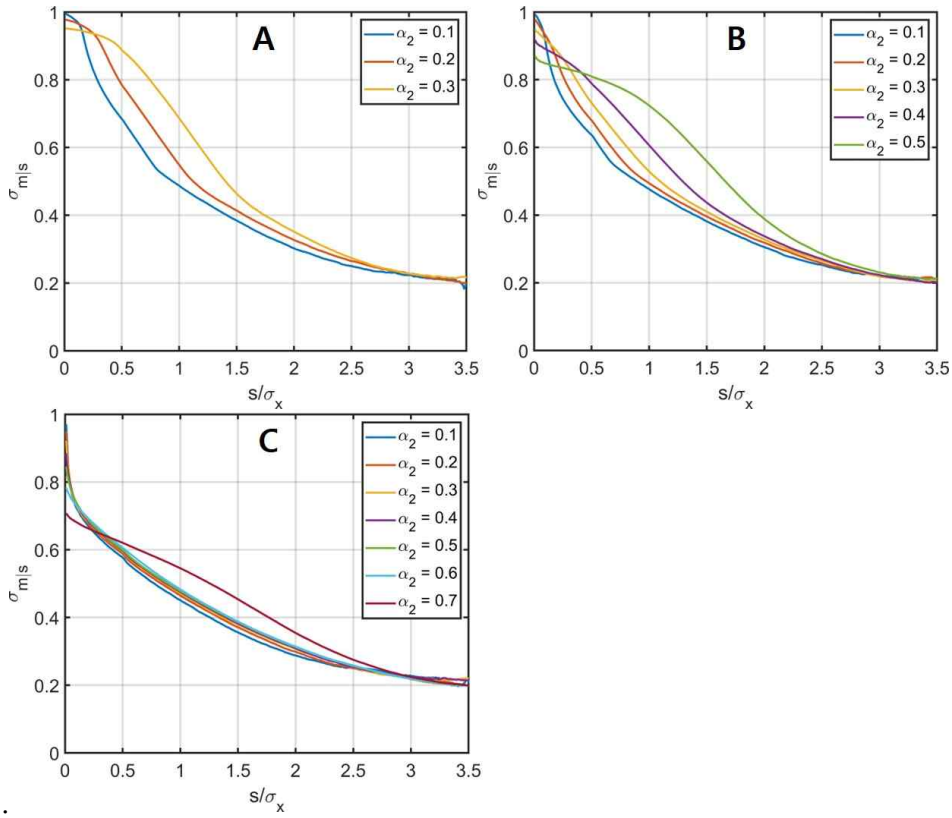

Fig. 25 The changes in $\sigma_{m|s}$ with different α_2 values

[α_1 = 0.4 [A]; 0.6 [B]; 0.8 [C];]

The five stress spectra used in time simulations are constructed to match target the 1st and 2nd bandwidth parameters (α_1, α_2). The choice of different spectral density shape makes it possible to make stress spectra which have the same α_1, α_2 and different $q_{\dot{X}}$ defined in Eq. (3.14) which related to bandwidth parameters of the 1st derivative of x(t). In Fig. 26, observed $\sigma_{m|s}$ in five different shapes of stress spectra having the same α_1, α_2 are compared. In five stress spectra, there is no significant difference in $q_{\dot{X}}$ except Type 5 spectrum. When $q_{\dot{X}}$ decreases, the observed $\sigma_{m|s}$ also tend to decreases rapidly. Thus, in derivation on condition PDF of rainflow

mean, $q_{\dot{X}}$ should be included as a input variable.

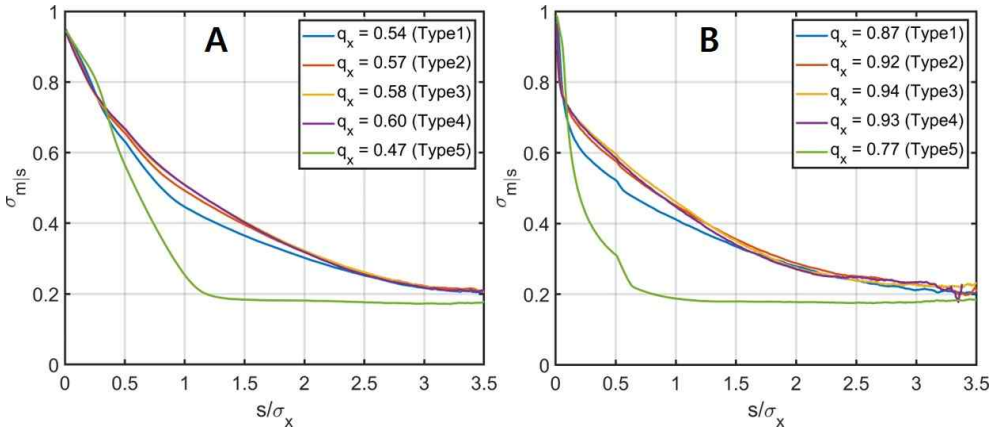

Fig. 26 The changes in $\sigma_{m|s}$ with different q_X values

[(α_1, α_2) = (0.7, 0.3) [A]; (0.8, 0.1) [B];]

Finally, the input variables of the standard deviation of conditional PDF $\sigma_{m|s}$ are determined as α_1, α_2 and $q_{\dot{X}}$. Next step is making a regression model for $\sigma_{m|s}$ with these input spectral parameters. The procedure for regression analysis is summarized in Fig. 27.

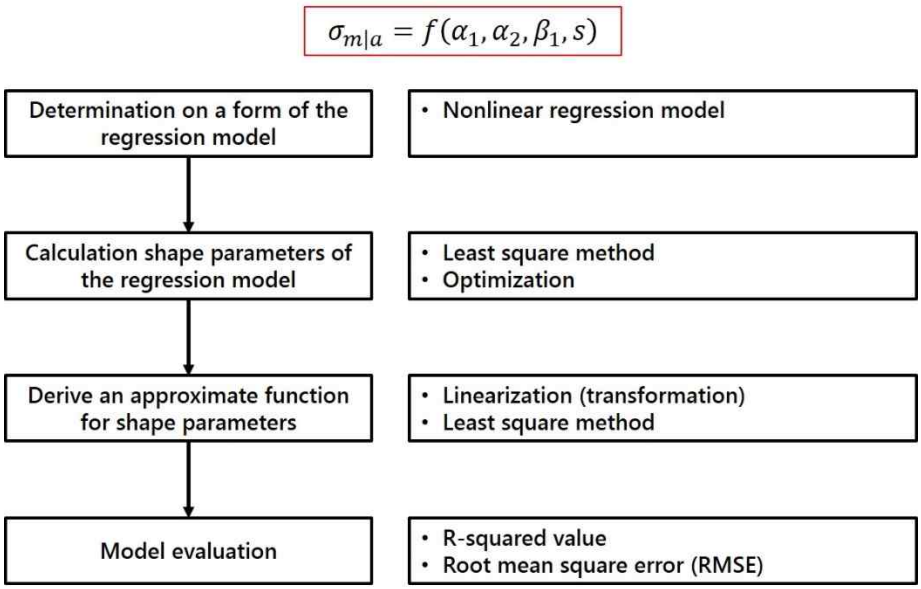

Fig. 27 Procedure for regression analysis on $\sigma_{m|s}$

The first step is to determine the form of the regression model for $\sigma_{m|s}$. From its shape, linear regression model is not adequate to express $\sigma_{m|s}$. Various shape of non−linear function families are introduced to describe the shape of $\sigma_{m|s}$ and among them, logit−log model is selected for our problem. This model was proposed for describing the concentration of an agrochemical material in soil samples. It has three shape parameters as seen in Eq. (4.5) and some examples of different shape of logit−log model are described in Fig. 28.

$$h(x;\theta_1,\theta_2,\theta_3) = \begin{cases} \theta_1 & \text{if } x = 0 \\ \dfrac{\theta_1}{1+\exp(\theta_2+\theta_3 \ln x)} & \text{if } x > 0 \end{cases} \tag{4.5}$$

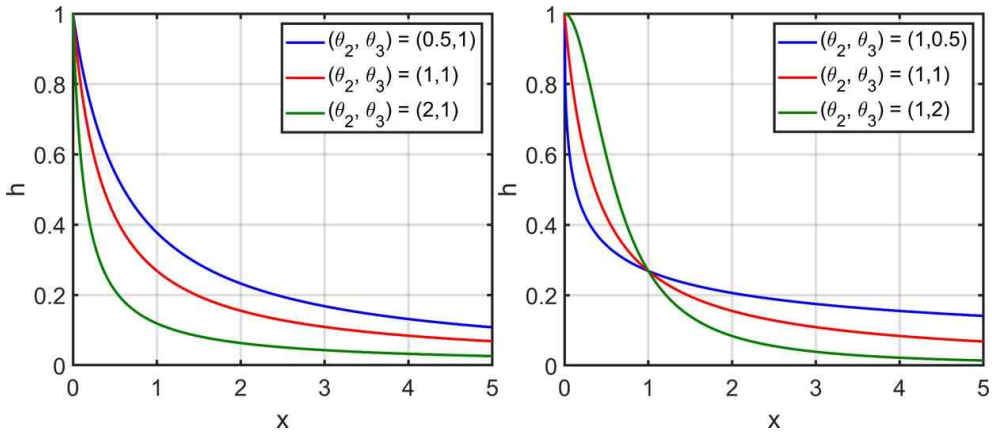

Fig. 28 Shapes of logit−log models with different shape parameters

Shape parameters of each stress spectra are calculated by least square method and some examples of comparison between actual and regressed $\sigma_{m|s}$ are suggested in Fig. 29. Except very large amplitude region where the simulated results are unstable due to lack of data, the regression model through least square method give a very good agreement on the actual data.

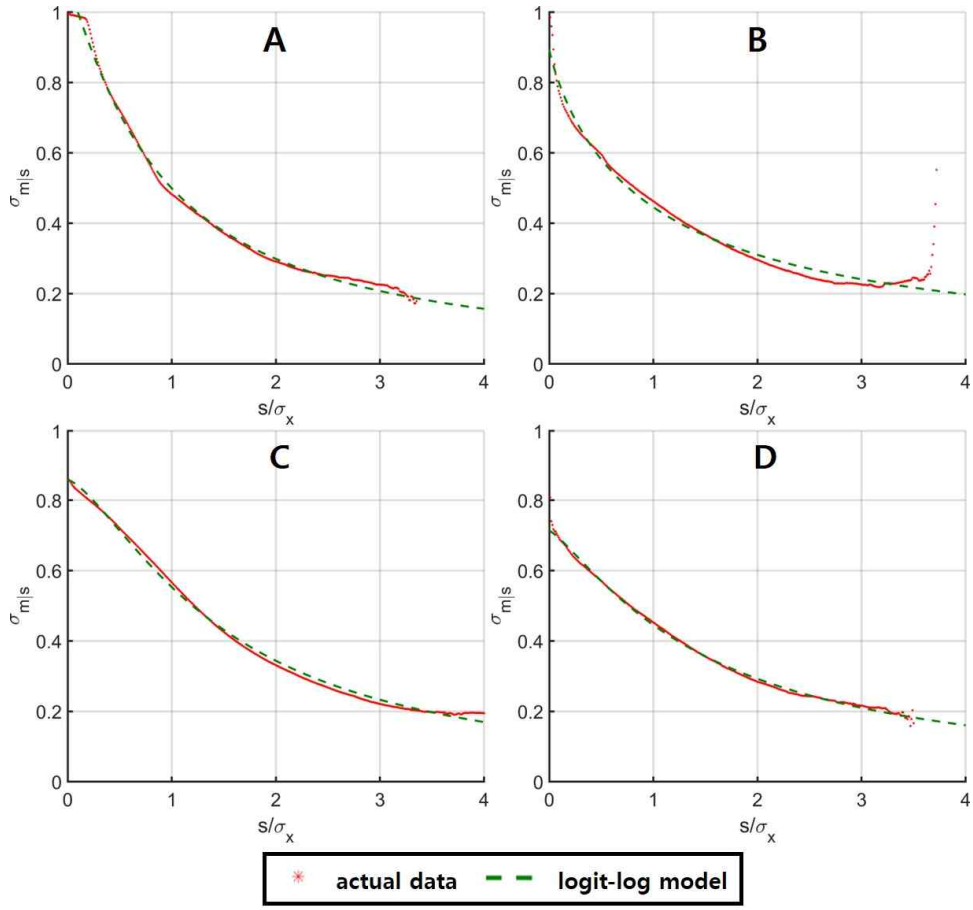

Fig. 29 Simulated (red line) and regressed (green line) standard deviations in different stress spectra [(α_1, α_2) = (0.25, 0.1) [A]; (0.75, 0.1) [B]; (0.6, 0.5) [C]; (0.83, 0.5) [D];]

The next step is making relationship between shape parameters $(\theta_1, \theta_2, \theta_3)$ of logit−log model and input variables $(\alpha_1, \alpha_2, q_{\dot{X}})$.

- Regression on $\boldsymbol{\theta_1}$

The 1st shape parameter θ_1 is related to y−intercept of logit−log model and Fig. 30 shows the changes in θ_1 with three input

variables. As mentioned in sensitivity analysis, y−intercept is strongly related to α_2 and other two spectral parameters seem to have a little effect on θ_1 value. Although small deviations are observed in high range of α_1 and $q_{\dot{X}}$, θ_1 is assumed to be a function of α_2 only as shown in Eq. (4.6).

$$\theta_1^{\text{app}}(\alpha_2) = -0.728\alpha_2^{2.6} + 0.980 \tag{4.6}$$

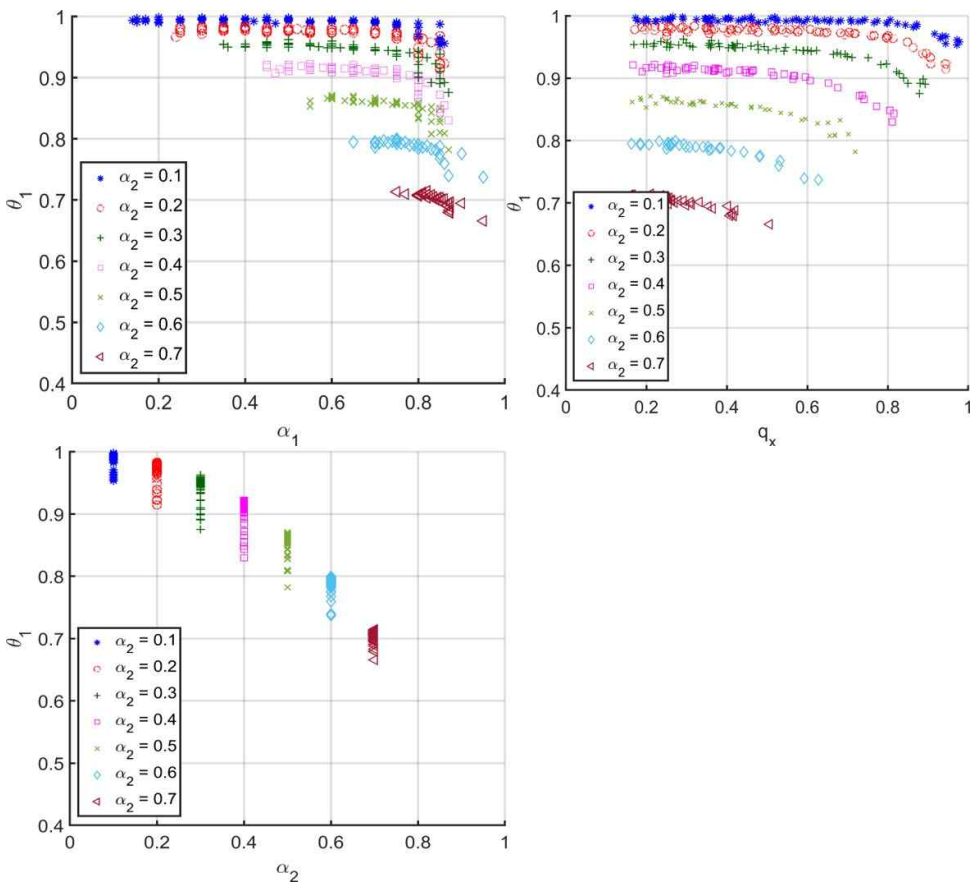

Fig. 30 Scatter plots of θ_1 and input variables

Averaged values of θ_1 which share the same α_2 value are used to regression model for θ_1. The regression results and R−square

value are summarized in Fig. 31.

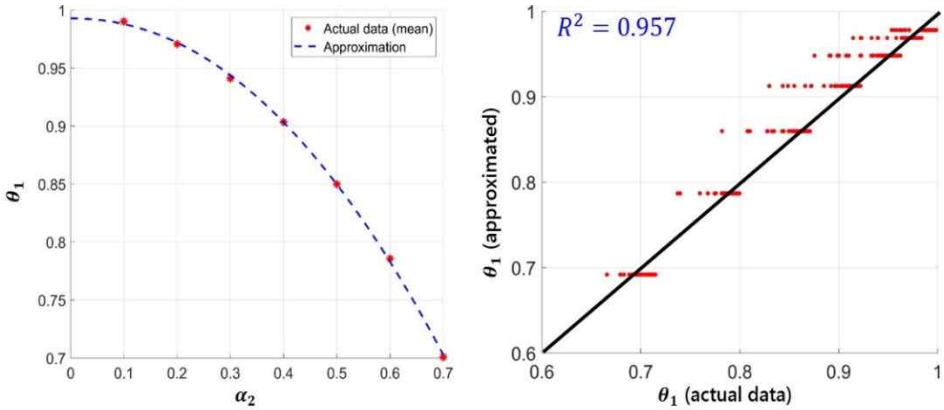

Fig. 31 The results of regression analysis on θ_1

- Regression on $\boldsymbol{\theta_2}$

Second shape parameter θ_2 determines the slope of regression model in mid amplitude region. The estimated θ_2 by least square method are plotted in Fig. 32. Unfortunately, θ_2 depends on three input variables at the same time. Thus, linearization of θ_2 is performed through transformation to simplify this problem.

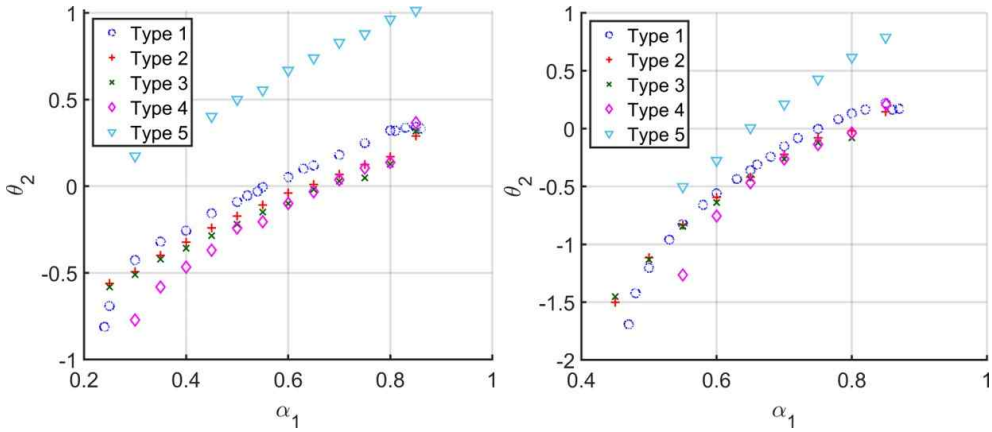

Fig. 32 Scatter plots of θ_2 and input variables

[α_2 = 0.2 (left); α_2 = 0.4 (right)]

Various nonlinear transformations are investigated and the best transformation function is determined by trial-and-error method. Through the transformation shown in Eq. (4.7), scattered data as shown in Fig. 32 could be transformed to lines shown in Fig. 33.

$$\theta_2(\alpha_1, \alpha_2, q_{\dot{X}}) \rightarrow \sqrt{1-\theta_2} - q_{\dot{X}} = f(\alpha_1, \alpha_2) \tag{4.7}$$

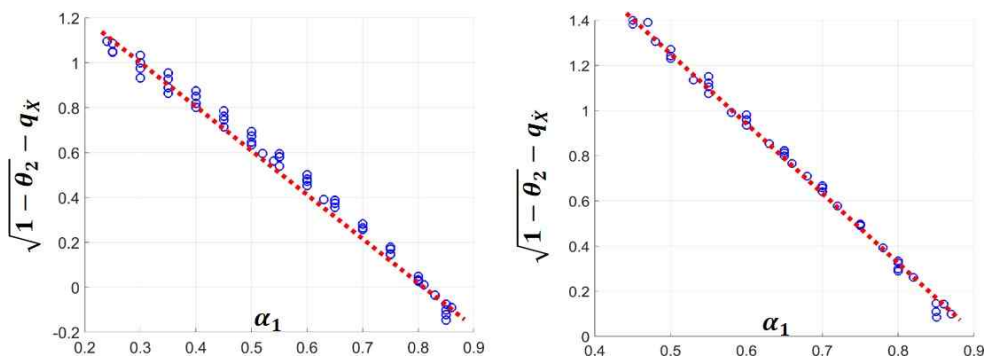

Fig. 33 Linearized θ_2 through non-linear transformation [α_2 = 0.2

(left); α_2 = 0.4 (right)]

Finally, the slope and y−intercept of linearized output variable are expressed as functions of α_1, α_2 as shown in Eq. (4.8). The R−squared value of the regression model for θ_2 is 0.971 in this work.

$$\sqrt{1-\theta_2^{\text{app}}} - q_{\dot{X}} = m(\alpha_2)(\alpha_1 - \alpha_2) + n(\alpha_2) \tag{4.8}$$

where, $\mathrm{m}(\alpha_2) = -1.13\exp(2.58\alpha_2), \mathrm{n}(\alpha_2) = -1.2\exp\left(-\left(\frac{\alpha_2 - 0.77}{0.8}\right)^2\right)$

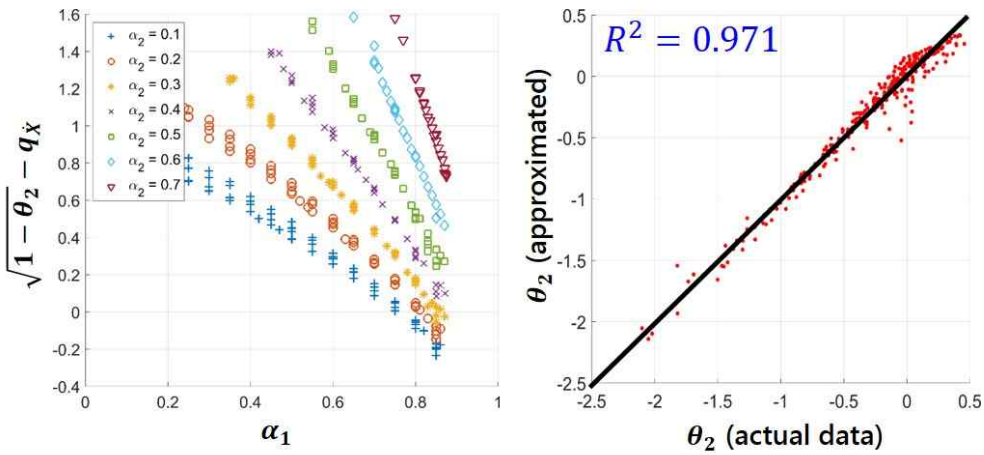

Fig. 34 Linearized θ_2 in all spectra (left) and R−squared value of the regression model for θ_2 (right)

- Regression on θ_3

Third shape parameter θ_3 determines the slope of regression model in small amplitude region. The estimated θ_3 by least square method are plotted in Fig. 35. θ_3 also depends on three input

variables at the same time. Thus, linearization of θ_3 is also performed through transformation to simplify this problem.

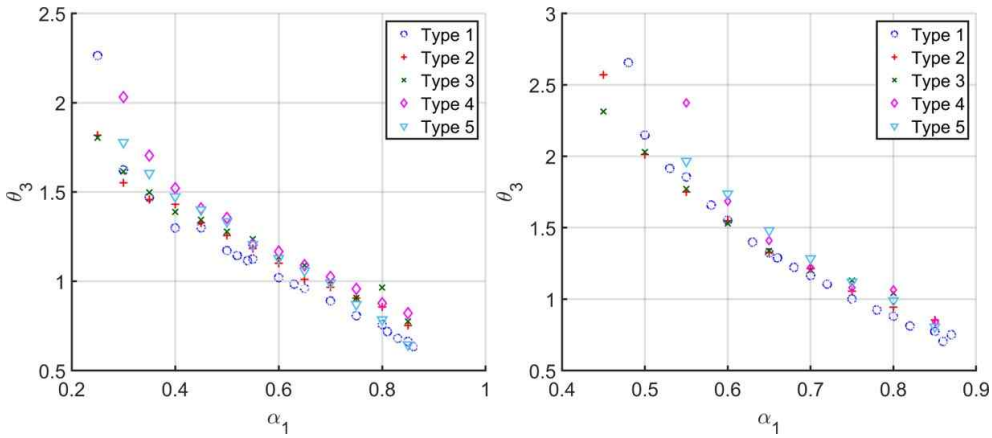

Fig. 35 Scatter plots of θ_3 and input variables [α_2 = 0.2 (left); α_2 = 0.4 (right)]

By subtracting $q_{\dot{X}}$ from θ_3, it could be easily linearized as shown in Fig. 36. However, as α_2 approaches to α_1, the observed θ_3 is largely deviated from the line. To prevent distortion due to the these points, simulation results obtained from stress spectra where the difference between α_1 and α_2 is smaller than 0.1 are excluded in regression analysis for θ_3. This effect of the assumption is discussed later.

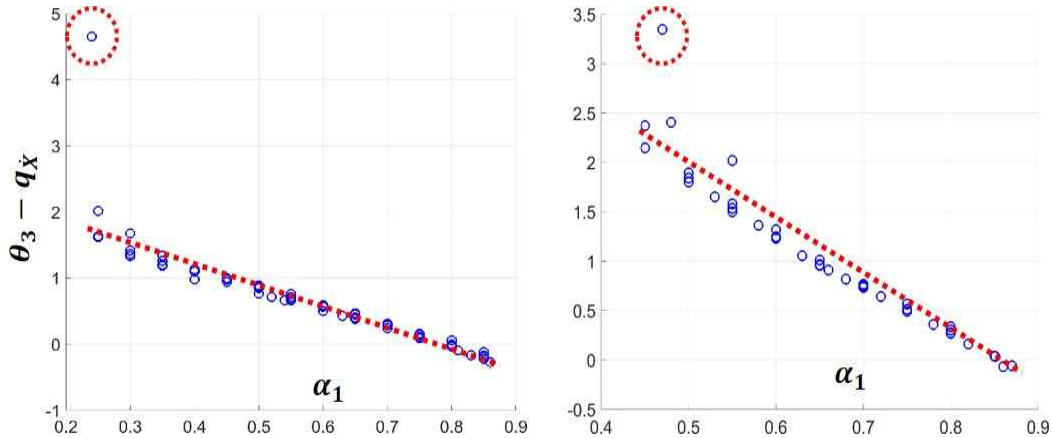

Fig. 36 Linearized θ_3 through non-linear transformation [α_2 = 0.2 (left); α_2 = 0.4 (right)]

The slope and y-intercept of linearized output variable are expressed as functions of α_1, α_2 as shown in Eq. (4.9). The R-squared value of the regression model for θ_2 is 0.934 excluding stress spectra where the difference between α_1 and α_2 is smaller than 0.1 and 0.819 in considering all stress spectra.

$$\theta_3^{\text{app}} - q_{\dot{X}} = p(\alpha_2)\alpha_1 + q(\alpha_2) \tag{4.9}$$

where, $\mathrm{p}(\alpha_2) = -1.59\exp(2.88\alpha_2), \mathrm{q}(\alpha_2) = 1.2\exp(3.15\alpha_2)$

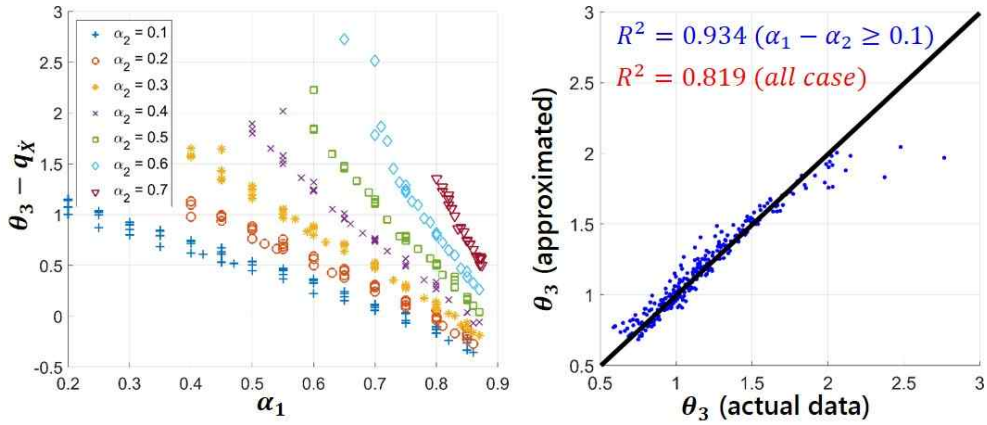

Fig. 37 Linearized θ_3 in all spectra (left) and R−squared value of the regression model for θ_3 (right)

Finally, the standard deviation of conditional PDF of rainflow mean is derived by substituting Eq. (4.6), (4.8) and (4.9) into (4.5) as shown in Eq. (4.10).

$$\sigma_{m|s}(s, \alpha_1, \alpha_2, q_{\dot{X}}) = \begin{cases} \theta_1^{\text{app}} & \text{if } s = 0 \\ \dfrac{\theta_1^{\text{app}}}{1 + exp\left(\theta_2^{\text{app}} + \theta_3^{\text{app}} \ln x\right)} & \text{if } s > 0 \end{cases} \tag{4.10}$$

Actual and estimated $\sigma_{m|s}$ are compared in Fig. 38. Because the stress spectra whose α_1, α_2 is close within 0.1 are excluded in the derivation on θ_3^{app}, some errors are observed in the left figure. However, errors tend to decrease when α_1 goes to unity. In other region as shown in middle and right figure in Fig. 38, the approximate model gives very accurate estimation on actual $\sigma_{m|s}$.

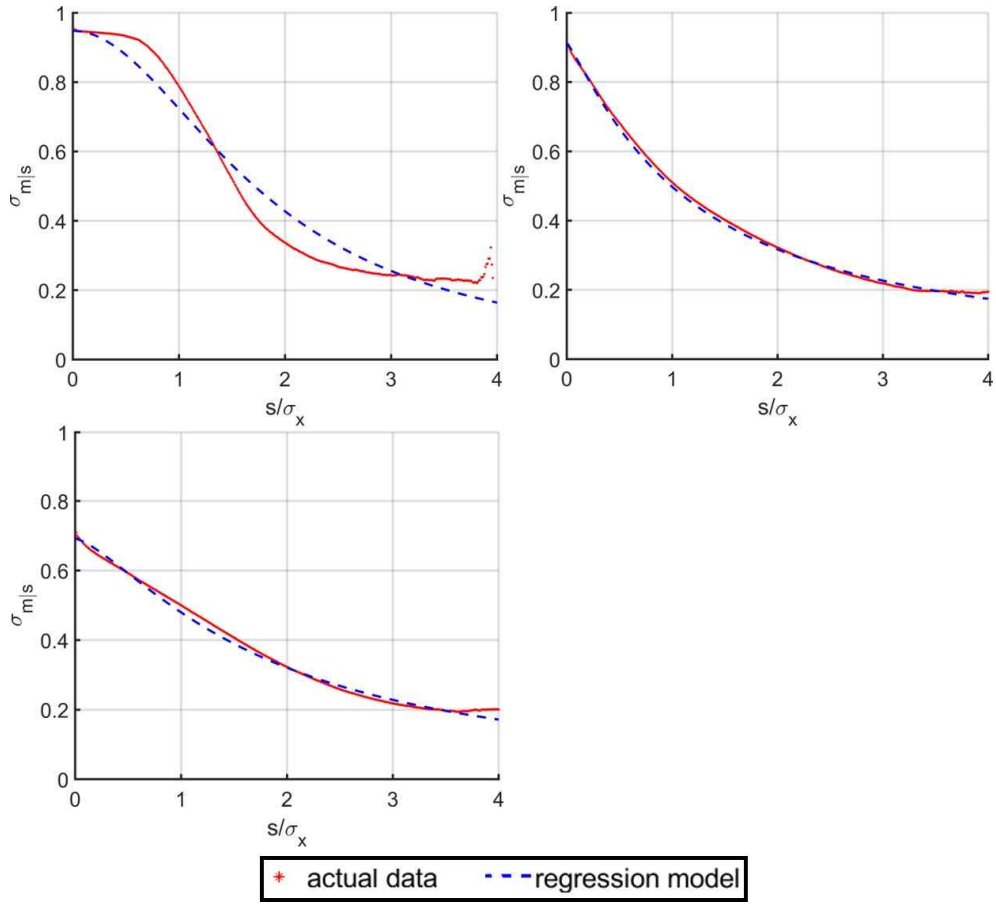

Fig. 38 Comparison between observed and estimated standard deviation of conditional PDF of rainflow mean ($(\alpha_1, \alpha_2, q_X)$= (0.35,0.3,0.2) [left−upper], (0.7, 0.4, 0.45) [right−upper], (0.82, 0.7, 0.23) [left−lower])

4.3. Joint probability distribution of mean & amplitude

As described in Eq. (4.3), joint probability distribution is derived by multiplying marginal distribution and conditional PDF of rainflow mean. In this work, $p_{RFC}^{BT}(s)$ is used to make joint probability distribution and the selection of approximate model for $p_s^{RFC}(s)$ is

discussed in Chapter 6.

Fig. 39 and 40 compares estimated joint probability distributions by two approximate models (proposed and BT model) and observed scatter plots of rainflow mean and amplitude. From Fig. 39 and 40, the proposed model seems to give better representation on the actual scatter plot by modifying the information of rainflow mean distribution.

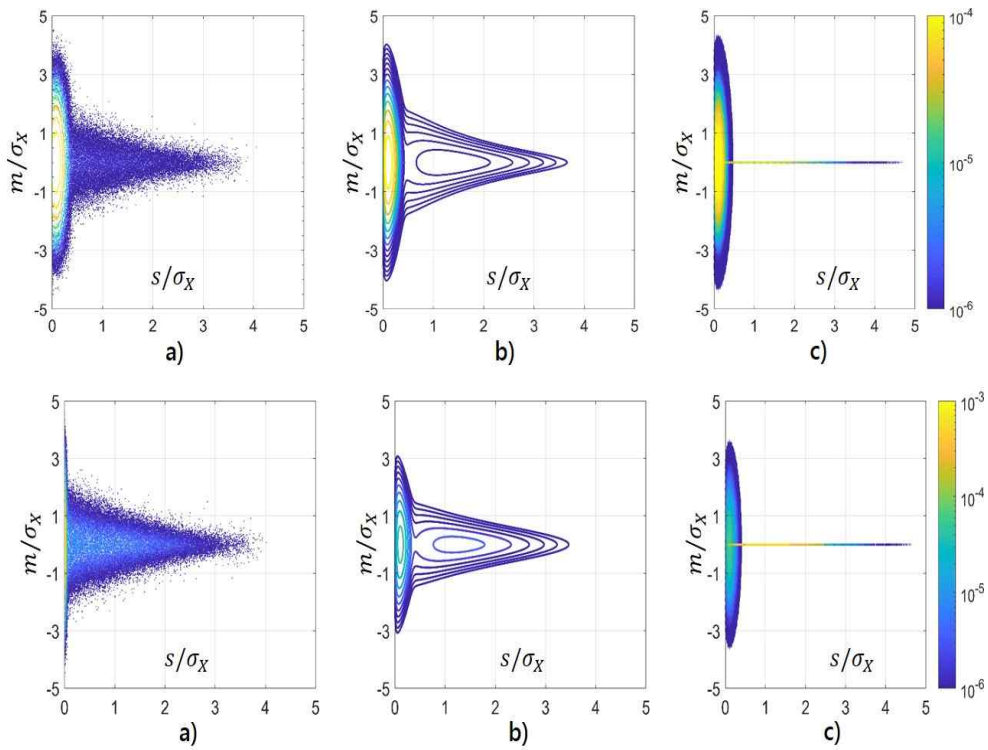

Fig. 39 Scatter plots of simulated (a) and estimated joint probability distribution through the proposed model (b) and the Benasciutti & Tovo model (c) [$(\alpha_1, \alpha_2)=(0.25,0.1)$; (upper), $(0.75,0.1)$ (lower)]

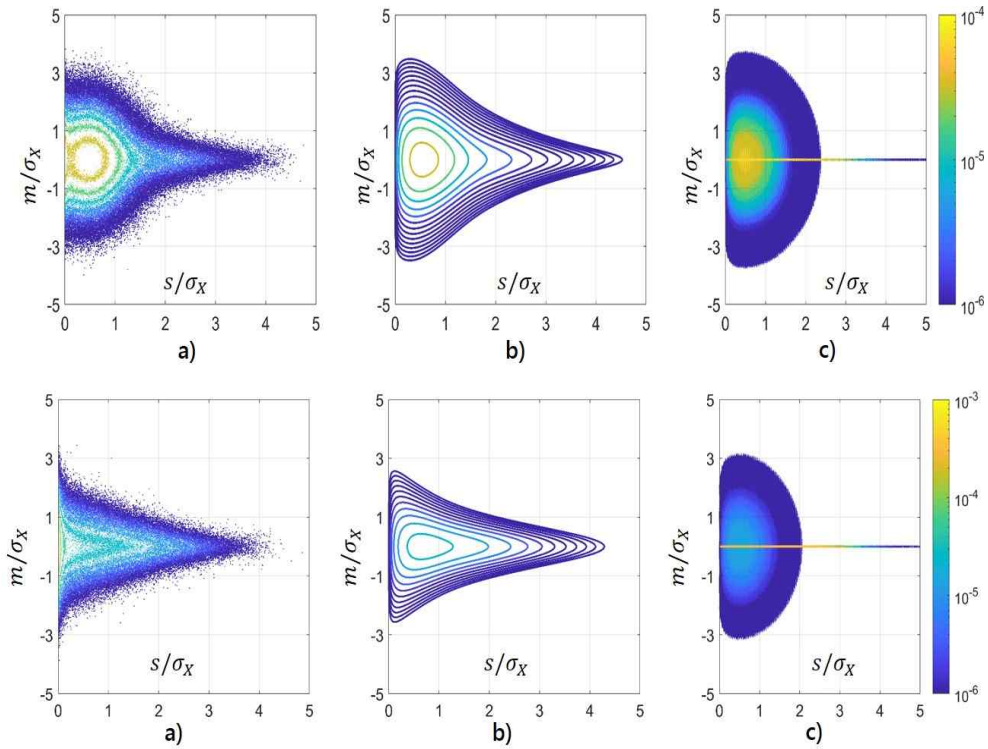

Fig. 40 Scatter plots of simulated (a) and estimated joint probability distribution through the proposed model (b) and the Benasciutti & Tovo model (c) [$(\alpha_1, \alpha_2) = (0.6, 0.5)$; (upper), (0.8,0.5) (lower)]

The accuracy of the proposed model is also evaluated in quantitative way. The root-mean-squared-error (RMSE) defined as Eq. (4.11) of two approximate models are compared in total 371 numbers of stress spectra used in simulation. The RMSEs are summarized in Table 1.

$$\mathrm{RMSE} = \frac{1}{N_{\mathrm{spectrum}}} \sqrt{\sum_{i=1}^{p} \sum_{j=1}^{q} \left(p_{a,m}^{\mathrm{est}}(s_i, m_i) - p_{a,m}^{\mathrm{sim}}(s_i, m_i) \right)^2} \tag{4.11}$$

Table 1 RMSE of two approximate models

Spectrum type (number of spectrum)	RMSE [BT model]	RMSE [Proposed model]	Ratio ($\frac{RMSE_{prop}}{RMSE_{BT}} \times 100$ [%])
Type 1 (131)	0.0253	0.0083	32.7%
Type 2 (64)	0.0209	0.0094	44.9%
Type 3 (59)	0.0195	0.010	51.2%
Type 4 (53)	0.0231	0.0121	52.5%
Type 5 (64)	0.0226	0.0066	29.1%

4.4. Fatigue damage estimation considering mean stress correction

As describe in Chapter 2.1, mean stress effect is an important factor in assessment of fatigue life. Most S-N curves have been constructed by fatigue tests under fully reversed loading cycles so mean stress correction should be considered when target structure is under non-zero loading cycles.

Nieslony and Bohm (2015) summarized three methods in dealing with mean stress correction in fatigue life estimation:

1) without compensating for the mean stress
2) transformation of stress amplitude in regards to each stress cycle and its mean stress value after cycle counting
3) transformation of stress amplitude with global mean stress value before cycle counting

They also mentioned that the last two methods give equally good results. However, the last one which utilizes global mean stress value has been preferred in practice so related regulations suggests reduction factor for the mean stress effect as a function of global mean stress value [DNV (2011)]. In the second method, the mean values of each stress cycle are required to reflect the mean stress effect in estimation on fatigue damages. Thus, marginal probability density function of stress amplitude is no sufficient for this method and joint probability distribution of stress mean and amplitude is needed.

Fatigue damage analysis considering the mean stress correction is also performed in idealized five stress spectra to verify the accuracy of the proposed joint probability distribution model. Without the mean stress correction, fatigue damages estimated the proposed model are the same the damages calculated by BT model because the proposed model uses the marginal distribution of stress amplitude by Benasciutti & Tovo. Among several transformation models for mean stress correction, reduction factor recommended in DNV-RP-C203 is used in this case study. The reduction factor is defined as shown in Eq. (4.12). The effective stress amplitude reflecting the mean stress correction is calculated by multiplying the original stress amplitude with the corresponding reduction factor as shown in Eq. (4.13). As mean value decreases, which means that the stress cycle goes to compression-compression cycle, the effective stress amplitude decreases.

$$f_m = \frac{\sigma_t + 0.6\sigma_c}{\sigma_t + \sigma_c} \tag{4.12}$$

where, f_m: reduction factor,

σ_t: maximum tension stress

σ_c: maximum compression stress

$$s_{eff} = f_m \times s \tag{4.13}$$

where, s_{eff} : effective stress amplitude

Fig. 41 shows an example of scatter plots of mean and amplitude of rainflow counted cycles before and after mean stress correction through the reduction factor. The time series data are generated from the 4th stress spectrum whose the 1st and 2nd bandwidth parameters are 0.6 and 0.1 respectively. As mentioned above, the effective stress amplitudes of stress cycles whose mean values are smaller than zero decreases after the mean stress correction. On the other hands, the effective stress amplitude of stress cycles under tensile state remains so the whole shape of scatter plot is no longer symmetric. Changes in fatigue damages without and with mean stress correction are compared in Fig. 42.

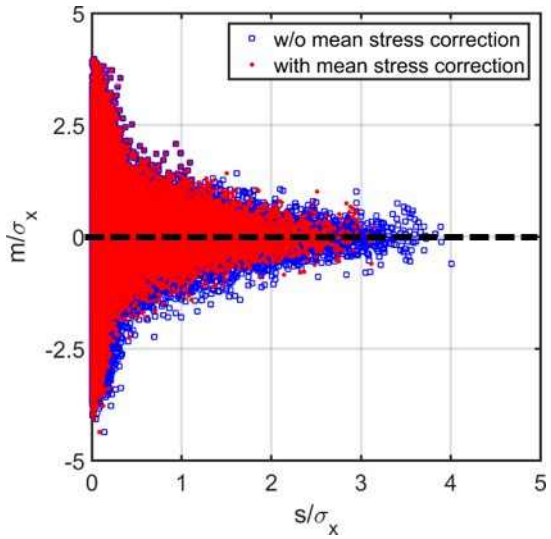

Fig. 41 Scatter plots of mean and amplitude of rainflow−counted−cycles before (blue) and after (red) mean stress correction. [Type 4 − (α_1, α_2) = (0.6,0.1))

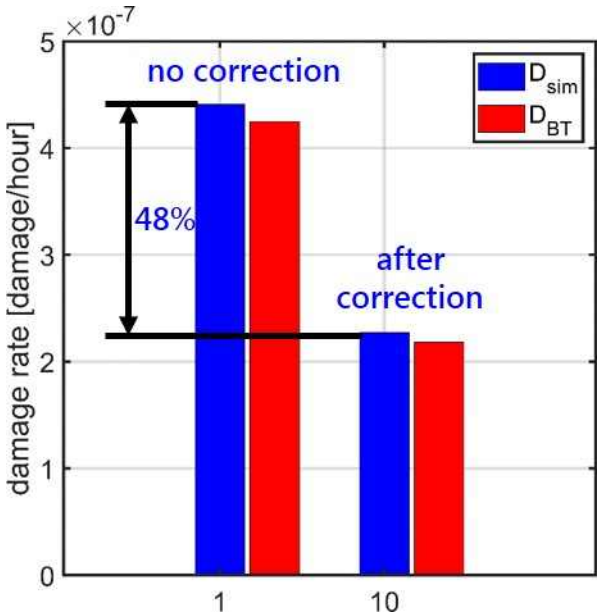

Fig. 42 Comparison fatigue damages estimated by time and frequency domain methods without and with mean stress correction. [Type 4 −

$(\alpha_1, \alpha_2) = (0.6, 0.1))$

Although, global mean stress is assumed to be zero, the mean stress correction through the reduction factor has significant reduction on estimated fatigue damages. The estimated fatigue damage by the BT model expressed as red bin gives very accurate results before and after mean stress correction.

The fatigue analysis considering the mean stress correction is performed in the same spectra. Two additional conditions that global mean value is negative (compression) and positive (tension) states as described in Fig. 43. Three groups of simulated data whose global mean values are shifted to $-0.5\sigma_X, 0$ and $0.5\sigma_X$ are considered in this example.

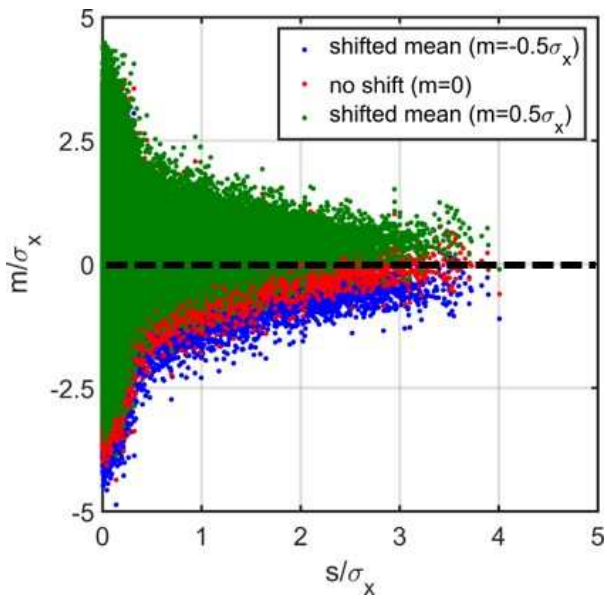

Fig. 43 Three groups of simulated data with shifted global mean value

(m=−0.5σ_X [blue], m=0 [red], m=0.5σ_X [green])

Finally, the estimated fatigue damages considering with and without mean stress correction through the BT and the proposed models are summarized in Fig. 44. The effect of the shifted mean values seem to be small in this example. Although, the proposed model gives better results than the BT model, these two model seem to give very accurate results in Gaussian processes.

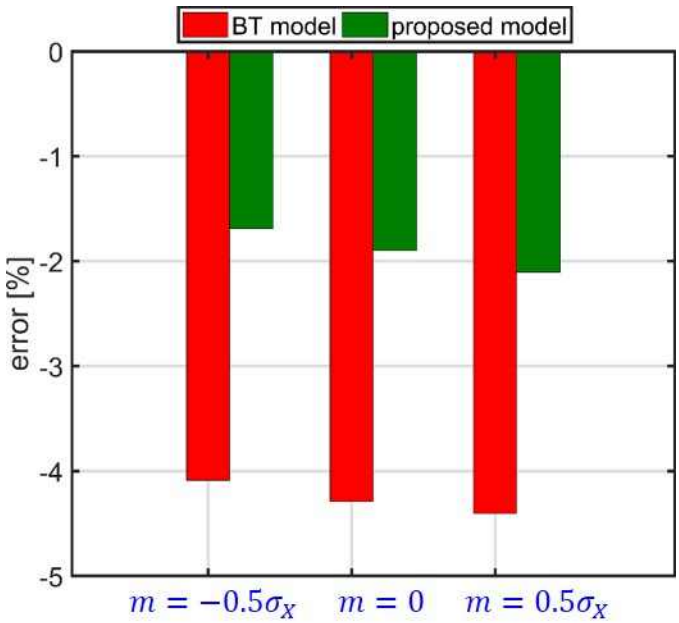

Fig. 44 The errors of two approximate models [BT model (red) and proposed model (green)] in three groups with different shifted mean values

Chapter 5. Fatigue analysis for wide-banded non-Gaussian random loadings

5.1. Introduction

In chapter 3, 4, all probabilistic models are derived under the wide-banded Gaussian assumption. However, most loadings and corresponding structural responses are not Gaussian process but non-Gaussian processes. The 3rd and 4th statistical moments of random process X(t) called skewness and kurtosis respectively are the parameters which indicate non-normality of X(t). When X(t) is Gaussian process, skewness and kurtosis of X(t) are 0 and 3 respectively. When skewness and kurtosis are deviated from this, the random process is called non-Gaussian process.

Some literatures have tried to explain the non-normal behavior of random processes and consider the effect of non-normality on fatigue damages. One solution for dealing with this non-normality is transformed Gaussian processes. This approach utilizes transformation function which relates non-Gaussian random process Z(t) and underlying Gaussian process X(t) which has the same mean and standard deviations of Z(t). After non-Gaussian process Z(t) is transformed to corresponding Gaussian process X(t), developed probabilistic models derived under Gaussian assumption can be applied to estimate joint probability distribution of mean and amplitude or marginal distribution of amplitude for evaluating fatigue

damage rate. Some literatures proposed their own transformation models to describe non-normal behavior of random process Z(t) [Winterstein (1988), Sarkani et al (1994), Winterstein et al (1994), Ochi and Ahn (1994)]. However, their models were limited in narrow-band problems and some of them only utilized skewness or kurtosis only so it can be used in limited non-Gaussian conditions. Rychlik et al (1997) suggested non-linear transformation function to overcome these limitations but the transformation function was not derived explicitly so it should depend on numerical approach.

Benasciutti & Tovo (2005, 2006) derived their own approximate joint probability distribution of mean and amplitude in Gaussian process X(t). They tried to extend their joint probability distribution model to non-Gaussian problems using transformation techniques.

Another approach to handle the effect of non-normality on fatigue damages is introducing correction factor. Winterstein (1988) suggested transformed Gaussian process through the Hermite function and he derived the ratio of fatigue damages under the non-normal process Z(t) to that of the underlying normal process X(t). However, as mentioned above, it was limited only for narrow-band problems. Wang and Sun (2005) modified the correction factor proposed by Winterstein by reflecting mean stress correction but they failed to derive explicit form of correction factor in wide-band non-Gaussian process. Braccesi et al (2009) proposed elaborate correction factor considering skewness and kurtosis of random process from a large amount of simulations. Cianetti et al (2018) explained that the correction factor proposed by Braccesi et al tends

to overestimate fatigue damages in high kurtosis region and suggested a correction factor suitable for high kurtosis. However, it also had a limitation that it assumed zero skewness condition.

Other approaches for describing non-normal behavior of random processes also have been investigated. Aberg et al (2009) introduced the Laplace driven moving average technique to overcome the dependence on Gaussian process in handling non-Gaussian process. Wolfsteiner (2017) showed interesting point of view in non-stationary and non-Gaussian processes. He tried to decompose non-stationary and non-Gaussian signal into several stationary portions with Gaussian processes. By comparing fatigue damages from initial non-Gaussian signal and the derived Gaussian portion, he verified the efficiency and the accuracy of his method.

In this chapter, it is explained how the derived joint probability distribution of stress mean and amplitude in Gaussian process is extended to non-Gaussian process through transformation techniques. Some literatures for transformation techniques are introduced in chapter 5.2. Among them, the Hermite function is used in this present work so the detail of the Hermite function is explained in chapter 5.3. Because there are some limitations of transformation through the Hermite functions, the limitations and some modifications on the Hermite functions are also addressed in chapter 5.3. Numerical simulations for verifying the accuracy of the proposed model in fatigue assessment for non-Gaussian random loadings are performed in idealized five stress spectra. The detail procedure and results of numerical simulations are explained in chapter 5.4.

5.2. Transformation techniques

Non-normality of non-Gaussian random process Z(t) is indicated by the standardized 3rd and 4th statistical moments of Z(t). The mathematical expression of these moments are defied as shown in Eq. (5.1).

$$\gamma_3 = \frac{E[(Z-\mu_Z)^3]}{\sigma_Z^3} \quad , \quad \gamma_4 = \frac{E[(Z-\mu_Z)^4]}{\sigma_Z^3} \qquad (5.2)$$

where, γ_3: skewness, γ_4: kurtosis

The 3rd moment called skewness is related to the degree of asymmetry of non-Gaussian process Z(t). When the skewness of Z(t) is zero, the probability density function of Z(t) is symmetry around its mean value μ_Z. On the other hands, the skewness is deviated from zero, the distribution of Z(t) is no longer symmetric as shown in Fig. 45.

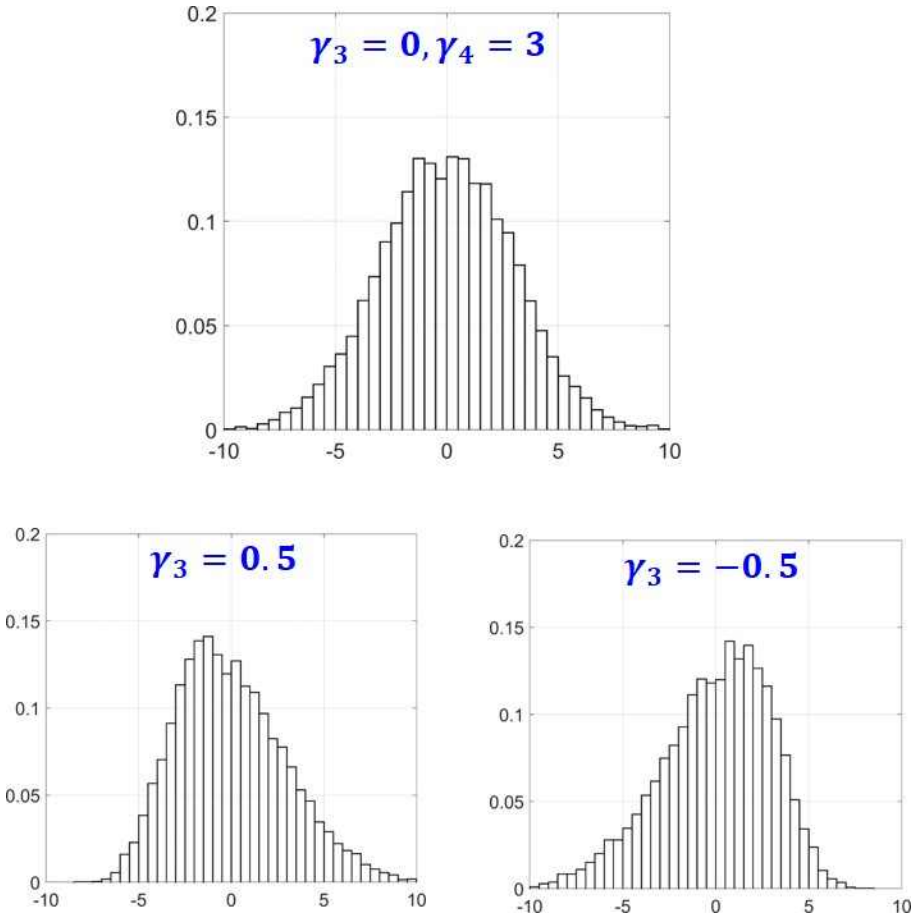

Fig. 45 An example of histograms of Gaussian process and skewed non-Gaussian process

The kurtosis indicates the heaviness of probability densities at tails. When it is larger than 3 (softening non-Gaussian process), the tail probability density is greater than Gaussian distribution tails whereas the converse (hardening non-Gaussian process) holds for a density having less probability mass in the tails as described in Fig. 46. In Gaussian random process X(t), both skewness and kurtosis of X(t) are 0 and 3 respectively.

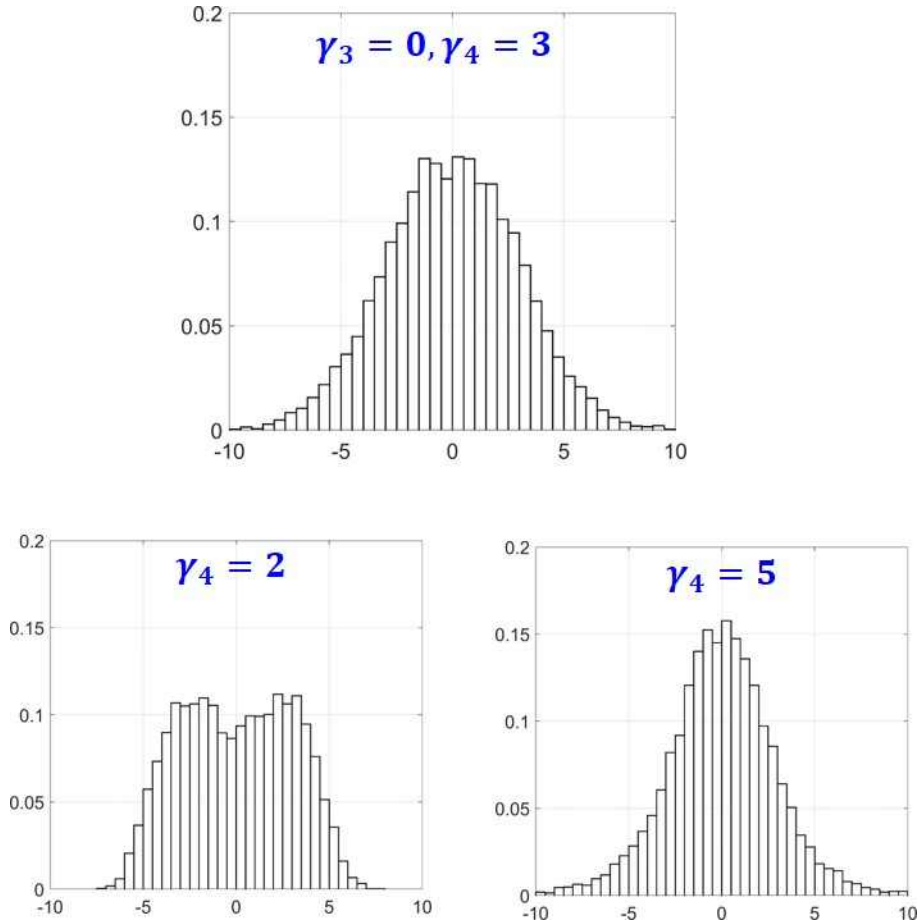

Fig. 46 An example of histograms of Gaussian process and hardening (left) and softening (right) non−Gaussian process

Transformation function is a nonlinear function which explains the relationship between non−Gaussian random process Z(t) and the underlying Gaussian random process X(t) as expressed in Eq. (5.2).

$$Z(t) = G[X(t)] \quad \leftrightarrow \mathrm{X(t)} = G^{-1}[Z(t)] = \mathrm{g}[Z(t)] \qquad (5.2)$$

where, $\mathrm{G}[\cdot]$: Transfomration function

The underlying Gaussian process X(t) has the same mean and

variance of the non-Gaussian random process Z(t). Fig. 47 shows an example of Z(t) and corresponding X(t).

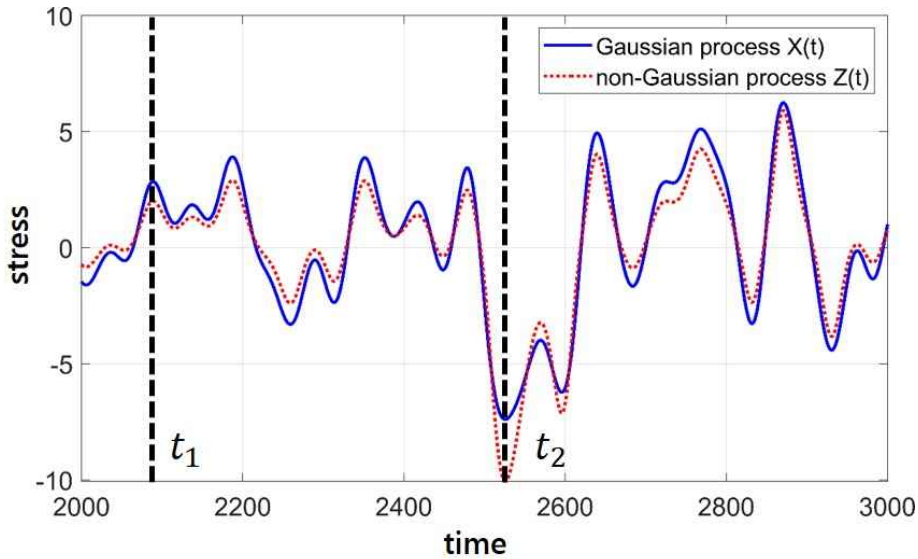

Fig. 47 An example of non-Gaussian random process Z(t) and the underlying Gaussian random process X(t)

Several transformation functions have been suggested and coefficients in these transformation functions were defined as a function of skewness and kurtosis. The important feature of transformation function is that it should be a monotonically increasing function to make Z(t) and X(t) have peaks and valleys at the same time. For example, Z(t) has peaks at t_1 as shown in Fig. 45. If transformation function G is monotonically increasing function, corresponding peak is also observed in X(t) at t_1. Z(t) and X(t) have valley at t_2 in the same manner. Under the assumption, X(t) and Z(t) always have peaks and valleys at the same time so rainflow counted

cycles in X(t) and transformed Z(t) will be counted at the same instants of time. In other words, the transformation function does not change the number and the sequence of rainflow-counted cycles and only control the amplitude or mean value of cycles.

5.2.1. Hermite model [Winterstein (1988)]

Grigoriu (1984) proposed to use a translation function to transform a Gaussian process to non-Gaussian process using cumulative distribution functions as shown in Eq. (5.3).

$$Z(t) = g[X(t)] = (F^{-1} \cdot \Phi)(X(t)) \tag{5.3}$$

where, F: cumulative distribution function of Z(t)

Φ: standard normal cumulative distribution function

As a translation function ($(F^{-1} \cdot \Phi)$), he compared several distribution functions such as log-normal, shifted log-normal, shifted exponential, Weibull and Gamma functions to describe various non-Gaussian random processes.

Winterstein (1988) utilized the Hermite polynomials as a translation function to describe general non-normal behavior of non-Gaussian process Z(t). Definition of the Hermite polynomials is suggested in Eq. (5.4).

$$H_n(x) = (-1)^n e^{x^2} \frac{d^n}{dx^n}\left(e^{-x^2}\right) \tag{5.4}$$

He explained that the third order Hermite polynomials is sufficient as a translation function for describing general non-Gaussian process Z(t). In this model, non-Gaussian processes are distinguished for the case of a softening and hardening processes and different translation functions and coefficients are used to explain non-normal behavior.

When kurtosis of Z(t) is larger than three, Z(t) is called a softening non-Gaussian process. In this case, the Winterstein's model is given in Eq. (5.5).

$$\frac{Z(t)-\mu_Z}{\sigma_Z} = Z_0(t) = \mathrm{G}[X_0(t)] = \kappa\left[X_0 + \sum_{n=3}^{4} \tilde{h}_n H_{n-1}(X_0)\right]$$
$$= \kappa\left[X_0 + \tilde{h}_3(X_0^2 - 1) + \tilde{h}_4(X_0^3 - 3X_0)\right] \tag{5.5}$$

where, $X_0 = \frac{X(t)-\mu_X}{\sigma_X}$, $\tilde{h}_3 = \frac{\sqrt{1+1.5(\gamma_4-3)}-1}{18}$, $\tilde{h}_4 = \frac{\gamma_3}{4+2\sqrt{1+1.5(\gamma_4-3)}}$,

$$\kappa = \frac{1}{\sqrt{1+2\tilde{h}_3^2+6\tilde{h}_4^2}}$$

Winterstein et al (1994) gave modified expression for coefficients of the Hermite function in Eq. (5.6).

$$\tilde{h}_3 = \frac{\gamma_3}{6}\left[\frac{1-0.15|\gamma_3|+0.3\gamma_3^2}{1+0.2(\gamma_4-3)}\right], \tilde{h}_4 = \tilde{h}_{40}\left[1-\frac{1.43\gamma_3^2}{\gamma_4-3}\right]^{1-0.1\gamma_4^{0.8}}$$
$$\tilde{h}_{40} = \frac{[1+1.25(\gamma_4-3)]^{1/3}-1}{10} \tag{5.6}$$

The inverse function of translation function G^{-1} can be obtained by inverting X(t) and Z(t) as shown in Eq. (5.7).

$$X_0(t) = \left[\sqrt{\xi^2(Z)+c}+\xi(Z)\right]^{1/3} - \left[\sqrt{\xi^2(Z)+c}-\xi(Z)\right]^{\frac{1}{3}} - a \qquad (5.7)$$

where $\xi(Z) = 1.5b\left(a+\frac{Z-\mu_Z}{\kappa\sigma_Z}\right) - a^3,\ a = \frac{\tilde{h}_3}{3\tilde{h}_4},\ b = \frac{1}{3\tilde{h}_4},$

$c = (b-1-a^2)^3$

On the other hands, Z(t) is called a hardening process whose kurotsis is smaller than three and the inverse function of translation function at that time is expressed as Eq. (5.8).

$$X_0(t) = Z_0 - \sum_{n=3}^{4} \tilde{h}_n H_{n-1}(Z_0) = Z_0 - h_3(Z_0^2-1) - h_4(Z_0^3-3Z_0) \qquad (5.8)$$

where, $h_3 = \frac{\gamma_3}{6},\ h_4 = \frac{\gamma_4-3}{24}$

As mentioned in chapter 5.1, all transformation function should be a monotonically increasing function. This means that the 1st derivative of transformation function is always positive. Due to this condition, the Hermite function can be used in limited skewness and kurtosis region expressed in Eq. (5.9) & Eq. (5.10). An example of the applicable regions for the Hermite function is described in Fig. 48.

$$\tilde{h}_3^2 - 3\tilde{h}_4\left(1-3\tilde{h}_4\right) \le 0 \rightarrow 3 + (1.25\gamma_3)^2 \le \gamma_4 \ \text{(hardening process)} \qquad (5.9)$$

$$\gamma_3^2 < \frac{2(\gamma_4 - 3)}{3} \quad \text{(softeing process)} \tag{5.10}$$

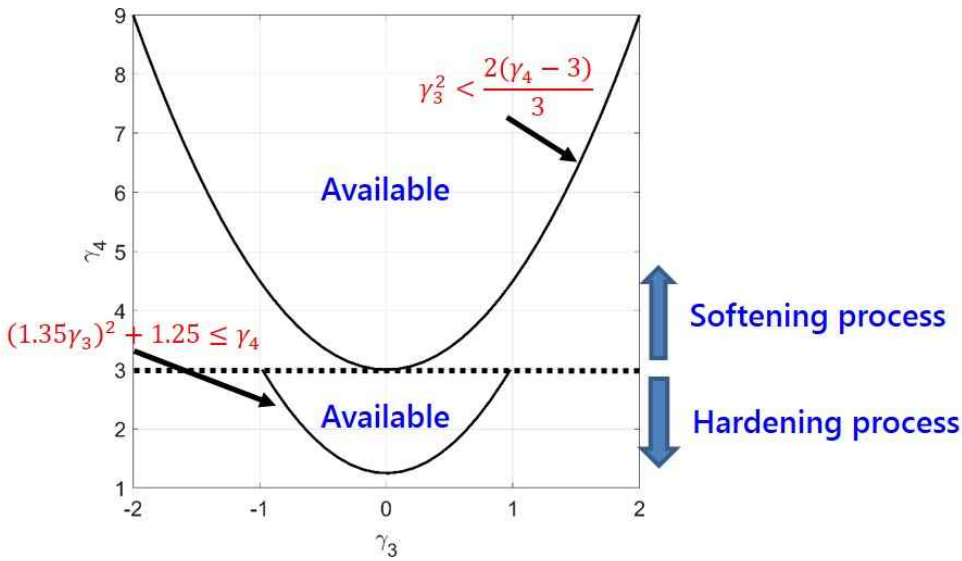

Fig. 48 Applicable regions for the Hermite function

5.2.2. Power-law model [Sarkani et al (1994)]

Sarkani et al (1994) proposed another transformation function as a function of kurtosis only. They defined the transformation function as shown in Eq. (5.11).

$$Z(t) = G[X(t)] = \frac{X(t) + \beta\big(\mathrm{sgn}(X)\big)(|X|^n)}{C} \tag{5.11}$$

where, $\mathrm{sgn}(\cdot)$: the signum function $[\mathrm{sgn}(X) = 1 \text{ for } x > 0,\ 0 \text{ for } x = 0 \text{ and } -1 \text{ for } x < 0]$,

β, n: parameters used to control non−normality

$$C = \sqrt{1 + \frac{2^{1/2(n+1)} n\Gamma(n/2)\sigma_X^{n-1}}{\sqrt{\pi}}\beta + \frac{2^n\Gamma(n+1/2)\sigma_X^{2(n-1)}}{\sqrt{\pi}}\beta^2}$$

Two parameters β, n should be positive to make the transformation function monotonically increasing function. By substituting Eq. (5.11) into the definition of kurtosis, Eq. (5.12) can be derived.

$$\gamma_{4,Z} = \frac{E[(Z-\mu_Z)^4]}{\sigma_Z^2} = \frac{E\left[\left(X(t)+\beta\left(\mathrm{sgn}(X)\right)(|X|^n)\right)^4\right]}{C^4\sigma_X^4}$$
$$= \frac{1}{C^4\sigma_X^4}\begin{bmatrix} E(X^4)+4\beta E(|X|^{n+3})+6\beta^2 E(X^{2n-2}) \\ +4\beta^3 E(|X|^{3n+1})+\beta^4 E(X^{4n}) \end{bmatrix} \tag{5.12}$$

Under given kurtosis value of non-Gaussian random process Z(t), a unique transformation function can be obtained by specifying either the intensity of non-normality n or the coefficient of the non-linear portion β. Thus, various combinations of β, n which indicate the same kurtosis value exist.

5.3. Fatigue analysis for wide-banded non-Gaussian processes

5.3.1. Modified Hermite transformation

In this present work, the Hermite function is used to transform non-Gaussian random process Z(t) to Gaussian random process X(t). Some literatures have commented that the accuracy of the coefficients of Hermite function proposed by Winterstein are only

ensuresed for representing very mildly non-Gaussian processes, especially hardening processes. Also, the original Hermite function is not held for skewed hardening non-Gaussian processes. The accuracy of the Hermite function using the coefficients proposed by Winterstein is investigated in this work before non-Gaussian simulations. In chapter 4, a large amount of wide-banded Gaussian random processes are generated from the idealized five different stress spectra. Non-Gaussian random processes Z(t) are generated through the Hermite function. Total 73 number of combinations of target skewness and kurtosis are determined considering the applicable region of the Hermite function shown in Eq. (5.9) & (5.10). The range of target skewness are −0.8 to 0.8 at interval of 0.2. In case of target kurtosis, it ranges from 1.5 to 9 within the applicable region. We compare the target values of skewness and kurtosis with the skewness and kurtosis of simulated non-Gaussian random process Z(t) calculated through the original Hertmie function. The results are shown in Fig. 49. As mentioned above, the Hermite function utilizing the coefficients proposed by Winterstein seems to be not proper for hardening processes and give large deviations compared to simulated skewness and kurtosis in high kurtosis regions.

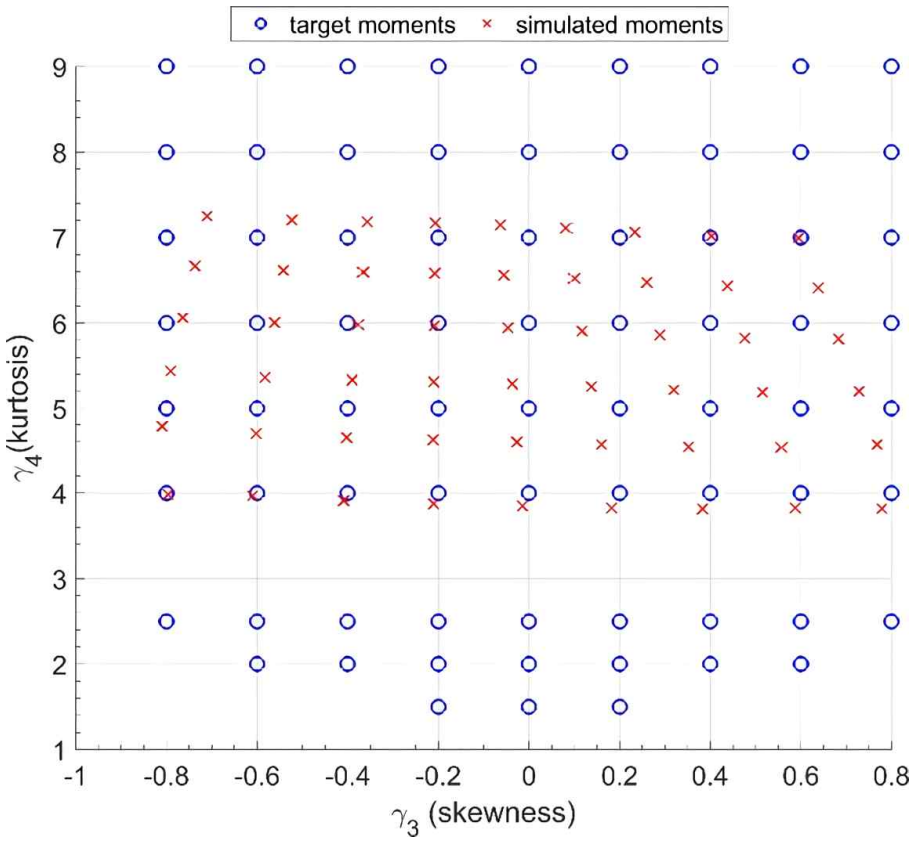

Fig. 49 Comparison between target and simulated the 3rd and 4th moments through conventional Hermite transformation

Ding and Chen (2015) suggested closed-form formulations for determining the model coefficients in terms of skewness and kurtosis for hardening non-Gaussian processes. They approximated the form of the Hermite function and its inverse function for hardening non-Gaussian processes as shown in Eq. (5.13) and Eq. (5.14).

$$Z(t) = G[X(t)] = \left[\sqrt{\xi^2(X) + c} + \xi(X)\right]^{1/3} - \left[\sqrt{\xi^2(X) + c} - \xi(X)\right]^{\frac{1}{3}} - a \quad (5.13)$$

where, $\xi(X) = \frac{X}{2b_4} + \frac{\gamma_3}{2} + \mathrm{a}(1.5 + 1.5b - a^2)$, $a = \frac{b_3}{3b_4}$

$$b = \frac{b_2 - b_3\gamma_3 - b_4\gamma_4}{3b_4}, c = (b - a^2)^3$$

$$b_2 = \varphi\left[1 - \frac{\gamma_3^4 + 1.2\gamma_3^2 - 0.18}{7.5exp\ (0.5\gamma_4)}\right], b_3 = -\frac{0.8\gamma_3^5 + \gamma_3^3 + 0.77\gamma_3}{(\gamma_4 - 1)^2 + 0.5}$$

$$b_4 = -\varphi\left[0.04 - \frac{11.5\gamma_3^4 + 6.8\gamma_3^2 + 3.5}{(\gamma_4^2 + 0.4)^2 + 0.15}\right], \varphi = [1 - 0.06(3 - \gamma_4)]^{1/3}$$

$$X(t) = G^{-1}[Z(t)] \cong b_2 Z + b_3(Z^2 - \gamma_3 Z - 1) + b_4(Z^3 - \gamma_4 Z - \gamma_3) \quad (5.14)$$

Gurley (1997) summarized the existing non-Gaussian simulation techniques using the transformation function. He also developed forward and backward modified Hermite transformations. These algorithms enhanced the accuracy of the Winterstein' s Hermite transformation. The backward transformation is related to the transformation between non-Gaussian random process Z(t) to Gaussian process X(t) and the forward transformation is the converse transformation of backward as described in Fig. 50.

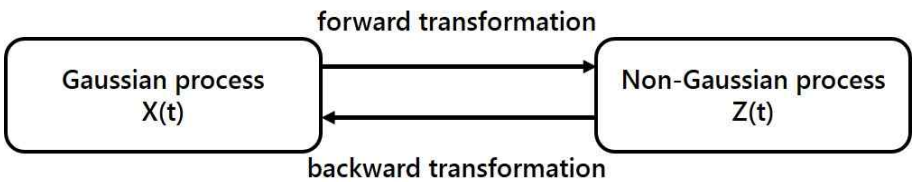

Fig. 50 Forward and backward transformations

The coefficients in modified Hermite transformation is identified using optimization routine. From the probability density function derived by Grigoriu (1984) suggested in Eq. (5.15), the skewness

and kurtosis of estimated non−Gaussian random process Z(t) can be calculated as shown in Eq. (5.16).

$$p_Z(z) = \frac{1}{\sqrt{2\pi}} \exp\left[-\frac{X^2(Z)}{2}\right] \frac{dX(Z)}{dZ} \tag{5.15}$$

where, $X(\mathrm{t})$: standard normal random variables

$Z(\mathrm{t})$: transformed non−Gaussian variables through Hermite transformation as described in Eq. (5.6) and (5.8)

$$\gamma_{3,\mathrm{est}} = \frac{\int (y-\mu_Z)^3 p_z(z)dz}{\sigma_Z^3}, \qquad \gamma_{4,\mathrm{est}} = \frac{\int (y-\mu_Z)^4 p_z(z)dz}{\sigma_Z^4} \tag{5.16}$$

where $\gamma_{3,est}$, $\gamma_{4,est}$: estimated skewness and kurtosis values

The coefficients of the modified Hermite transformation derived by Gurley (1997) was defined as the values minimizing the error function as shown in Eq. (5.17).

$$\mathrm{err}(h_3, h_4) = \left(\bar{\gamma}_3 - \gamma_{3,\mathrm{est}}(h_3, h_4)\right)^2 + \left(\bar{\gamma}_4 - \gamma_{4,\mathrm{est}}(h_3, h_4)\right)^2 \tag{5.17}$$

where, $\bar{\gamma}_3, \bar{\gamma}_4$: target skewness and kurtosis values

The forward and backward transformations are called moment correction part that means procedure for finding appropriate coefficients that make target and estimated the 3rd and 4th moments equal. However, the power spectral density of simulated non−Gaussian processes could be changed during the moment correction procedure so spectral parameters such as bandwidth parameters and

mean up-crossing rate are different to original values. To prevent this, Gurley (1997) developed new simulation techniques called spectral correction by controlling the amplitude of Fourier coefficients.

We compare the target values of skewness and kurtosis with the skewness and kurtosis of simulated non-Gaussian random process Z(t) calculated through the modified Hertmie function once again. The results are shown in Fig. 51. The modified Hermite transformation proposed by Ding and Xinzhong for hardening non-Gaussian processes seems to give small deviations between target and simulated moments only using skewness and kurtosis values. The simulated moments obtained by Gurley' s simulation technique based on optimization routines also show a good agreement on target value. Thus, in this present work, non-Gaussian random processes

are generated by the modified Heremite transformation.

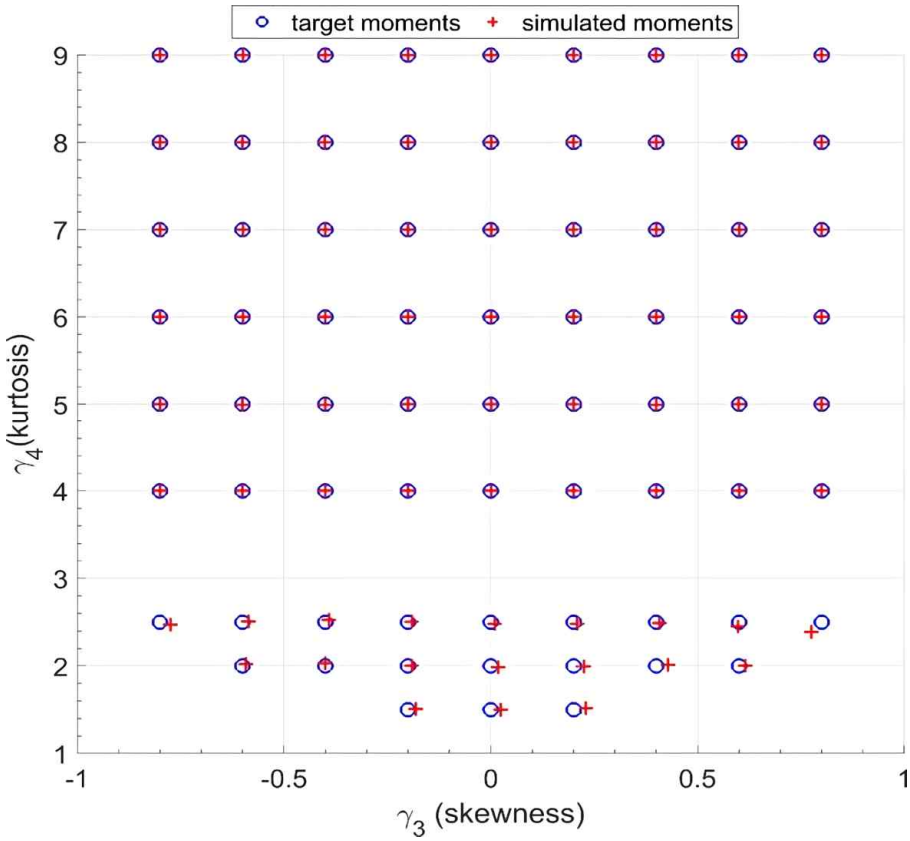

Fig. 51 Comparison between target and simulated the 3rd and 4th moments through modified Hermite transformation

5.3.2. Numerical simulations for non-Gaussian signals

In chapter 4.2, the procedure for generating a large amount of data blocks containing wide-banded Gaussian random processes X(t) in the idealized different five stress spectra is introduced. Non-Gaussian random processes Z(t) are generated to verify the accuracy of the proposed probabilistic model in evaluating fatigue damages

induced by wide-banded non-Gaussian random loadings through the modified Hermite transformation function. The detail procedure for generating non-Gaussian signal is summarized in Fig. 52.

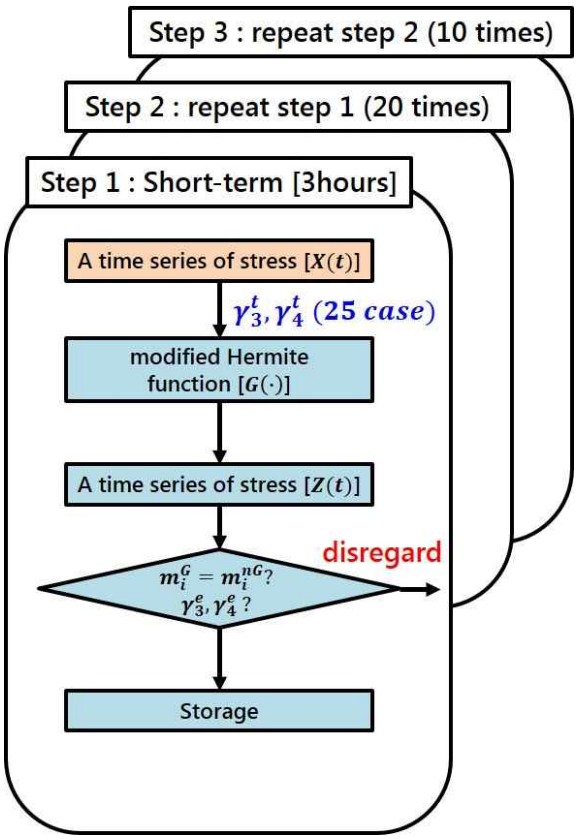

Fig. 52 Procedure for generating non-Gaussian random process Z(t)

In this works, total 25 number of experimental points that represent different combinations of target skewness and kurtosis are considered. The target skewness ranges from −0.5 to 0.5 at interval of 0.5. In case of target kurtosis, they are determined within 1.5 to 9 with consideration for the applicable region of Hermite transformation. The detailed information of the non-normality

condition is summarized in Table 2 and Fig. 53.

Table 2 Non−normality conditions

Target skewness ($\bar{\gamma}_3$)	Target kurtosis ($\bar{\gamma}_4$)
−0.5	2,2.5,4,5,6,7,8,9
0	1.5,2,2.5,4,5,6,7,8,9
0.5	2,2.5,4,5,6,7,8,9

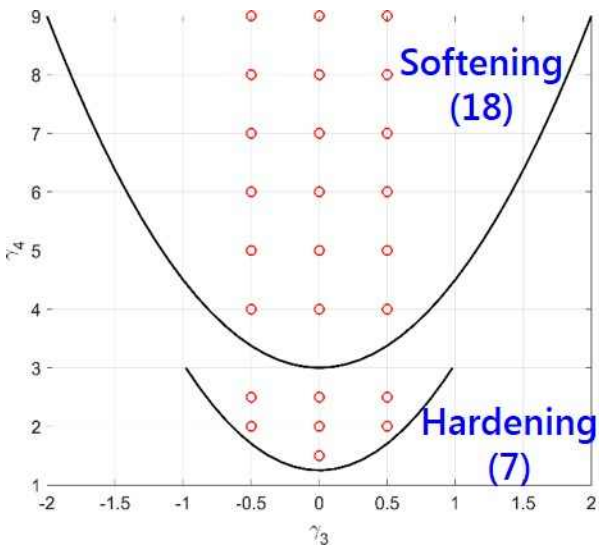

Fig. 53 The experimental points with applicable region for Hermite transformation

5.3.3. Results

Fatigue damages in all stress spectra used in chapter 4 are estimated by two frequency domain methods: BT and the proposed models. Let us assume that two stress cycles are observed in

Gaussian process X(t). These cycles share the same amplitude but have different mean values. At first, let assume that these cycles are transformed to hardening non-Gaussian process Z(t) through the modified Hermite transformation. For hardening process, which has wider tail probability than Gaussian process, the gradient of the Hermite transformation function tend to decrease as the farther away from the origin. Therefore, as described in Fig. 54, these two stress cycles have the same amplitude before transformation, the amplitude of cycle A, which is a zero-mean cycle, is larger than that of cycle B after the Hermite transformation for hardening process. In short, corresponding fatigue damages induced by two stress cycles are different after the transformation and zero-mean cycle A induces larger damage than cycle B in case of hardening non-Gaussian process.

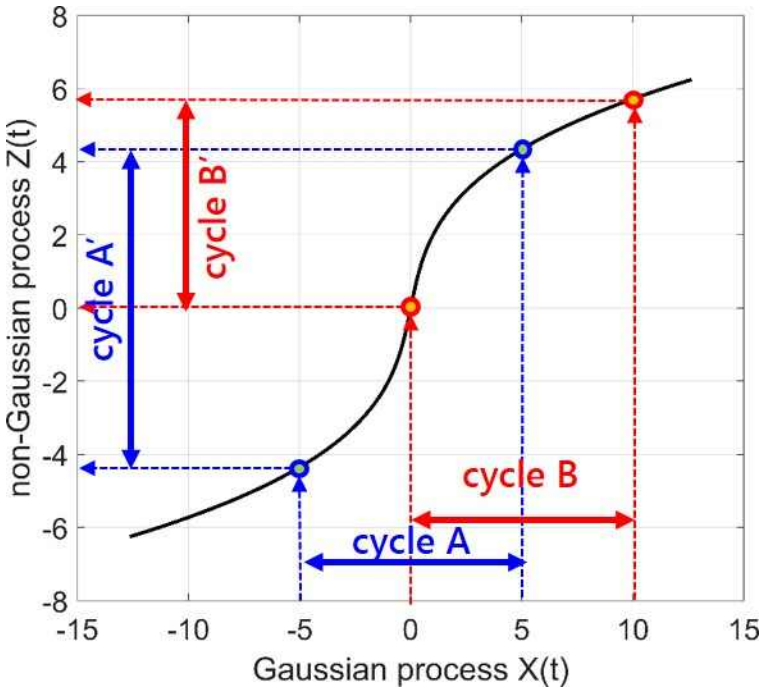

Fig. 54 Comparison of two rainflow-counted cycles before and after the Hermite transformation for hardening process

Conversely, the gradient of the Hermite transformation function increases as the farther away from the origin for softening non-Gaussian process. Thus, the amplitude of zero-mean cycle A is smaller than that of cycle B as shown in Fig. 55.

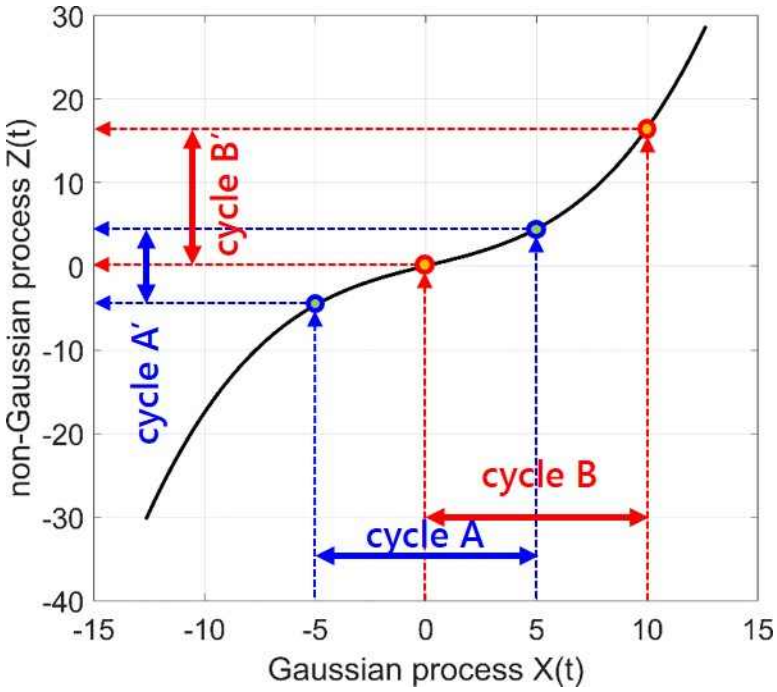

Fig. 55 Comparison of two rainflow-counted cycles before and after the Hermite transformation for softening process

As explained in chapter 4, the BT model tends to overestimate the probability density of zero-mean stress cycles due to the symmetric assumption in level-crossing counting cycle distribution. Therefore, it is expected that the BT model tends to overestimate fatigue damages in hardening processes and underestimate damages for softening non-Gaussian processes. To verify the accuracy of two frequency domain methods for estimating fatigue damages induced by non-Gaussian random loadings, the estimated fatigue damages by two models are compared to the results of the time domain approach with RFC in all stress spectra. As explained in Eq. (3.23), marginal distribution of stress amplitude could be obtained by integrating joint probability distribution of mean and amplitude against mean. Fig. 56

- 57 show examples of marginal distribution of amplitude in case of hardening and softening non−Gaussian processes. The y−axis indicates exceedance probability of stress amplitude in log scale and the x−axis is normalized stress amplitude. As mentioned above, the BT model tends to overestimate exceedance probability of stress cycles in high amplitude region for hardening non−Gaussian process. On the other hands, for softening non−Gaussian process shown in Fig. 57, the BT model underestimates the exceedance probability in high amplitude region.

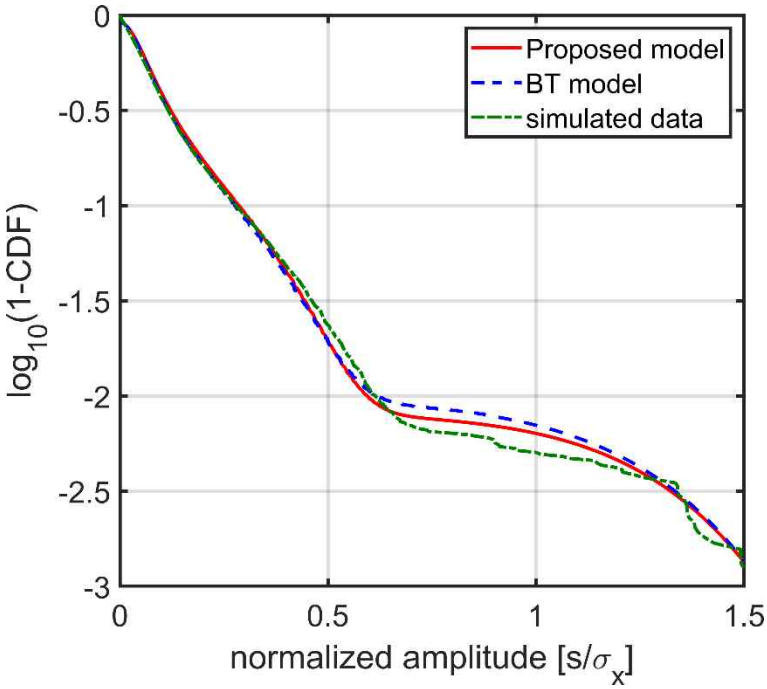

Fig. 56 An example of exceedance probability of amplitude estimated by two approximate models and simulated data in log scale versus normalized stress amplitude [$(\gamma_3, \gamma_4)=(0,1.5)$, $(\alpha_1, \alpha_2)=(0.17,0.1)$] [Type 1]

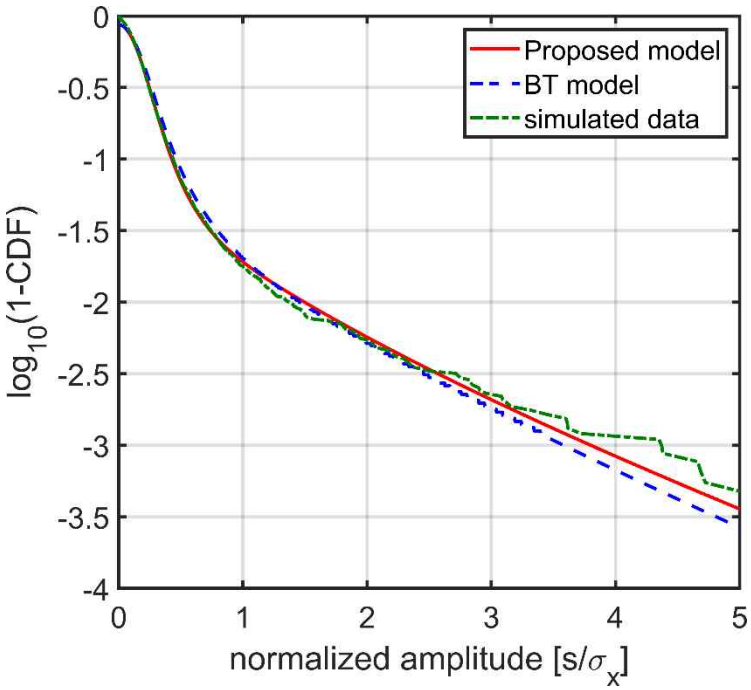

Fig. 57 An example of exceedance probability of amplitude estimated by two approximate models and simulated data in log scale versus normalized stress amplitude [(γ_3, γ_4) = (0, 9), (α_1, α_2) = (0.17, 0.1)] [Type 1]

Fig. 58 - 60 shows the errors between estimated fatigue damages calculated by time and frequency domain methods. The error is defined as shown in Eq. (5.18).

$$\text{error} = \frac{\left(\bar{D}^{\text{est}} - \bar{D}^{\text{RFC}}\right)}{\bar{D}^{\text{RFC}}} \times 100 \ \ [\%] \tag{5.18}$$

where $\bar{D}^{\text{est}}$: estimated fatigue damage rate by frequency domain method

$\bar{D}^{\text{RFC}}$: rainflow−counted fatigue damage rate

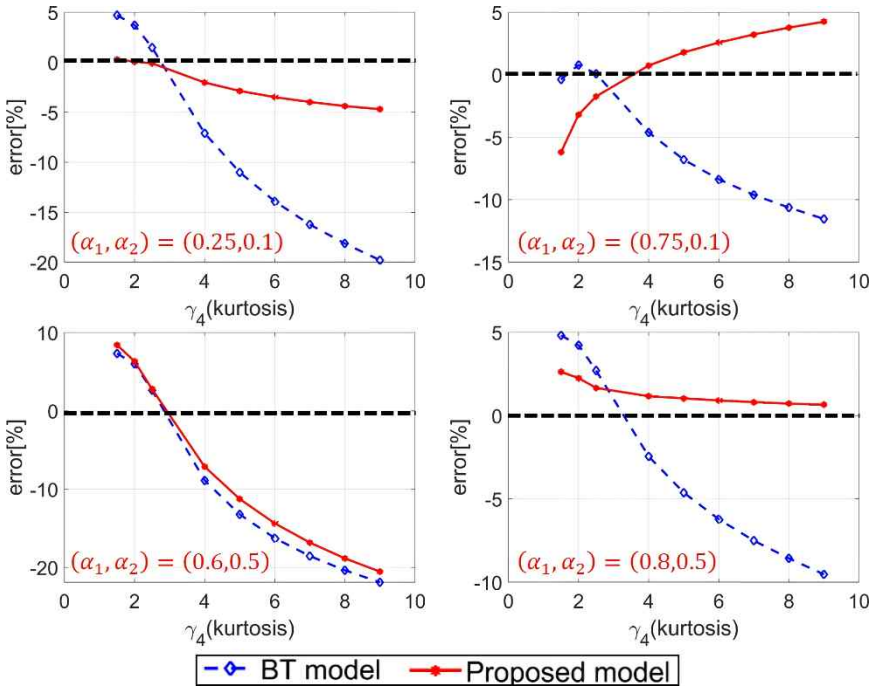

Fig. 58 The errors of fatigue damages estimated by two approximate models in the 4th type of stress spectra (γ_3=-0.5)

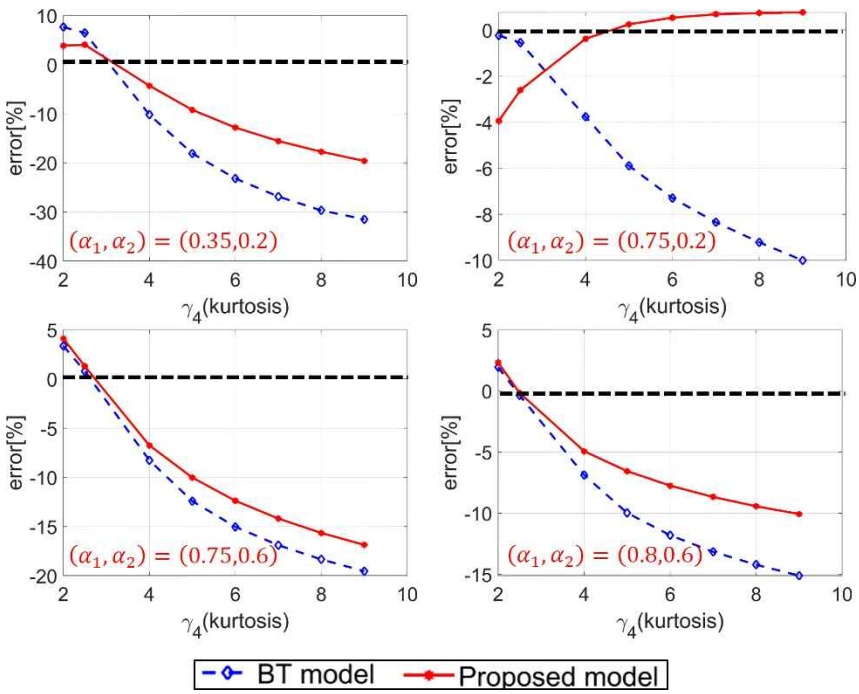

Fig. 59 The errors of fatigue damages estimated by two approximate

models in the 3rd type of stress spectra (γ_3=0)

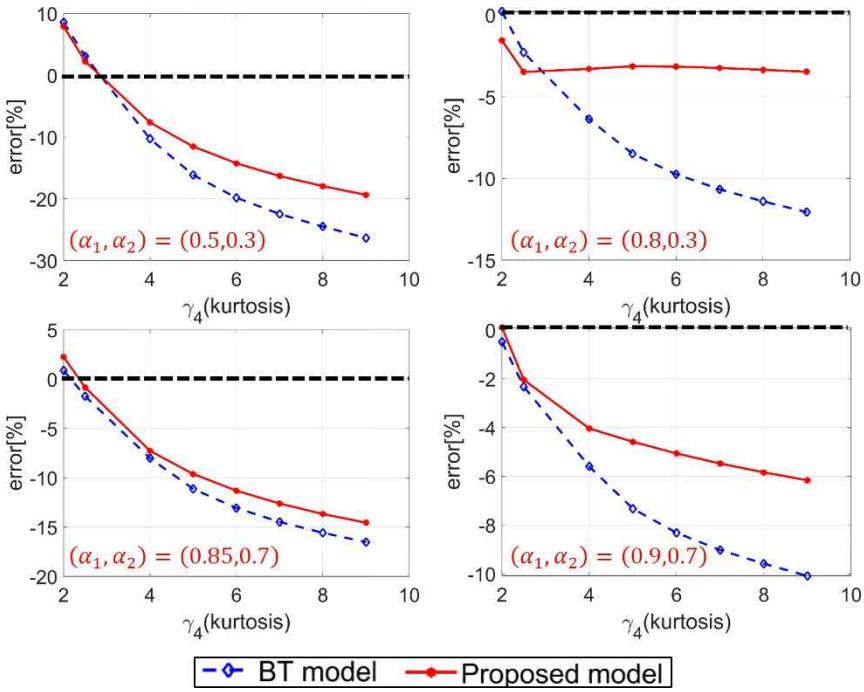

Fig. 60 The errors of fatigue damages estimated by two approximate models in the 5th type of stress spectra (γ_3=0.5)

As we expect, the BT model tends to overestimate fatigue damages when kurtosis of non-Gaussian random process Z(t) is smaller than 3. As kurtosis increases, the BT model underestimates fatigue damages in all stress spectra. On the other hands, the proposed model, which consists of the marginal distribution of stress amplitude proposed by BT and the conditional probability density function of stress mean given amplitude proposed by this work, seems to give better results in assessment on fatigue damages in wide-banded non-Gaussian problems.

Benasciutti and Tovo (2005) suggested error index (EI) as

defined in Eq. (5.19) to compare the accuracy of frequency domain models for wide-banded Gaussian processes. We also calculates and compares the error index of two approximate models in all stress spectra and non-Gaussian conditions in Table 3.

$$\mathrm{EI} = \sqrt{\frac{1}{n}\sum_{i=1}^{n}\left[\log_{10}\left(\frac{\overline{D}^{\mathrm{est}}}{\overline{D}^{\mathrm{RFC}}}\right)\right]^2} \tag{5.18}$$

Table 3 Error index of two approximate models

Spectrum type	$\mathrm{EI}_{\mathrm{BT}}$	$\mathrm{EI}_{\mathrm{prop}}$	$\frac{\mathrm{EI}_{\mathrm{prop}}}{\mathrm{EI}_{\mathrm{BT}}} \times 100$ [%]
Type 1	0.641	0.503	78.5%
Type 2	1.260	0.894	71.0%
Type 3	0.477	0.315	66.0%
Type 4	0.465	0.260	56.0%
Type 5	0.476	0.323	67.9%

The proposed model only modifies the information of stress mean in probabilistic models. By only adjusting the information of mean in joint probability distribution, the accuracy of fatigue damages increases significantly.

5.3.4. Discussion

To derive approximate joint probability distribution of mean and amplitude in wide-banded Gaussian processes, the approximate

model for marginal distribution of stress amplitude proposed by Benasciutti and Tovo (2005) is used. Although, the BT model is one of the most accurate model evaluating fatigue damage for wide-banded Gaussian random loadings, some literature argued that this model tends to give a poor prediction in estimation of the shape of probability density function of stress amplitude. Some examples of the estimated shapes of probability density functions of stress amplitude and corresponding fatigue damages are given in Fig. 61.

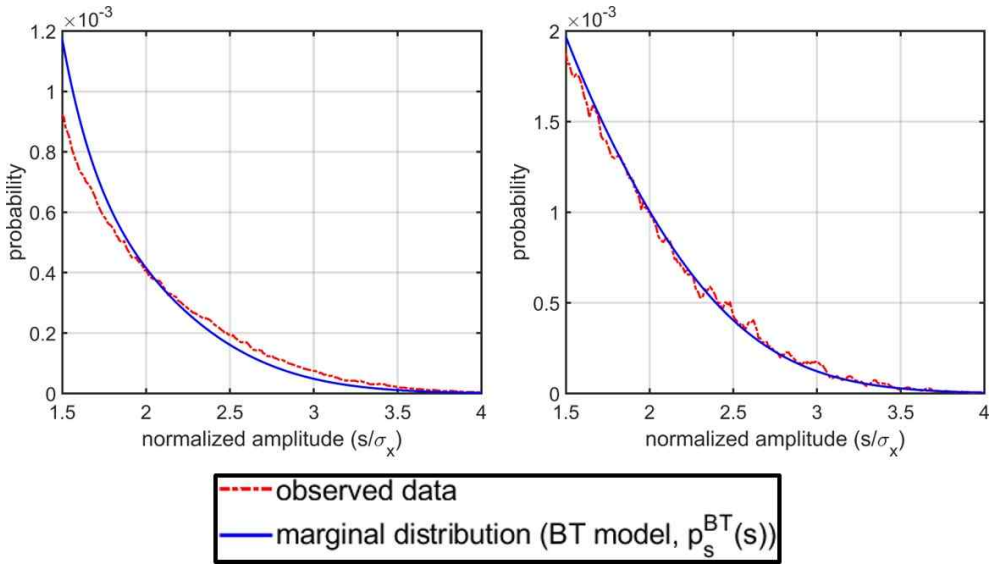

Fig. 61 Comparison between estimated (blue) and actual (red) shapes of probability of stress amplitudes in two stress spectra [(α_1, α_2) = (0.6, 0.5) [left]; (α_1, α_2) = (0.8, 0.5) [right]] [Type 3]

When the 1st bandwidth parameter (α_1) approaches to the 2nd bandwidth parameter (α_2), the BT model tends to underestimate probabilities in high amplitude region. This fact can also affect the estimated fatigue damages by the proposed model that utilizes the

BT marginal distribution of stress amplitude. To quantify the effect of marginal distribution of stress amplitude on the estimated fatigue damages for non−Gaussian problems, another approximate model is introduced. This model uses marginal distribution of stress amplitude extracted directly from simulated data. In other words, exact probability density function of stress amplitude is utilized to eliminate the error from PDF of amplitude in estimated fatigue damages.

Fig. 62 shows the errors of the three models in the 3rd type of stress spectra. The green dash line representing joint probability distribution model with exact marginal distribution give very accurate damage estimations so most observed errors are located near zero. From these results, it is concluded that the degree of improvement seems to be significantly affected by the selection of a model for marginal distribution of stress amplitude.

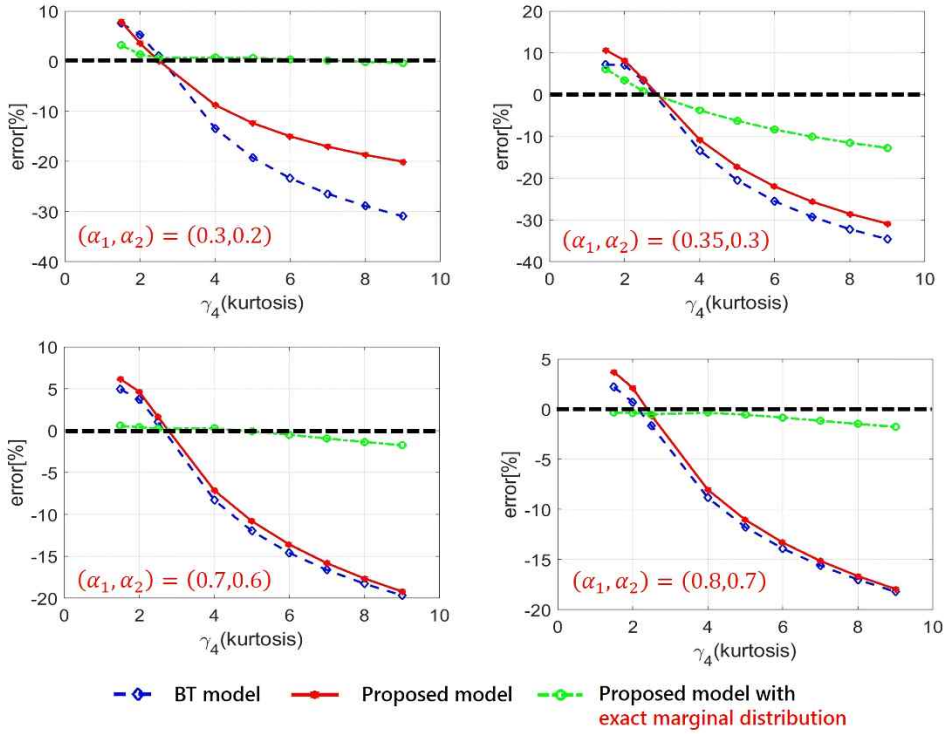

Fig. 62 The errors of fatigue damages estimated by three approximate models in the 3rd type of stress spectra (γ_3=0)

Therefore, other models for marginal distribution of stress amplitude are also taken to construct joint probability distribution of mean and amplitude with the proposed conditional probability distribution functions. Two approximate models proposed by Dirlik (1985) [DK model] and Park et al (2014) [JB model] are considered additionally. Fig. 63 shows the errors of the BT model and three models that consist of the proposed conditional probability function and three approximate models (BT, DK and JB models) for marginal distribution of stress amplitude.

DK model seems to give the worst results in this case study. In case of JB model, it seems to predict fatigue damage rate with similar

or better accuracy than the BT model. However, as the difference between the 1st and 2nd bandwidth parameters increases, this model tends to overestimate fatigue damage rate.

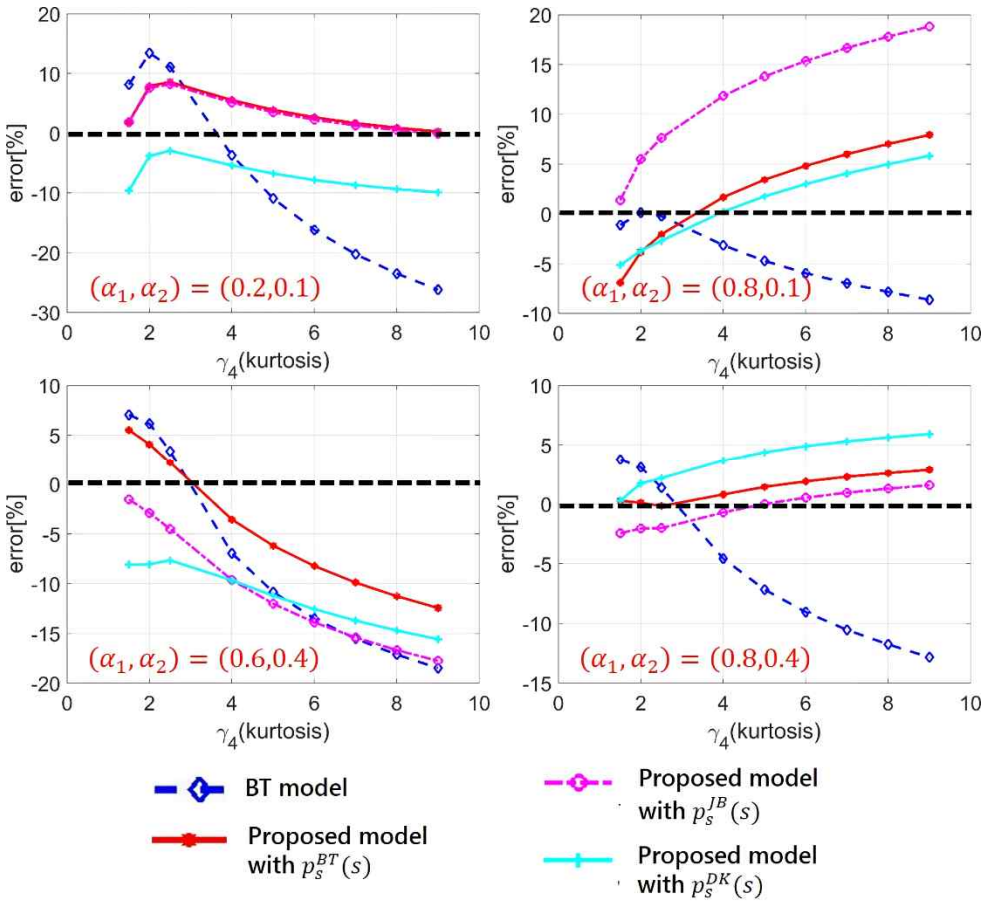

Fig. 63 The errors of fatigue damages estimated by four approximate models with different amplitude models in the 4th type of stress spectra (γ_3=0)

Chapter 6. Application on real engineering problems

6.1. Introduction

In previous chapters, the proposed model for joint probability distribution of mean and amplitude of rainflow-counted cycles is derived in wide-banded processes and the accuracy of the proposed model in evaluating fatigue damages induced by wide-banded non-Gaussian processes is verified through the idealized five different shapes of stress spectra. In this chapter, the accuracy of the proposed model is investigated once again in real engineering problems.

Two engineering problems are introduced in this chapter. The first one is engineering critical assessment (ECA) on TLP tendon. As explained in chapter 2.2, the information of stress ratio (R) is required to reflect the crack closure effect in crack propagation analysis so not only the marginal distribution of stress amplitude but also the information of stress mean is needed in ECA. Thus, it seems that joint probability distribution should be offered when crack propagation analysis is performed in frequency domain. The crack growth rates are estimated and compared by two approximate models to verify the performance of the proposed model in this example.

The other example is a fatigue analysis on offshore floating wind turbine supporting structure. Wind load is representative non-linear loading in offshore engineering. Due to the non-linearity in wind load,

corresponding structural responses seem to show non-Gaussian properties. In this example, fatigue analysis using the proposed model with the modified Hermite transformation is performed to estimate the fatigue damages of hot spot with consideration on wind and wave loads at the same time. Finally, the estimated fatigue damages are compared to the damage rate calculated from fully coupled time simulation with RFC.

6.2. Case study I – Prediction on fatigue crack growth on TLP tendon (wide-banded Gaussian process)

6.2.1. Procedure of case study I

As mentioned in chapter 2, engineering critical assessment (ECA) is started from obtaining the information of stress history. If the crack closure effect is required in ECA, not only probability distribution of stress amplitude but also entire cycle distribution such as joint probability distribution of mean and amplitude is required in ECA. The next step is defining initial crack geometry such as crack depth, length, shape and thickness. From that information, correction factor for stress intensity factor (K) can be calculated. The crack growth rate of each cycle is calculated based on Paris law and propagated crack depth is summed to estimate accumulated crack growth based on linear damage rule.

Several empirical formula for the U ratio which is the ratio of

effective stress intensity factor range (ΔK_{eff}) to stress intensity factor range (ΔK) defined in Eq. (2.8) [Elber (1971), ASTM (1999), Schjive (2004)]. In this present work, the formula proposed by Scijive as shown in Eq. (6.1) is used to evaluate effective stress intensity factor range.

$$U = 0.55 + 0.33R + 0.12R^2 \quad for \quad -1 \le R \le 1 \qquad (6.1)$$

where, $U = \frac{\Delta K_{\mathbf{ef}}}{\Delta K}$, $R = \frac{\sigma_{\mathrm{m\ in}}}{\sigma_{\mathrm{m\ ax}}}$

Another important factor that has a significant effect on crack growth rate is load sequence. However, this phenomenon is not reflected in this case study.

6.2.2. Information of simulation

- Model description

A typical TLP which accommodates total 16 number of tendon in corners is used to this simulation. The configuration of target TLP is shown in Fig. 64.

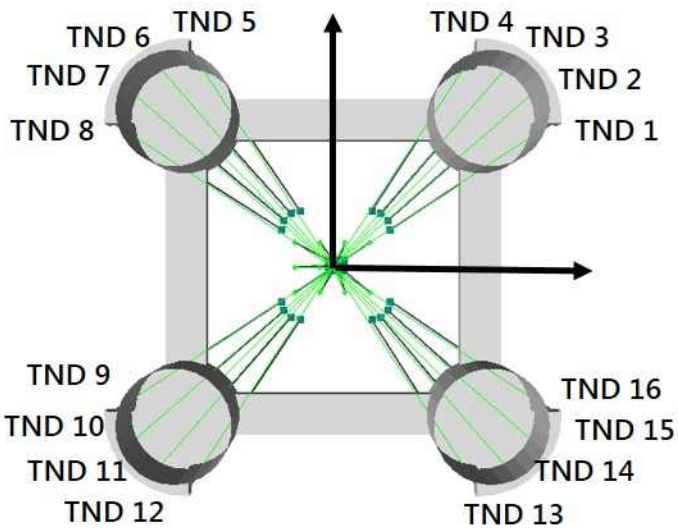

Fig. 64 Configuration of TLP in case study I

The detail information of TLP such as main dimension and mass distribution are summarized in Table 4 and 5.

Table 4 Main dimensions of TLP

Length [m]	Breadth [m]	Depth [m]	Draft [m]
107	107	44	35

Table 5 Mass and moment of inertia

Mass [ton]	I_{xx} [ton · m^2]	I_{yy} [ton · m^2]	I_{zz} [ton · m^2]
8.22×10^4	1.58×10^7	1.58×10^7	1.38×10^7

- Environmental loadings

Wave, wind and current loads are considered in TLP analysis. The target structure is assumed to be installed in Gulf of Mexico

(GOM). The 38-year sea scatter diagram in GOM as shown in Fig. 65 is used to TLP analysis. Total 61 number of sea states where significant wave height is larger than 1 meter in the scatter diagram is considered in crack propagation analysis. JONSWAP wave spectrum is selected in this simulation. The information of quadratic transfer function (QTF) from motion analysis is also used in TLP analysis.

Hs(ft) \ Tp(s)	1	2	3	4	5	6	7	8	9	10	11	12	13	14	15	sum
0	59	2193	11864	19108	10178	1997	652	242	100	47	7	1	4	2	1	46455
3	0	0	362	6316	17654	10252	1255	116	36	24	12	7	3	4	2	36043
6	0	0	0	9	1184	7820	2928	322	36	12	9	7	3	1	1	12332
9	0	0	0	0	2	463	2341	512	64	7	6	9	5	0	0	3409
12	0	0	0	0	0	0	223	470	81	9	4	3	0	0	0	790
15	0	0	0	0	0	0	3	63	61	29	6	1	0	0	0	163
18	0	0	0	0	0	0	0	2	15	14	6	2	0	0	0	39
21	0	0	0	0	0	0	0	0	3	6	4	2	1	0	0	16
24	0	0	0	0	0	0	0	0	0	4	4	0	1	0	0	9
27	0	0	0	0	0	0	0	0	0	0	2	3	2	0	0	7
30	0	0	0	0	0	0	0	0	0	1	1	2	1	0	0	5
33	0	0	0	0	0	0	0	0	0	1	0	1	2	0	0	4
36	0	0	0	0	0	0	0	0	0	0	0	1	4	0	0	5
39	0	0	0	0	0	0	0	0	0	0	1	0	0	0	0	1
42	0	0	0	0	0	0	0	0	0	0	0	1	0	0	0	1
45	0	0	0	0	0	0	0	0	0	0	0	0	1	0	0	1
sum	59	2193	12226	25433	29018	20532	7402	1727	396	154	62	40	27	7	4	99280

Fig. 65 38-year sea scatter diagram in GOM

As for wind and current loads, they are considered as constant loads in each sea state. Norwegian Petroleum Directorate (NPD) wind spectrum is used and mean wind speed at 10 meters height is taken as 41.13 m/s. Mean current velocity is taken 1.292 m/s at free surface. The heading of all excitations are assumed to come from 45 degree.

- Initial crack and correction factor of geometry

To calculate stress intensity factor range which is directly

related to crack growth, correction factor of geometry ($f(g)$) which accounts for crack geometry and specimen properties should be estimated in advance. In this example, initial crack is assumed to be located on outer diameter of TLP tendon as shown in Fig. 66. The shape of initial crack is taken as elliptic. The detailed information of crack geometry and tendon section are summarized in Table 6 and 7.

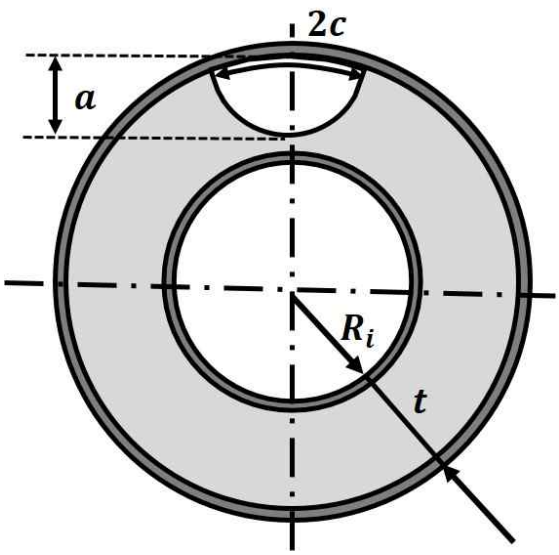

Fig. 66 Description of initial crack

Table 6 Crack dimensions and shape

Shape	Depth [mm] (a)	Length [mm] (c)
Elliptic	3	30

Table 7 Information of tendon section

Outer diameter [in]	Inner diameter [in]	Thickness [in] (t)
34	32.7	1.3

From the information of initial crack, correction factor of stress intensity factor defined in Eq. (2.5) can be calculated. The correction factor depends on the geometry and shape of initial crack. In case of plain pipe with elliptic shape crack, Hoh et al (2016) summarized the correction factor suitable for this case as shown in Eq. (6.2) and (6.3).

$$f(g) = F\left(\frac{a}{t}, \frac{a}{c}, \phi\right) \tag{6.2}$$

where, ϕ: the angle of the crack tip along the crack front

$$F\left(\frac{a}{t}, \frac{a}{c}, \phi\right) = \left[M_1 + M_2\left(\frac{a}{t}\right)^2 + M_3\left(\frac{a}{t}\right)^4\right] f_\phi g f_w \tag{6.3}$$

where, $M_1 = 1.112 - 0.08423(a/c)$, $M_2 = -0.3298 + \frac{0.6035}{0.05831 + (a/c)}$

$$M_3 = 0.5 - \frac{1}{0.4287 + (a/c)} + 14\left(1 - \frac{a}{c}\right)^{24},$$

$$g = 1 + \left[0.1 + 0.2609\left(\frac{a}{t}\right)^2\right][1 - \sin(-1.179\phi)]^2, \ f_w = 1$$

$$f_\phi = \left[\left(\frac{a}{c}\right)^2 \cos^2\phi + \sin^2\phi\right]^{1/4},$$

To account for the effect of welding, additional correction factor as shown in Eq. (6.4) can be introduced.

$$M_{k,c} = M_{k,a} + M_{k(c-a)} \tag{6.4}$$

where, $M_{k,a} = 0.003786\left(\frac{a}{t}\right)^{-1.316} + 0.9766$

$$M_{k(c-a)} = M_{k,c} - M_{k,a} = 1.871\left(\frac{a}{t}\right)^{-0.1005} - 1.56,$$

The correction factor for stress intensity factor of TLP tendon

in Eq. (6.5) is finally derived by substituting Eq. (6.3) and (6.4) into Eq. (2.5).

$$K = \sigma \sqrt{\frac{\pi a}{Q}} F\left(\frac{a}{t}, \frac{a}{c}, \phi\right) M_{k,c} \tag{6.5}$$

where, $Q = 1 + 1.464\left(\frac{a}{c}\right)^{1.65} \quad for \quad \frac{a}{c} \ll 1$

Maximum and minimum of stress intensity factor in each stress cycle can be calculated by substituting peak and valley of rainflow-counted cycle into Eq. (6.5). Then, stress intensity factor range is obtained from its definition. Finally, the corresponding effective stress intensity factor range can be evaluated by multiplying stress intensity factor range and U-ratio from Schjive formula.

6.2.3. Results

Time simulations for TLP analysis are performed by DeepC developed by DNV software. This programs give time history of effective tension (F_X) and bending moments (M_y, M_z). Time series data of hot spot stress can be evaluated by inputting the load histories into 3-D beam theory as explained in Eq. (6.6).

$$\sigma_{xx} = \frac{F_X}{A} - y\frac{M_z}{I_{zz}} - z\frac{M_y}{I_{yy}} \tag{6.6}$$

where, A: sectional area of tendon

Fig. 67 shows an example of time history of hot spot stress at the 11th tendon and the corresponding power spectral density of hot spot stress is described in Fig. 68. In the stress spectrum shown in Fig. 66, three main frequency components that are typically observed in TLP analysis are clearly expressed.

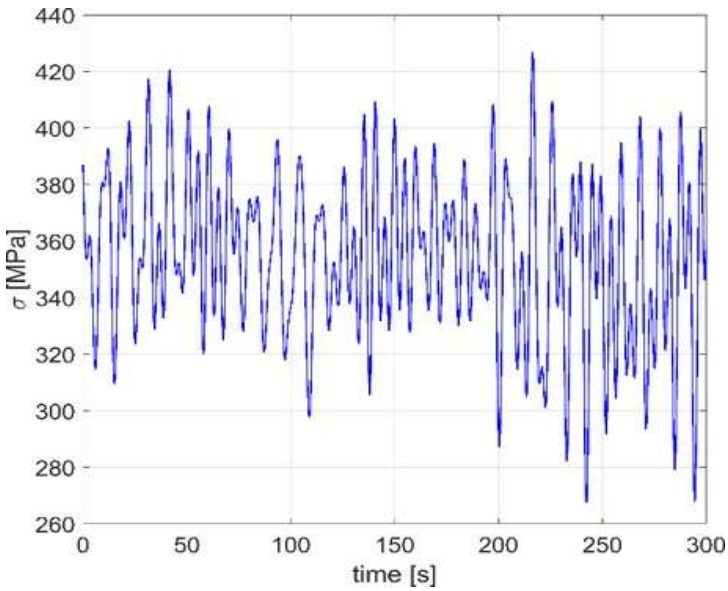

Fig. 67 An example of time history of hot spot stress at the 11th tendon in (Hs, Tp) = (9.1m, 10s)

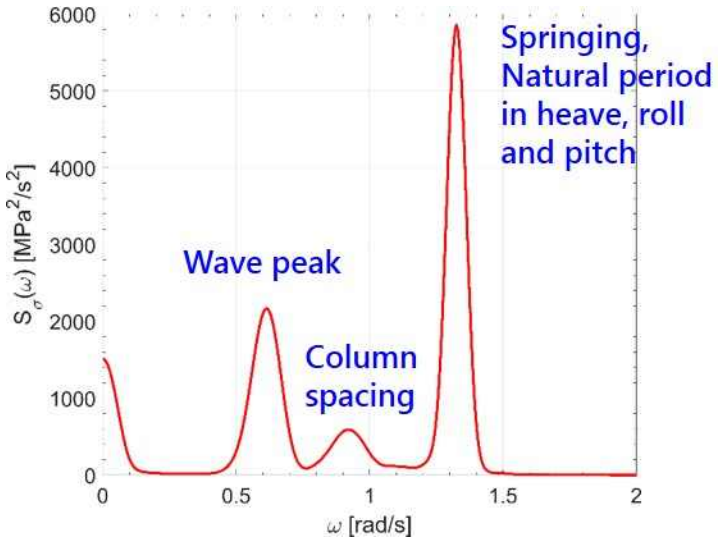

Fig. 68 Power spectral density of hot spot stress at the 11th tendon in (Hs, Tp) = (9.1m, 10s)

Two approximate models estimate the joint probability distribution of mean and amplitude: the BT and proposed model in this present work. Spectral moments of power spectral densities are calculated in all sea states and the 1st and 2nd bandwidth parameters which are the input variables of approximate models are estimated. The 1st and 2nd bandwidth parameters of hot spot stresses and its 1st derivative are plotted in Fig. 69 and 70. As seen in Fig. 67, most bandwidth parameters are located near unity. It means that hot spot stresses at tendon seem to be close to narrow-banded Gaussian processes.

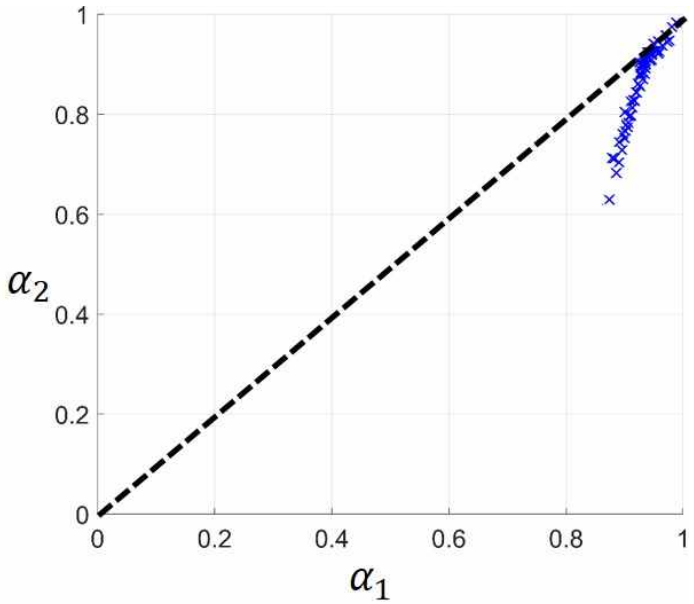

Fig. 69 Scatter plot of the 1st and 2nd bandwidth parameters of hot spot stresses at the 1st tendon in all sea states

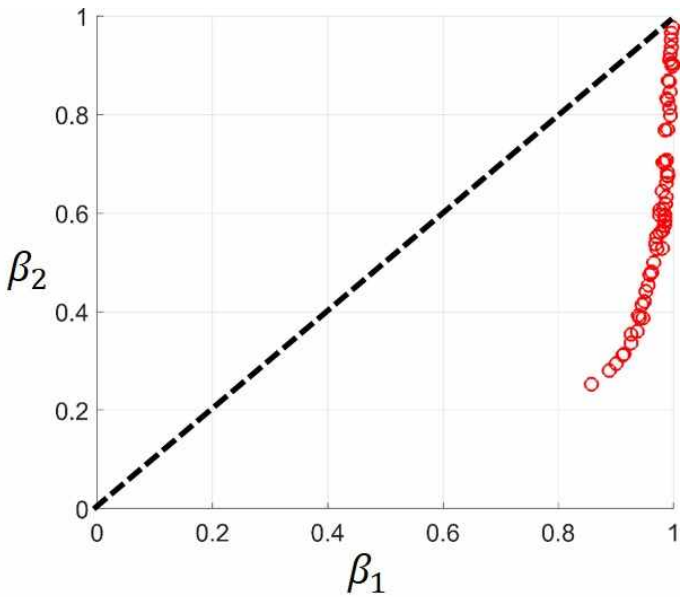

Fig. 70 Scatter plot of the 1st and 2nd bandwidth parameters of the 1st derivative of hot spot stresses at the 1st tendon in all sea states

The joint probability distribution of mean and amplitude can be estimated input variables from given spectral density into the approximate models. Fig. 71 and 72 show the simulated data and estimated JPD by two models. In Fig. 71, two model gives similar prediction on the JPD of mean and amplitude. In Fig. 72, the BT model seems to give poor representation of scatter plot of simulated data. On the other hands, the proposed model also give a good agreement on the simulated results in Fig. 72.

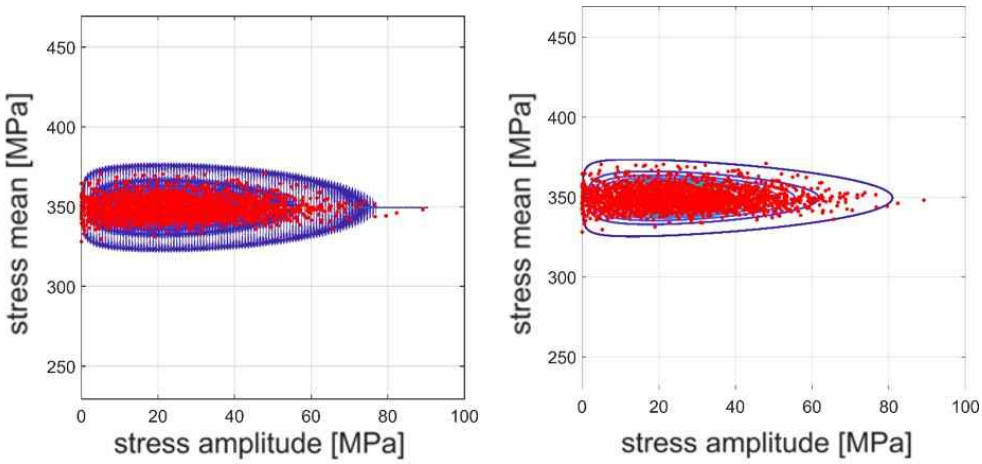

Fig. 71 Simulated data (red dot) and estimated joint probability distribution of mean and amplitude by the BT (left) and proposed models (right) [the 1st tendon, (Hs, Tp) = (4.6m, 8s)]

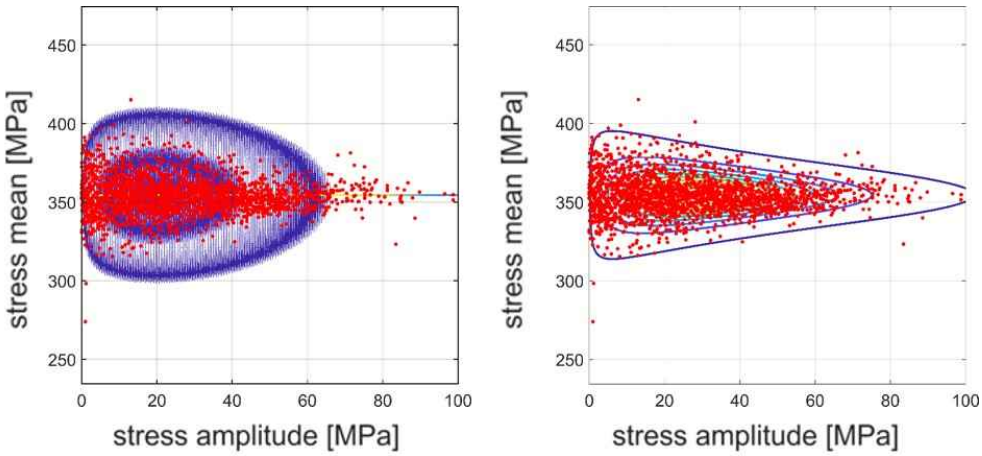

Fig. 72 Simulated data (red dot) and estimated joint probability distribution of mean and amplitude by the BT (left) and proposed models (right) [the 1st tendon, (Hs, Tp) = (10.1m, 13s)]]

The differences observed in JPD of mean and amplitude also affect the marginal distribution of stress intensity factor ranges. The exceedance probabilities of stress intensity factor ranges are shown in Fig. 73 and 74 in log scale. Relatively larger errors between simulated data and estimated exceedance probability by the BT model are observed in the 2nd sea state similar to JPD results.

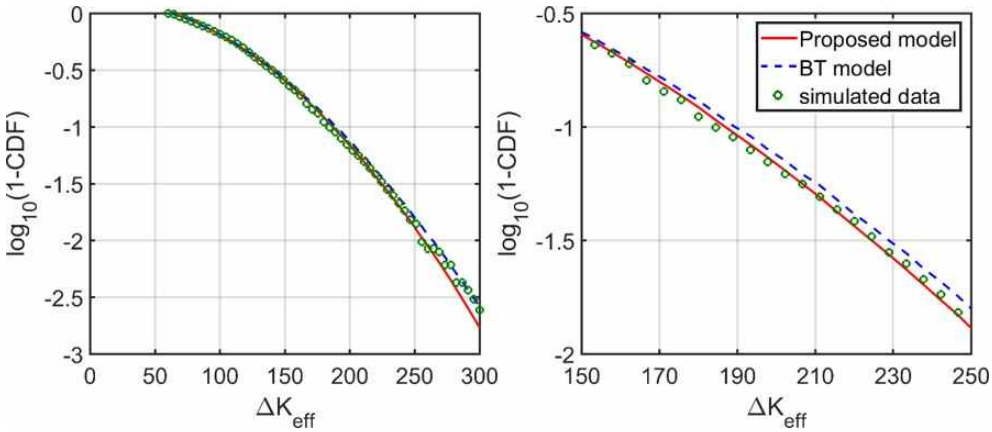

Fig. 73 The simulated data and estimated exceedance probabilities of effective stress intensity range in whole range (left) and zoomed in high range region (right) by two models [the 1st tendon, (Hs, Tp) = (4.6m, 8s)]

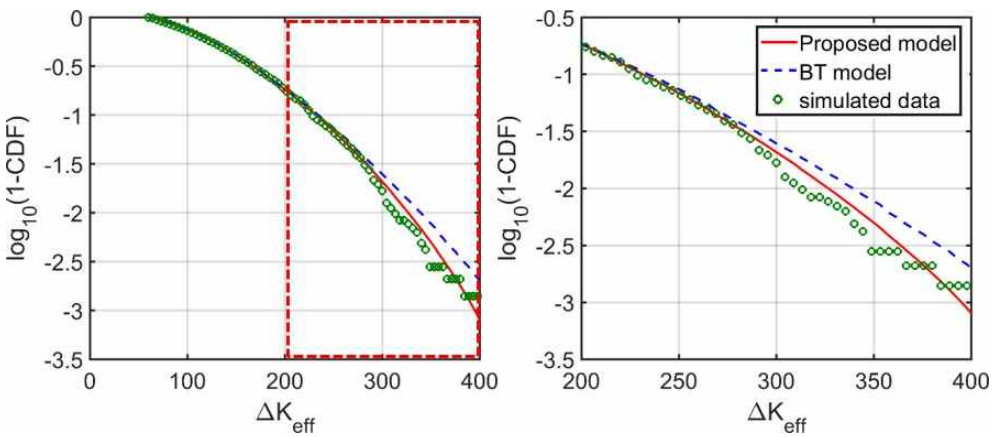

Fig. 74 The simulated data and estimated exceedance probabilities of effective stress intensity range in whole range (left) and zoomed in high range region (right) by two models [the 1st tendon, (Hs, Tp) = (10.1m, 13s)]

Finally, the simulated and estimated crack growth predictions are summarized in Fig. 75. The expected values of crack depth of the 3rd

and 11th tendons are significantly larger than the other tendons because they are located in along with the direction of wave heading.

The predictions of the BT model expressed as blue dash line always overestimate the crack growth rate. On the other hands, the predictions of the proposed model seems to give better representation on actual crack growth rates.

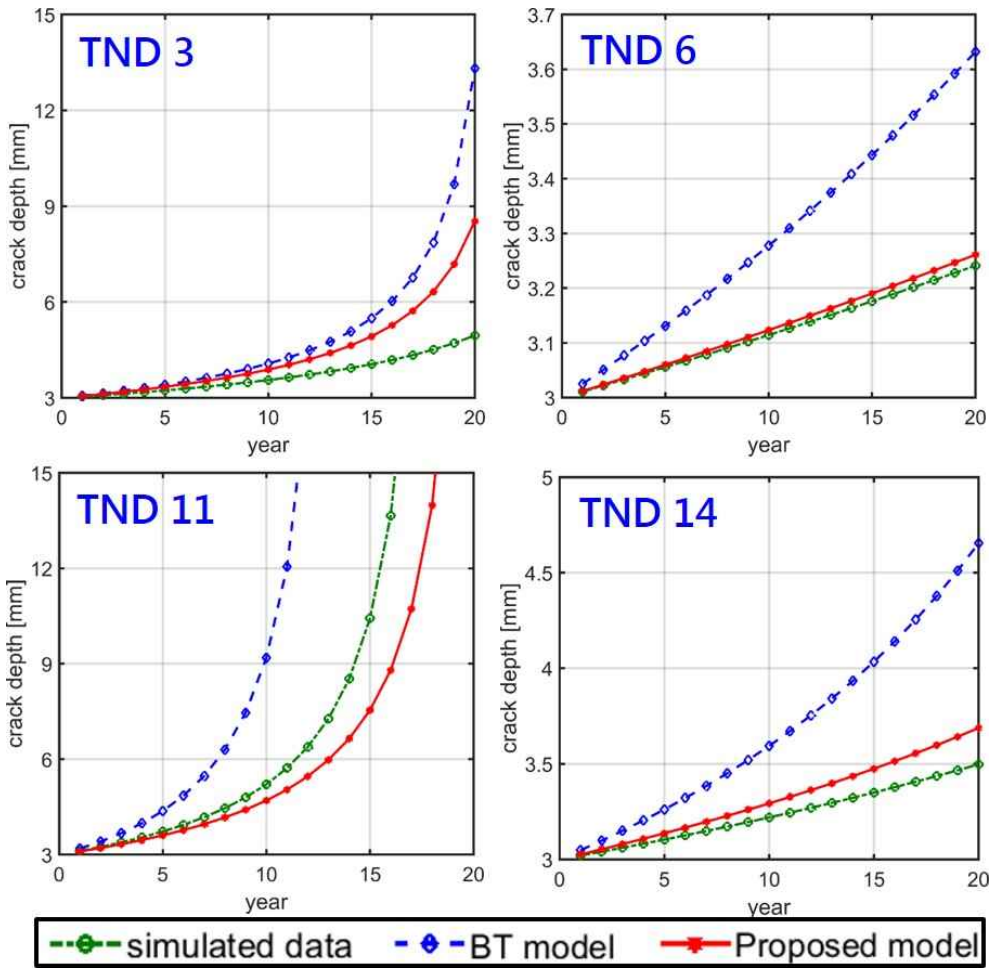

Fig. 75 Results of crack propagation analysis evaluated by time domain analysis with RFC and two frequency domain approaches

6.3. Case study II – Fatigue analysis on floating wind turbine support structure (wide-banded non-Gaussian process)

Wind load is one of the representative non-linear environmental loading. The effect of wind load is relatively smaller than that of wave load in most offshore platforms so wind load is assumed as constant load in these cases. However, in these days, requirements on renewable energy have been increased and offshore wind energy has been focused on in several decades.

In floating wind turbine platforms, the effect of wind load on fatigue damages in supporting structures is significant. Therefore, in this case, non-linearity of wind load should be considered in fatigue analysis on this structure. Due to non-linearity of wind loads, hot spot stresses induced by wind load show non-Gaussian properties. We aim at verifying the accuracy of the proposed model in dealing with fatigue analysis for non-Gaussian problems through this case study.

6.3.1. Information of simulation

- Model description

The WWHybrid system in this study consists of long-span beams. Fig. 76 shows a configuration of this system, the detailed information on which is summarized in Table 8 and 9. The pontoon

structure located at the bottom consists of outer pontoons, inner pontoons and diagonal pontoon braces. The upper deck structure is formed in the same way as the pontoon structure. The pontoon and upper deck structures are connected by 21 columns. The four wind turbines are located at the corners of the upper deck structure, respectively, and at each side, six wave-energy converters are installed. These wave-energy converters are modeled as fixed bodies in the time and frequency analyses, simply because they are outside the scope of the present study. This system is moored at the corner columns by eight catenary mooring lines (chains). Boundary condition should be applied to avoid rigid body motion of a structural model and at least 6 degree of freedom should be fixed. Statically determined boundary conditions addressed by DNV (2012) is applied to the target structure for structural analysis as shown in Fig. 77.

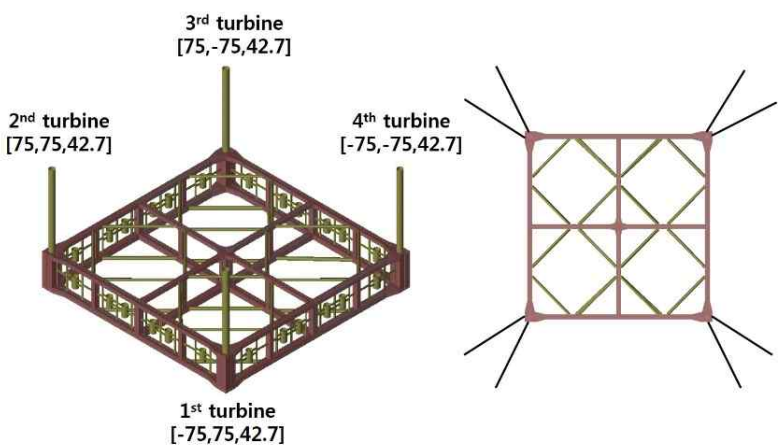

Fig. 76 Structural modeling of WWHybrid system

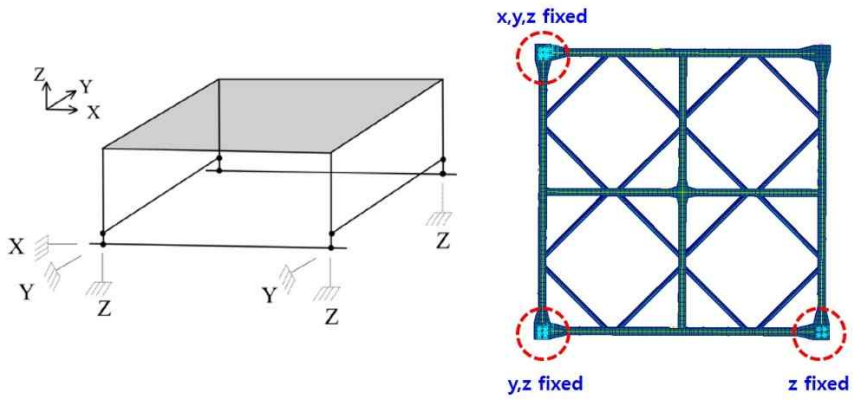

Fig. 77 Boundary condition for structural analysis [DNV-RP-C103 (left), structural model (right)]

The capacity of the wind turbine used in this simulation is 3 MW. The cut-in, cut-out and rated wind speeds of this turbine are 4, 25, and 11.7 m/s, respectively. Because the four wind turbines are operated at the same time in this system, the wake effect on turbines located behind can be significant. As for the control system, the configuration of turbine in this work was variable-speed and variable-pitch(VS-VP). This means that turbine responses such as power and rotational speed above the rated wind speed were managed by controlling the pitch angle.

Table 8 Main dimensions of WWHybrid system

Platform		
LOA [m]	Breadth [m]	Depth [m]
158.5	158.5	27
Wind turbine		
Capacity [MW]	Diameter [m]	Height [m]
2	105	61.4

Table 9 Mass, Hydrostatic data of WWHybrid system

Total Mass [tons]	26,900
Heave-Heave restoring coefficient [ton/s2]	9.09×10^3
Roll-Roll restoring coefficient [ton/s2]	3.27×10^7
Pitch-Pitch restoring coefficient [ton/s2]	3.27×10^7
Nacelle mass [tons]	103
Hub mass [tons]	30

- Environmental loadings

As mentioned above, the goal of this case study is verifying the performance of the proposed model in assessment on fatigue damage induced by non-Gaussian random loading. Because non-linear wind loads causes non-normality of hot spot stresses of floating wind turbine, various wind speeds are considered in this case study. The wind speeds ranges from the cut-in speed (4m/s) to the cut-out speed (25m/s). Total 6 number of different wind speeds are included in load cases.

As for wave and current loads, the effects of these loadings on non-normality of hot spot stress are not significant. Therefore, we use mild sea condition and fix sea state and mean current velocity in all load cases. Finally, total six number of load cases are considered in this case study and the detail information is summarized in Table 10.

Table 10 The information of load cases in case study II

$V_w[m/s]$	$(Hs[m], Tp[s])$	$V_c[m/s]$
4	(0.5,13)	0.14
6	(0.5,13)	0.14
11.7	(0.5,13)	0.14
15	(0.5,13)	0.14
20	(0.5,13)	0.14
25	(0.5,13)	0.14

6.3.2. Results

Time simulations were performed in all of the fatigue bins to obtain the exact fatigue damage of the hot spots. MUFOWT developed by Texas A&M University was used to perform a coupled time-domain analysis for the WWHybrid system. This tool can handle wind, wave and current at the same time by integrating FAST for aerodynamic loads and CHARM3D for hydrodynamic loads (Bae et al., 2014 and Kang et al., 2013). This could provide a time series of wind loads acting on the tower base and 6-DOF platform motions

at the platform' s COG, considering all of the relevant loads. The duration of the time simulation was 4,000 s including the transient state.

The position of the hot spot was determined at the tower bases of the 1st turbine [Fig. 78]. In order to obtain the time series of hot-spot stress, FE analysis is required in every time step. However, instead of FE analysis, a stress-effect factor was used to calculate the hot-spot stress induced by wind and wave loads efficiently. The stress-effect factors are the structural responses induced by unit force and moment. If it is possible to assume that structural responses have a linear relationship to applied loads, a time series of the hot-spot stress induced by arbitrary loads can be computed, simply by multiplying the stress-effect factors by the time series of the loads.

Wind load was computed at the tower base. On the other hand, the inertial force induced by the platform motion was computed at the tower' s COG, because the lumped mass of the tower was assumed to be concentrated at the tower' s COG. The acting point of the wind load was moved to the tower' s COG to reduce the number of required stress-effect factors. Thus, it could be said that the stress-effect factors in this simulation were the structural responses of the hot-spot locations induced by unit force and moment applied at the tower' s COG. NASTRAN solver was used to calculate the stress-effect factors in this problem.

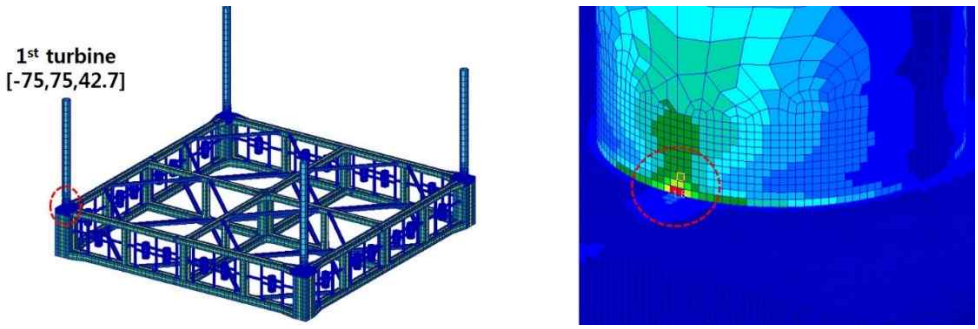

Fig. 78 FE model and hot-spot location

An example of time series of hot spot stress is shown in Fig. 79. Due to non-linear wind loads, hot spot stress shown in Fig. 79 seems to be positively skewed.

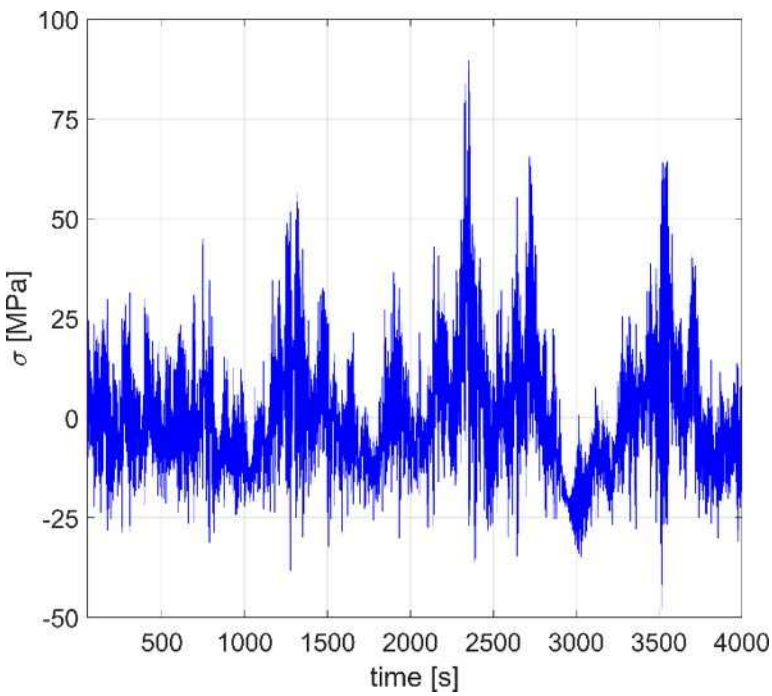

Fig. 79 An example of time history of hot spot stress in the 1st load case (V_w=4m/s)

The corresponding power spectral density is also plotted in Fig. 80. Two main frequency components related to slowly varying wind speed and the 1st natural frequency of tower are clearly shown in Fig. 80. Because mild sea condition is taken in this simulation, wave frequency component is not observed in the spectrum.

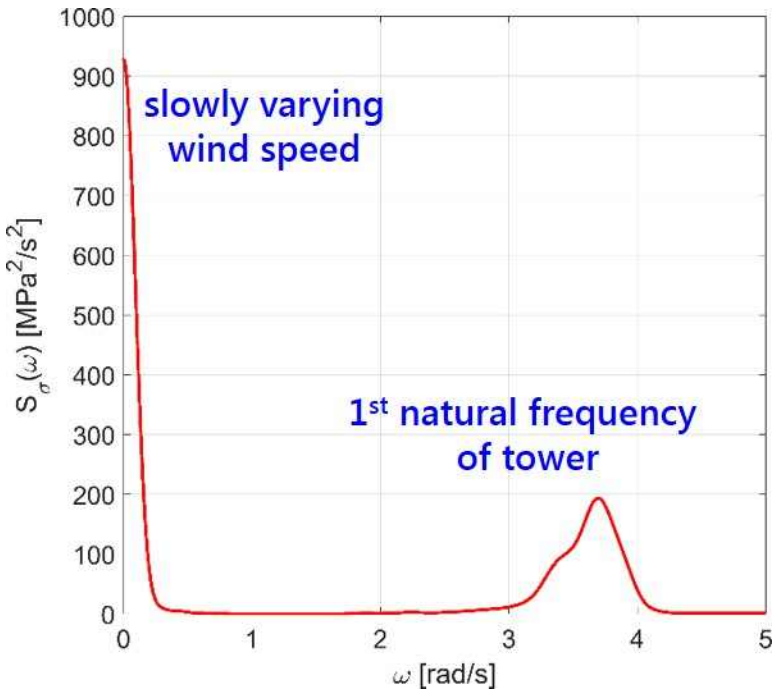

Fig. 80 The corresponding power spectral density of hot spot stress in the 1st load case

Unlike the previous case study, the hot spot stresses in this case study are close to wide-banded process as seen in Fig. 81. The simulated skewness and kurtosis of hot spot stresses are summarized in Fig. 82 in all load cases. We expect that the non-linearity of wind load makes hot spot stress non-normal process and as the wind speed increases, non-normality will also increase.

However, as seen in Fig. 82, the kurtosis value of hot spot stress go to 3 as wind speed increases and hot spot stresses are mildly non-Gaussian process except the 1st load case where wind speed is the lowest among load cases.

When wind speed reaches the rated speed, the pitch control system would change the pitch angle to reduce the wind load acting on turbine blade. Thus, we consider that wind load would be stable after wind speed exceeds the rated speed due to the pitch control algorithm.

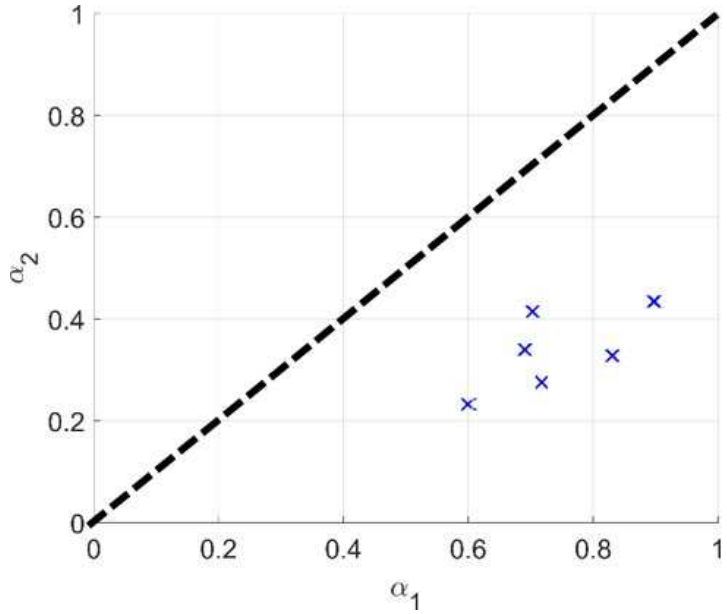

Fig. 81 Scatter plot of the 1st and the 2nd bandwidth parameters of hot spot stresses

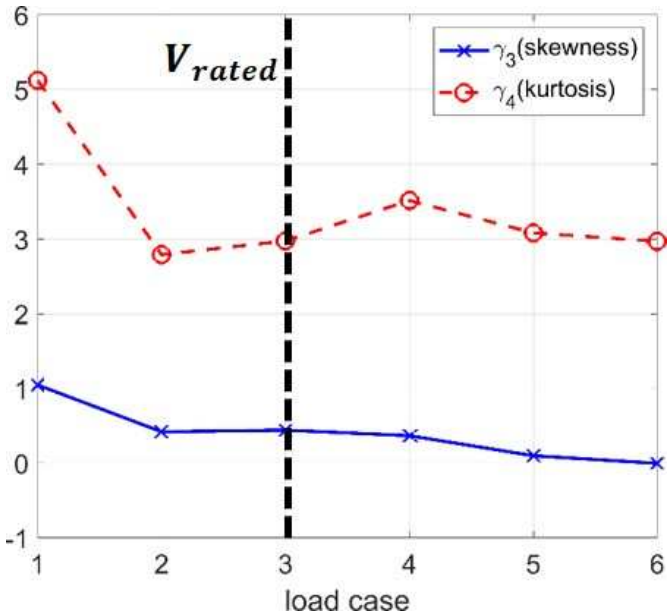

Fig. 82 Skewness and kurtosis of hot spot stresses

In short, only the time history of hot spot stress in the 1st load case seems to be wide-banded non-Gaussian process. Because we intend to analyze non-Gaussian process through this case study, we only focus on the 1st load case. Fig. 83 and 84 compare simulated data expressed as red dot and estimated joint probability distribution of mean and amplitude by two models.

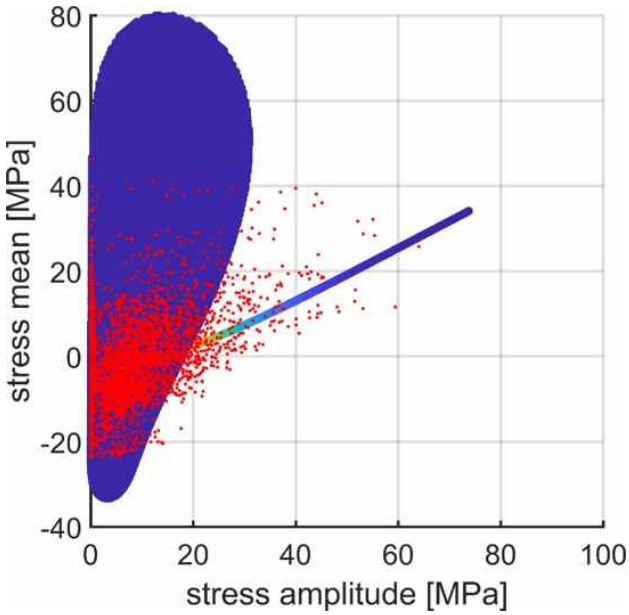

Fig. 83 Simulated and estimated joint probability distribution of mean and amplitude by the BT model in the 1st load case

As mentioned in chapter 3, the BT model seems to distort the probability in high amplitude region due to symmetric assumption on level-crossing counted cycle distribution. Due to non-zero skewness value, the estimated and simulated data are positively skewed processes. By comparing Fig. 83 and 84, it can be concluded that the proposed model seems to give a better representation of simulated data.

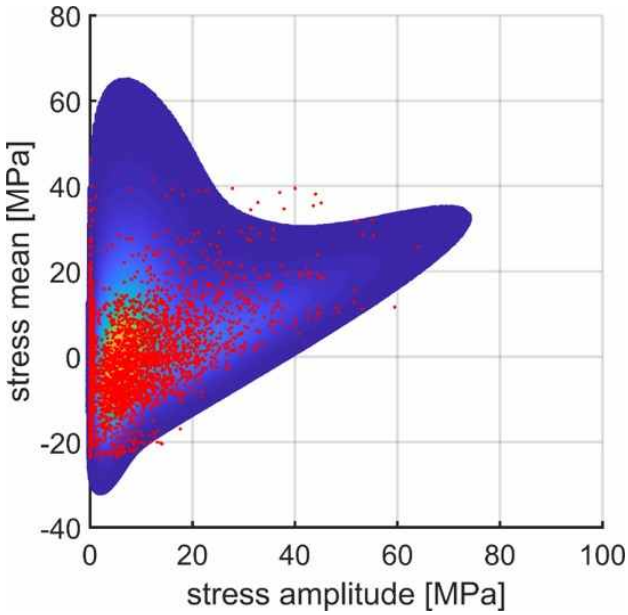

Fig. 84 Simulated and estimated joint probability distribution of mean and amplitude by the proposed model in the 1st load case

Fig. 85 shows predictions of exceedance probabilities of stress amplitude in log scale. The predicted exceedance probability by the BT model seems to underestimate the exceedance probability in high amplitude. The simulated data shows a little deviation from estimated exceedance probability model in low amplitude region and would be close to the estimated exceedance probability by the proposed model after the normalized amplitude reaches 2.

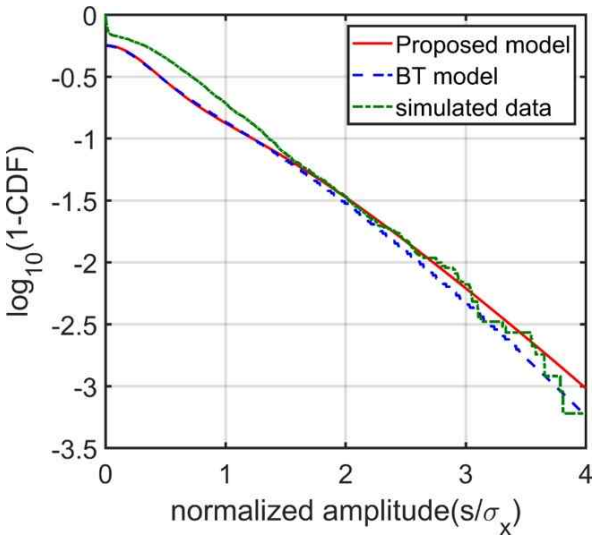

Fig. 85 Simulated and estimated exceedance probability of normalized stress amplitude in log scale (the 1st load case)

Finally, fatigue damages estimated by two models are compared in Fig. 86.

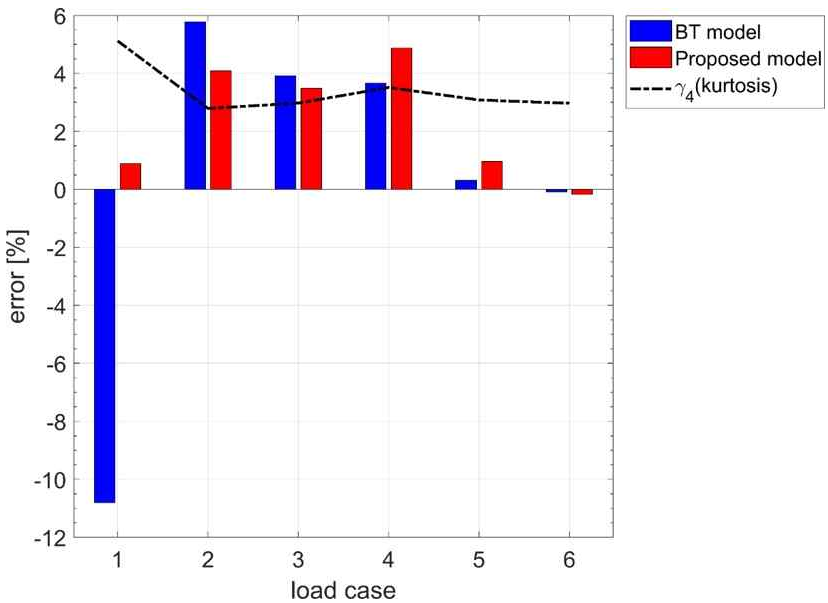

Fig. 86 The errors of two models in all load cases

Chapter 7. A linearization coefficient for Morison force considering intermittent effect

7.1. Introduction

Slender members have widely been used in many offshore structures such as offshore fixed wind turbines and jacket structures. In general, wave forces acting on these slender members are calculated from the Morison' s equation in combination with linear random wave theory. The validity of linear random wave theory used to predict the particle kinematics in random wave field was proven at continuously submerged points by Charkrabarti (1980). However, if points of interest are located near the free surface, the particle kinematics are changed due to the intermittent effect. Wave forces act discontinuously at those points because that points are intermittently submerged due to free surface fluctuation. The phenomenon that fluid particle kinematics change by free surface fluctuation is called the intermittent effect. Tung (1975) proposed linear intermittent random wave theory that calculates particle kinematics in intermittent flow by linear random wave theory below the free surface and assuming that all properties are zero above the free surface. The probability density functions and statistical moments of particle velocity, acceleration and pressure were derived through the linear intermittent random wave theory. Anastasiou et al (1982) indicated the importance of second-order effects in wave

forces and Tung and Huang (1983, 1985) derived the probabilistic models and particle kinematics in intermittent flow using the second-order Stokes wave theory. Tung (1995) conducted a study on the magnitude of the effect of the intermittent effect and the conditions that could have a significant effect.

The Morison's equation consists of two terms. The first one is drag force which is proportional to the square of velocity and the other one is inertia force which is proportional to acceleration. Due to nonlinearity in drag force, it is difficult to calculate force spectral density. Borgman (1967) suggested force spectral density for fully submerged case. Because it is not easy to estimate force spectral density reflecting the complete form of Morison's equation as it is, a linearization coefficient was introduced to linearize nonlinear drag term in the Morison's equation. Pajouhi and Tung (1975) extended Tung's work (1975) to derive covariance function of Morison force which preserves nonlinear drag term. The force spectral density which is a Fourier transform pair of the covariance function was also derived by numerical integration of a lengthy formula in their work. Approximate form of force spectral density was also suggested to simplify formula for force spectral density. Isaacson and Baldwin (1990a, 1990b) proposed analytic formula for the probability density function of force maxima and simplified force spectral density near the free surface and verified the formula by experiments. The intermittent effect was not significant below the free surface but the force spectrum was greatly reduced by the intermittent effect above the surface. Isaacson and Subbiah (1991) verified the derived

theoretical model through numerical analysis in time domain and mentioned the effect of simulation time and random phase of wave on numerical analysis results.

Many researches pointed out the limitation of Borgman's linearization coefficient. Brouwers and Verbeek (1983) compared fatigue damages and extreme responses caused by nonlinear drag and linearized drag force calculated by Borgman's coefficient (1967). The linear method significantly underestimated the expected fatigue damages and extreme response when drag is dominant. An alternative approach to determine the linearization coefficient for drag force in Morison's equation was investigated by Wolfram (1999). He explained that a least-square approach used in Borgman's work was adequate if the ultimate goal was to minimize the time average of nonlinear and linearized drag force. However, in engineering point of view, truly important things are extreme response or fatigue damage, not load itself. Proposed linearization approach was to find the coefficient that could match the expectation values of force maxima of nonlinear and linearized drag force.

Existing linearization coefficients suggested by Borgman and Wolfram were estimated based on fully submerged condition. Isaacson and Baldwin (1990b) also proposed linearization coefficient in intermittent flow but it was also obtained by a least-square method that may underestimate extreme responses and fatigue damages. In this chapter, the linearization coefficient in intermittent flow is investigated. The expectation values of force maxima of nonlinear and linearized drag force in intermittent flow are derived. Finally, the

linearization coefficient is proposed by comparing two-expectation value and is verified by numerical simulations.

7.2. Linear intermittent random wave theory and the probabilistic density function of force maxima

7.2.1. Linear intermittent random wave theory

The linear random wave theory (LRWT) has been verified in a number of studies for its accuracy in predicting particle kinematics at a fully submerged point. The surface elevation derived from the LRWT follows a zero-mean Gaussian process and could be expressed as a wave spectrum in frequency domain. Particle velocity and acceleration at x = 0 are linearly proportional to the surface elevation and its derivative as Eq. (7.1) ~ (7.3).

$$\eta(x,t) = \frac{H}{2}\cos(\omega t) \tag{7.1}$$

where, η: surface elevation, H: wave height

ω: angular frequency, t: time

$$u(z,t) = \frac{H}{2}\omega G(z)\cos(\omega t) = u_0 G(z)\cos(\omega t) = \omega G(z)\eta \tag{7.2}$$

where, u : horizontal particle velocity, d : water depth,

$u_0 = \frac{H}{2}\omega$: velocity amplitude, k: wave number

$G(z) = \frac{\cosh\,(k(z+d))}{\sinh\,(kd)}$ where $z \le 0$, otherwise $G(z) = \frac{1}{\tanh\,(kd)}$,

$$a(z,t) = \frac{\partial u}{\partial t} = -\frac{H}{2}\omega^2 G(z)\sin(\omega t) = -u_0 \omega G(z)\sin(\omega t) = \omega G(z)\dot{\eta} \quad (7.3)$$

where, a : horizontal particle acceleration

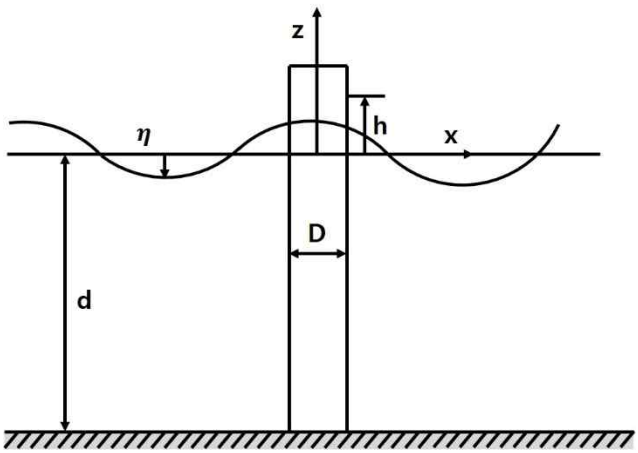

Fig. 87 Definition of coordinate system and variables

However, near the free surface, the particle kinematics are discontinuous due to the surface fluctuation. Tung (1975) proposed the linear intermittent random wave theory to express particle kinematics in intermittent flow as described in Fig. 87. This approach estimates particle kinematics near the free surface by comparing the surface elevation (η) and observation position (h). When η is larger than h, which means that the observation point is immersed, particle kinematics are calculated based on LRWT and otherwise all properties are assumed to be zero. The particle velocity (u') and acceleration (a') in intermittent flow derived from the linear intermittent random wave theory are expressed as Eq. (7.4) mathematically.

$$u'(z,t) = u(z,t)Y(\eta(t)-h), \quad a'(z,t) = a(z,t)Y(\eta(t)-h) \qquad (7.4)$$

where, Y(x): Heaviside function, $Y(x) = \begin{cases} 0, & x < 0 \\ 1, & x \geq 0 \end{cases}$

The probability density functions of the particle velocity ($p(u')$) and acceleration ($p(a')$) at h are expressed by Tung (1975) as Eq. (7.5) and (7.6).

$$p(u') = [1 - Q(b)]\delta(u') + \frac{1}{\sigma_u} Z\left(\frac{u'}{\sigma_u}\right) Q\left(\frac{b - \frac{ru'}{\sigma_u}}{\sqrt{1-r^2}}\right) \qquad (7.5)$$

where, σ_u: the standard deviation of particle velocity at h,

$\delta(x)$: Dirac delta function

$r = \frac{1}{\sigma_\eta \sigma_u} \int_0^\infty S_{u\eta}(\omega)\, d\omega = \frac{1}{\sigma_\eta \sigma_u} \int_0^\infty \omega G(z) S_\eta(\omega)\, d\omega$

σ_η : the standard deviation of elevation, $b = \frac{h}{\sigma_\eta}$,

$Z(\lambda) = \frac{1}{\sqrt{2\pi}} exp\left(-\frac{\lambda^2}{2}\right)$, $Q(b) = \int_b^\infty Z(\lambda) d\lambda$

$$p(a') = [1 - Q(b)]\delta(a') + \frac{1}{\sigma_a} Z\left(\frac{a'}{\sigma_a}\right) Q(b) \qquad (7.6)$$

where, σ_a : the standard deviation of particle acceleration at h

The Q in above equations is the probability that the surface elevation exceeds the observation height. When the observation point is always submerged, Q goes to unity and the probability density function of u' and a' become Gaussian distribution like fully submerged case. Pajouhi and Tung (1975) derived spectral density

functions for particle velocity, acceleration and pressure in intermittent flow by extending Tung' s work (1975) as Eq. (7.7) and (7.8).

$$S_{u'}(\omega) = \left[\omega G(z)Q(b) + \frac{\sigma_u}{\sigma_\eta} rbZ\ (b)\right]^2 S_\eta(\omega) = |H_{u'}(\omega)|^2 S_\eta(\omega) \qquad (7.7)$$

where, $S_{u'}(\omega)$: spectral density of velocity in intermittent flow

$H_{u'}(\omega)$: transfer function for particle velocity

$S_\eta(\omega)$: wave spectrum,

$$S_{a'}(\omega) = [-i\omega^2 G(z)Q(b)]^2 S_\eta(\omega) = |H_{a'}(\omega)|^2 S_\eta(\omega) \qquad (7.8)$$

where, $H_{a'}(\omega)$: transfer function for particle acceleration

7.2.2. Force spectral density

The Morison' s equation is widely used to calculate the wave force acting on the slender member and it consists of drag force and inertia force term as shown in Eq. (7.9).

$$F = F_D + F_I = \frac{1}{2}\rho C_d D u|u| + \rho\left(\frac{\pi D^2}{4}\right) C_m a$$

$$= K_d u_0^2 \cos\omega t\,|\cos\omega t| - K_m u_0 \omega \sin\omega t \qquad (7.9)$$

where, ρ: sea water density [kg/m3],

D: the diameter of the member

C_d, C_m: empirical drag and inertia coefficients

$K_d = {}^1/_2\,\rho C_d D, K_m = \rho\left({}^{\pi D^2}/_4\right) C_m$

It is difficult to obtain force spectral density for a complete form of Morison' s equation due to the nonlinear drag term in it. Borgman (1967) derived the force spectral density for fully submerged member by linearizing the nonlinear drag term. He introduced linearization coefficient to linearize the Morison' s equation. By substituting the coefficient, Morison' s equation could be linearized as Eq. (7.10) and the force spectral density for fully submerged case could be derived as Eq. (7.11).

$$F_l = K_d \beta u + K_m a = \overline{K}_d u_0 \cos \omega t - K_m u_0 \omega \sin \omega t \tag{7.10}$$

where, $\beta = \sqrt{\frac{8}{\pi}} \sigma_u$, $\overline{K}_d = K_d \beta$

$$S_F(\omega) = K_d^2 \beta^2 S_u(\omega) + K_m^2 S_a(\omega) = \omega^2 G^2(z) \left[K_d^2 \beta^2 + K_m^2 \omega^2 \right] S_\eta(\omega) \tag{7.11}$$

where, $S_u(\omega) = \omega^2 G^2(z) S_\eta(\omega)$, $S_a(\omega) = \omega^4 G^2(z) S_\eta(\omega)$

When the points of interest are located near the free surface, it is hard to assume that particle velocity u' is a Gaussian process. Pajouhi and Tung (1975) proposed a lengthy formula for covariance function and spectral density for a complete form of Morison' s equation which retains the nonlinear drag term considering the intermittent effect. The force spectral density could be obtained by integrating the covariance function numerically so they gives approximate form of force spectral density based on Taylor series expansion. Isaacson and Baldwin (1990b) pointed out necessity for

modification of linearization coefficient in intermittently submerged case and derived a linearization coefficient as Eq. (7.12).

$$\beta' = \frac{< |u'|^3 >}{< u^2 >} \tag{7.12}$$

where, $\langle \cdot \rangle$: the time−averaged or expectation value

Expectation values required to calculate (7.12) could be estimated numerically from probability distribution function of u' in (7.5). The approximate form of force spectral density ($S_{F'}(\omega)$) in intermittent flow was derived by using the linearization coefficient, β and spectral densities of u' and a' as Eq. (7.13) [Isaacson and Baldwin (1990b)].

$$S_{F'}(\omega) = K_d^2 \beta^2 \, S_{u'}(\omega) + K_m^2 S_{a'}(\omega)$$
$$= \left\{ K_d^2 \beta^2 \left[1 + \frac{\sigma_u r b Z\ (b)}{\sigma_\eta Q(b) \omega G(z)} \right]^2 + K_m^2 \omega^2 \right\} \omega^2 G^2(z) Q^2(b) S_\eta(\omega) \tag{7.13}$$

7.2.3. The probabilistic density function of force maxima

From the structural design point of view, extreme responses and fatigue damage are of interest rather than load itself. Therefore, many studies were conducted to derive not only the probability distribution function of the force but also the force maxima that is related to the extreme load. In fully submerged case, force maxima

occurs when the time derivative of Eq. (7.9) goes to zero so the maximum value of Morison force is expressed as Eq. (7.14).

$$F_P(z) = \begin{cases} u_0 \omega G(z) K_m & [\text{for} \quad u_0 \le \frac{\sigma_u}{2K}] \\ u_0^2 G^2(z) K_d + \frac{K_m^2 \omega^2}{4K_d} & [\text{for} \quad u_0 > \frac{\sigma_u}{2K}] \end{cases} \tag{7.14}$$

where, F_P : force maxima,

$K = \frac{K_d \sigma_u}{K_m \omega}$ (the ratio of drag force to inertia force)

Borgman (1965) derived the probability density function of force maxima for narrow banded wave spectrum in fully submerged member as shown in Eq. (7.15).

$$p(\zeta) = \begin{cases} \zeta exp\left(-\frac{1}{2}\zeta^2\right) & [\text{for} \quad \zeta < \zeta_c] \\ \zeta_c exp\left(-\frac{1}{2}\zeta_c(2\zeta - \zeta_c)\right) & [\text{for} \quad \zeta \ge \zeta_c] \end{cases} \tag{7.15}$$

where, $\zeta = \frac{2\sqrt{2}F_P}{\omega_0^2 K_m H_{rm\,s} G(z)}$, ω_0 : modal frequency

$H_{rm\,s}$: the root−mean−square wave height ,

$\zeta_c = \frac{\sqrt{2}K_m}{K_d H_{rm\,s} G(z)}$

The probabilistic distribution model of force maxima near the free surface also changes due to the intermittent effect. Although a continuous force reaches its maximum, force maxima observed near the free surface could differ from peak value of the continuous force if waves do not reach the observation point. In other words, the value of force maxima near the free surface could be influenced by the

relation between the phase (θ_m) at which the peak value of continuous force occurs and the phase (θ_0) when water first reaches the observation point. Isaacson and Baldwin (1990b) derived the value of force maxima in intermittent flow by using the relationship between θ_m and θ_0 as shown Eq. (7.16) and the probability density function of force maxima was also derived as Eq. (7.17).

$$F_P(h) = \begin{cases} 0 & \left[\text{for} \quad \frac{H}{2} < h\right] \\ u_0^2 G^2(z) K_d \cos\theta_0 \,|\cos\theta_0| - u_0 \omega G(z) K_m \sin\theta_0 & \left[\text{for} \quad \frac{H}{2} \geq h \text{ and } \theta_0 > \theta_m\right] \\ u_0^2 G^2(z) K_d + \frac{K_m^2 \omega^2}{4K_d} & \left[\text{for} \quad \frac{H}{2} \geq h \text{ and } \theta_0 \leq \theta_m\right] \end{cases} \quad (7.16)$$

where, $\theta_0 = \cos^{-1}\left(\frac{2h}{H}\right)$, $\theta_m = -\frac{\pi}{2}$ for $K_m \geq G(z)HK_d$

otherwise $\theta_m = -\sin^{-1}\left(\frac{K_m}{G(z)HK_d}\right)$

$$p(\xi) = \begin{cases} \Gamma(\gamma)\delta(\zeta) & [\text{for} \quad \zeta = 0] \\ 0 & [\text{for} \quad 0 < \zeta < \gamma] \\ (\zeta - \gamma)\exp\left(-\frac{1}{2}(\zeta - \gamma)^2 - \gamma\zeta_c\right) & [\text{for} \quad \gamma < \zeta < \zeta_c + \gamma] \\ \zeta_c \exp\left(-\frac{1}{2}\zeta_c(2\zeta - \zeta_c)\right) & [\text{for} \quad \zeta \geq \zeta_c + \gamma] \end{cases} \quad (7.17)$$

where, $\Gamma(x) = 1 - \exp\left(-\frac{x^2}{2}\right)$ (gamma function), $\gamma = \frac{b^2}{2\zeta_c}$

The probability model for maxima of Morison force in a wide band wave spectrum deviating from the narrow band assumption, in which the spectral density is not concentrated at one frequency, has also been studied. However, it is difficult to develop a complete form of

expression and approximate forms were investigated [Tung (1974), Tickell (1977) and Moe & Crandall (1978)].

7.3. Linearization coefficients in fully and intermittently submerged members

7.3.1. Coefficients for fully submerged member

To approximate the spectral density of the Morison force, the linearization coefficients was first proposed by Borgman (1967). The Borgman's coefficient was estimated by minimizing the error between nonlinear and linearized Morison force during entire time span. A least-square method was applied to minimize the error and the coefficient ($\bar{K}_d$) was derived by Eq. (7.18).

$$\frac{\partial\langle(F-F_l)^2\rangle}{\partial\bar{K}_d} = -2\langle K_d u^2|u| - \bar{K}_d u^2\rangle = 0 \rightarrow \quad \bar{K}_d = K_d\frac{\langle u^2|u|\rangle}{\langle u^2\rangle} \qquad (7.18)$$

Based on the linear wave theory, in the fully submerged section, the particle velocity u follows the Gaussian process of zero mean, so the second and third moments of u are σ_u^2 and $\sqrt{(8/\pi)}\sigma_u^3$ respectively. Therefore, the Borgman's coefficient for fully submerged condition could be derived by substituting statistical moments in Eq. (7.18). That is, the Borgman's coefficient as shown in Eq. (7.19) is only

proportional to the standard deviation of the particle velocity (σ_u) at that location and the other variables do not affect the coefficients.

$$K_d\beta = K_d \frac{\sqrt{(8/\pi)}\sigma_u^3}{\sigma_u^2} = K_d \sqrt{\frac{8}{\pi}}\sigma_u \tag{7.19}$$

Brouwers & Verbeek (1983) compared fatigue damages calculated by nonlinear and linearized Morison's equations by Borgman, respectively. When the ratio of drag force to inertia force (K) is small, which means that inertia force is dominant, linearized force could predict well the fatigue damage calculated by the nonlinear force but it was found that linearized force tend to underestimate fatigue damages in region where drag force is not negligible. They also pointed out that the error increases as the slope of S-N curve increases. Because Borgman's coefficient is calculated by minimizing the time average of error between nonlinear and linear Morison force, it may underestimate the value of peak forces deviated largely from the mean value.

The limitations of Borgman's coefficient were reviewed and an alternative approach to linearize Morison's equation for a narrow-band wave was proposed by Wolfram (1999). The important responses such as extreme responses and fatigue damage are related to the force maxima, not force itself. Thus, the approach was to match the expectation values of the force maxima of the nonlinear and linearized Morison force. Because expectation value is defined as integrating the product of probability density function and random

variable in the whole region, the expectation value of force maxima in complete Morison' s equation is calculated by integrating the product of Eq. (7.14) and the probability density function of the amplitude of particle velocity ($p(u_0)$) as Eq. (7.20). Because the Wolfram' s coefficient was derived just below the free surface, $G(z)$ in Eq. (7.14) was taken as 1 in his work.

$$E[F_P] = \int_0^{\frac{\sigma_u}{2K}} p(u_0)[u_0\omega_{m\,v}K_m]\,du_0 + \int_{\frac{\sigma_u}{2K}}^{\infty} p(u_0)\left[u_0^2K_d + \frac{K_m^2\omega_{m\,v}^2}{4K_d}\right]du_0$$

$$= \omega_{m\,v}K_m\int_0^{\frac{\sigma_u}{2K}} p(u_0)u_0\,du_0 + K_d\int_{\frac{\sigma_u}{2K}}^{\infty} p(u_0)u_0^2\,du_0 +$$

$$\frac{K_m^2\omega_{m\,v}^2}{4K_d}\int_{\frac{\sigma_u}{2K}}^{\infty} p(u_0)\,du_0 \quad (7.20)$$

where, $\omega_{m\,v}$: the mean zero-up crossing frequency of velocity

In LRWT, the particle velocity at a fully submerged point is assumed to be zero-mean Gaussian process, thus, the amplitude of particle velocity follows the Rayleigh distribution. After substituting the Rayleigh distribution and integrating three terms in Eq. (7.20), the expectation value is expressed as Eq. (7.21).

$$E[F_P] = K_d\sigma_u^2\left[\exp\left(-\frac{1}{8K^2}\right)\left(\frac{1}{4K^2}+2\right) + \frac{1}{K}\sqrt{\frac{\pi}{2}}\,erf\left(\frac{1}{2\sqrt{2}K}\right)\right] \quad (7.21)$$

As for the expectation value in linearized Morison' s equation, the value of peak force could be obtained by differentiating Eq. (7.10) respect to time and equating it to zero

$$F_{Pl} = u_0\sqrt{\overline{K}_d^2 + K_m^2\omega^2} \tag{7.22}$$

Therefore, the expectation value of force maxima in linearized Morison' s equation is derived as Eq. (7.23).

$$E[F_{Pl}] = \int_0^\infty f(u_0)\left[u_0\sqrt{\overline{K}_d^2 + K_m^2\omega_{m\,v}^2}\right]du_0 = \sigma_u\sqrt{\frac{\pi}{2}}\sqrt{\overline{K}_d^2 + K_m^2\omega_{m\,v}^2} \tag{7.23}$$

Finally, the linearization coefficient that make the force maxima equal in the complete and linearized Morison' s equations can be obtained by comparing Eqs. (7.21) and (7.23), which can be summarized as Eq. (7.24).

$$\overline{K}_d = K_d\sigma_u\sqrt{\left\{\frac{2}{\pi}\left(\exp\left(-\frac{1}{8K^2}\right)\left(\frac{1}{4K^2}+2\right)+\frac{1}{K}\sqrt{\frac{\pi}{2}}\,\mathrm{erf}\left(\frac{1}{2\sqrt{2}K}\right)\right)^2-\frac{1}{K^2}\right\}}$$

$$= K_d\beta = K_d\sigma_u C^{(1)}(K) \tag{7.24}$$

where, $C^{(m)}(K) = \frac{\beta}{\sigma_u}$

In case of fatigue damage, it is proportional to m−th power of stress range, not stress range. Therefore, linearization coefficient to match fatigue damages calculated by nonlinear and linear drag force should be calculated by equating the expectation values of m−th power of force maxima. Wolfram (1999) also derived linearization

factor considering this fact and the generalized linearization coefficient was expressed in his work.

7.3.2. Coefficients for intermittently submerged member

Unlike the fully submerged case, the particle velocity and acceleration in the intermittent flow no longer follow the Gaussian process. Therefore, it is necessary to propose a new linearization coefficient through the probability distribution model considering the intermittent effect in vicinity of near free surface. In this study, the linearization coefficient near the free surface is derived by using the probability distribution model of force maxima and particle velocity in the intermittent flow proposed by Tung (1975) and Isaacson and Baldwin (1990b). This coefficient is estimated by equating the expectation values of force maxima for nonlinear and linearized Morison' s equation. As mentioned above, when deriving the expectation value for the force maxima in the intermittent flow, there are two differences with fully submerged case: the probability density function of amplitude of the particle velocity$(p(u_0'))$ and the expectation value of force maxima(F_P'). From Eq. (7.5) which indicates the probability density function of particle velocity in intermittent flow proposed by Tung (1975), it is possible to derive the probability function of velocity amplitude as Eq. (7.25).

$$p(u_0') = [1 - Q(b)]\delta(u_0') + \frac{u_0'}{\sigma_u^2}\exp\left(-\frac{u_0'^2}{2\sigma_u^2}\right)Q\left(\frac{b-\frac{ru_0'}{\sigma_u}}{\sqrt{1-r^2}}\right) \qquad (7.25)$$

The value of force maxima expressed in Eq. (7.16) could be rewritten as a function of velocity amplitude as Eq. (7.26). In deep water, $G(z)$ is assumed to be 1 near the free surface where z approaches to zero.

$$F_P'(h) = \begin{cases} 0 \quad [\text{for} \quad u_0' < \omega h] \\ \omega^2 K_d h^2 + \omega K_m \sqrt{u_0'^2 - \omega^2 h^2} \quad \left[\text{for } \omega h < u_0' < \sqrt{\frac{\sigma_u^2}{4K^2} + \omega^2 h^2}\right] \\ u_0'^2 K_d + \frac{K_m^2 \omega^2}{4K_d} \quad \left[\text{for} \quad \sqrt{\frac{\sigma_u^2}{4K^2} + \omega^2 h^2} \le u_0'\right] \end{cases} \qquad (7.26)$$

The expectation value of force maxima in intermittent flow is derived from Eq. (7.25) and (7.26). In order to reflect the effect of m which is the slope of S-N curve on the linearization coefficient, the expectation value for m-th order of force maxima is derived. In case of the complete Morison' s equation in a narrow-band wave spectrum, the expectation value is expressed as Eq. (7.27).

$$E\left[F_P'^m(h)\right] = \int_{\omega_{m\,v}h}^{\sqrt{\frac{\sigma_u^2}{4K^2}+\omega_{m\,v}^2 h^2}} p(u_0')[F_A]^m du_0' + \int_{\sqrt{\frac{\sigma_u^2}{4K^2}+\omega_{m\,v}^2 h^2}}^{\infty} p(u_0')[F_B]^m du_0' \quad (7.27)$$

where, $F_A = \omega_{m\,v}^2 K_d h^2 + \omega_{m\,v} K_m \sqrt{u_0'^2 - \omega_{m\,v}^2 h^2}$

$$F_B = u_0'^2 K_d + \frac{K_m^2 \omega_{m\,v}^2}{4K_d}$$

The two integral terms (F_A^m,F_B^m) are expanded as Eq. (7.28) and (7.29) by binomial theorem.

$$F_A^m = \sum_{p=0}^{m} C_{(m,p)} \left(\omega_{m\,v} K_m \sqrt{u_0'^2 - \omega_{m\,v}^2 h^2} \right)^p (\omega_{m\,v}^2 K_d h^2)^{m-p}$$

$$= \sum_{p=0}^{m} C_{(m,p)}\, K_m^p \omega_{m\,v}^{2m-p} \left(u_0'^2 - \omega_{m\,v}^2 h^2\right)^{p/2} K_d^{m-p} h^{2m-2p} \qquad (7.28)$$

where, $C_{(m,p)}$: $\frac{m!}{(m-p)!p!}$

$$F_B^m = \sum_{p=0}^{m} C_{(m,p)} \left(\frac{K_m^2 \omega_{m\,v}^2}{4K_d} \right)^p \left(u_0'^2 K_d\right)^{m-p}$$

$$= \sum_{p=0}^{m} C_{(m,p)}\, 2^{-2p} K_m^{2p} \omega_{m\,v}^{2p} K_d^{m-2p} u_0'^{2m-2p} \qquad (7.29)$$

By substituting Eq. (7.28) and (7.29) into Eq. (7.27), it can be rewritten as sum of Eq. (7.30) and (7.31).

$$\sum_{p=0}^{m} C_{(m,p)}\, K_m^p \omega_{m\,v}^{2m-p} K_d^{m-p} h^{2m-2p}$$

$$\times \int_{\omega_{m\,v} h}^{\sqrt{\frac{\sigma_u^2}{4K^2} + \omega_{m\,v}^2 h^2}} p(u_0') \left(u_0'^2 - \omega_{m\,v}^2 h^2\right)^{p/2} du_0' \quad (7.30)$$

$$\sum_{p=0}^{m} C_{(m,p)}\, 2^{-2p} K_m^{2p} \omega_m^{2p} K_d^{m-2p} \int_{\sqrt{\frac{\sigma_u^2}{4K^2}+\omega_m^2 h^2}}^{\infty} p(u_0') u_0'^{2m-2p} du_0' \qquad (7.31)$$

Two integral terms in Eq. (7.30) and (7.31) are not be possible to express explicit forms so they should be evaluated through a numerical method.

In linearized Morison' s equation as Eq. (7.10), the values of force maxima in intermittent flow are derived from Eq. (7.26). The phase angle (θ_m) at which the peak of continuous force occurs in the linearized Morison force could be evaluated by differentiating Eq. (7.10) with respect to time and be expressed as Eq. (7.32).

$$\frac{\partial F_l}{\partial \mathrm{t}} = -u_0\omega(\bar{K}_d \sin\theta_m + K_m\omega\cos\theta_m) = 0 \rightarrow \quad \theta_m = -\tan^{-1}\left(\frac{K_m\omega}{\bar{K}_d}\right) \quad (7.32)$$

The phase angle (θ_m) in Eq. (32) is expressed as a function of linearization coefficient ($\bar{K}_d$). Since this is related to continuous force, it could be assumed that it is equal to the Wolfram' s coefficient (Eq. (7.24)) derived from fully submerged condition. By substituting Eq. (7.24) to Eq. (7.32), the θ_m of linearized Morison force could be expressed as Eq. (7.33).

$$\theta_m = -\tan^{-1}\left(\frac{K_m\omega}{\bar{K}_d}\right) = -\tan^{-1}\left(\frac{K_m\omega}{K_d\sigma_u C_w}\right) = -\tan^{-1}\left(\frac{1}{C_w K}\right) \qquad (7.33)$$

where, C_w : Wolfram' s coefficient (m=1)

By comparing θ_m and θ_0, the peak values of linearized Morison force in intermittent flow at h is derived as Eq. (7.34)

$$F'_{Pl}(h) = \begin{cases} 0 \quad [for \quad u'_0 < \omega h] \\ \omega \bar{K}_d h + \omega G(z) K_m \sqrt{u_0'^2 - \omega^2 h^2} \quad \left[for \quad \omega h < u'_0 < \omega h \sqrt{\frac{1}{C_w^2 K^2} + 1} \right] \\ u'_0 \sqrt{\bar{K}_d^2 + K_m^2 \omega^2} \quad \left[for \quad \omega h \sqrt{\frac{1}{C_w^2 K^2} + 1} \le u'_0 \right] \end{cases} \quad (7.34)$$

The expectation value for mth order of force maxima in linearized Morison force for a narrow−band wave spectrum could be derived as the same manner.

$$E\left[F_{Pl}'^{m}(h)\right] = \int_{\omega_{m\,v} h}^{\omega_{m\,v} h \sqrt{\frac{1}{C_w^2 K^2}+1}} p(u'_0)[F_C]^m du'_0 + \int_{\omega_{m\,v} h \sqrt{\frac{1}{C_w^2 K^2}+1}}^{\infty} p(u'_0)[F_D\ \ ]^m du'_0 \quad (7.35)$$

where, $F_C = \omega_{m\,v} \bar{K}_d h + \omega_{m\,v} K_m \sqrt{u_0'^2 - \omega_{m\,v}^2 h^2}$, $F_D = u'_0 \sqrt{\bar{K}_d^2 + K_m^2 \omega_{m\,v}^2}$

The two integral terms (F_C^m,F_D^m) are expanded as Eq. (7.36) and (7.37) by binomial theorem.

$$F_C^m = \sum_{p=0}^{m} C_{(m,p)} \left(\omega_{m\,v} K_m \sqrt{u_0'^2 - \omega_{m\,v}^2 h^2} \right)^p (\omega_{m\,v} \bar{K}_d h)^{m-p}$$

$$= \sum_{p=0}^{m} C_{(m,p)}\, K_m^p \omega_{m\,v}^m \bar{K}_d^{m-p} h^{m-p} \left(u_0'^2 - \omega_{m\,v}^2 h^2\right)^{p/2} \qquad (7.36)$$

$$F_D^m = \left(\bar{K}_d^2 + K_m^2 \omega_{m\,v}^2\right)^{m/2} u_0'^m \qquad (7.37)$$

By substituting Eq. (7.36) and (7.37) into Eq. (7.35), it can be rewritten as sum of Eq. (7.38) and (7.39).

$$\sum_{p=0}^{m} C_{(m,p)}\, K_m^p \omega_{m\,v}^m K_d^{m-p} \sigma_u^{m-p} C^{m-p} h^{m-p} \times \int_{\omega_{m\,v} h}^{\omega_{m\,v} h \sqrt{\frac{1}{C_w^2 K^2}+1}} p(u_0')\left(u_0'^2 - \omega_{m\,v}^2 h^2\right)^{p/2} du_0' \qquad (7.38)$$

$$K_d^m \sigma_u^m \left(C^2 + \frac{1}{K^2}\right)^{m/2} \int_{\omega_{m\,v} h \sqrt{\frac{1}{C_w^2 K^2}+1}}^{\infty} p(u_0')\, u_0'^m \; du_0' \qquad (7.39)$$

C in Eq. (7.38) and (7.39) was defined in Wolfram' s work as a function of K and m but observation height h is added as an input factor for C in this present work. The expectation value for m−th order of force maxima in linearized Morison' s equation can be expressed as a summation of Eq. (7.38) and (7.39) and the integral terms should be evaluated by numerical integration. Because C is defined as the value that makes both expectation values of nonlinear and linearized drag force, C could be evaluated by comparing Eq (7.27) and (7.35). Finally, C is expressed as a function of K, m and h as shown in Eq. (7.40).

$$\bar{K}_d = C^{(m)}(K,h)K_d\sigma_u \tag{7.40}$$

Finally, the linearization coefficient ($C^{(m)}(K,h)$) in intermittent flow could be calculated by equating the expectation values in nonlinear and linearized Morison' s equations. Fig. 88 shows linearization coefficients with the ratio of drag force to inertia force (K) at different observation heights (h). Since the influence of the drag is small in a small region of K ($K < 0.2$), the linearization coefficients are also small in that region. As K increases, the linearization coefficients increase and then converge to a specific value like Wolfram' s coefficient. The converged value (1.654) is similar to Wolfram coefficient, 1.595 when observation height is small. In the intermittent flow, the observed height (h) also have an impact on the linearization coefficient. As shown in Fig. 88, the proposed linearization coefficient increases as observation height (h) increases. As the observation position increases, the number of waves reaching it decreases, whereas the all-arriving wave have high wave amplitudes. Because the amplitude of particle velocity has a linear relationship with wave amplitude, the amplitude of velocity should be large when the wave amplitude is large. This tendency is reflected in the proposed linearization coefficient, and it can be interpreted that the linearization coefficient increases with the increase in the observation position.

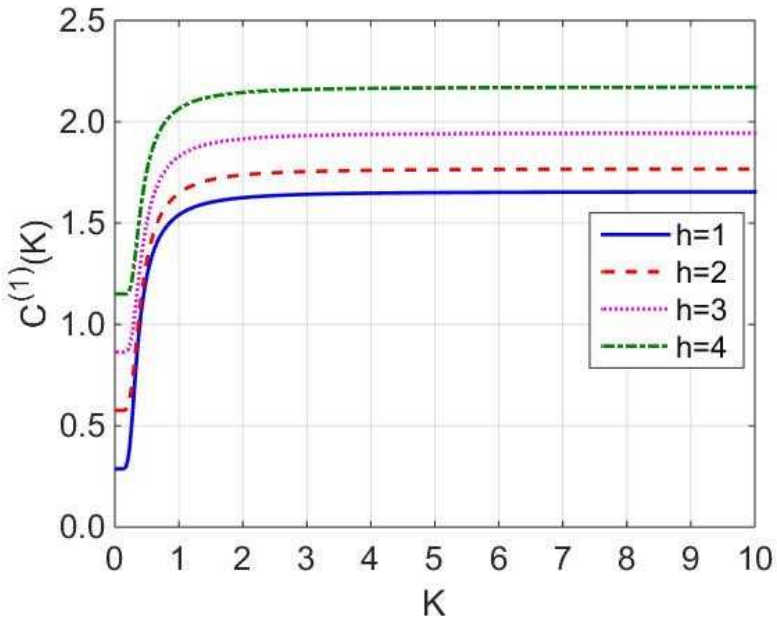

Fig. 88 The linearization coefficients in intermittent flow with different observation heights (m=1)

The linearization coefficients with different m values are also compared to evaluate the effect of the slope of S-N curve in the coefficient. As mentioned in the study of Brouwers & Verbeek (1983), the Borgman approximation underestimates the fatigue damage and the error increases as the slope of S-N curve increases. The proposed coefficient is also considered the effect of the slope of S-N curve like Wolfram' s work. As seen in Fig. 89, the linearization coefficient increases as m increases although all three lines are calculated at the same height.

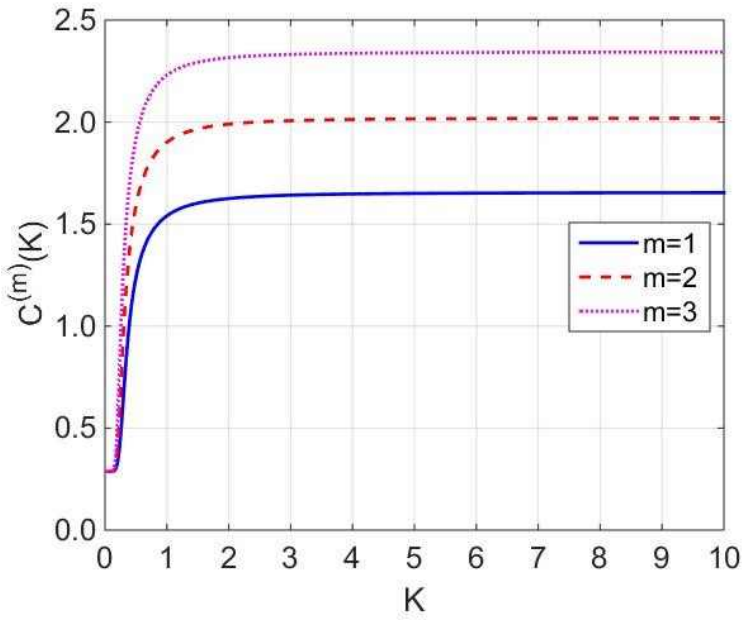

Fig. 89 The linearization coefficients in intermittent flow with different the slope of S−N curve (h=1)

7.4. Numerical simulations

7.4.1. Procedure of simulation

Fatigue damages are estimated by three different methods as summarized below.

1. Time domain method with RFC (D1)
2. Frequency domain method with linearization coefficient (D2)
3. Frequency domain method with two approximate models (D3)

The difference between the 2nd and 3rd methods is the way to obtain power spectral density of hot spot stress. In the 3rd method, hot spot stress spectrum is calculated from the time history of hot spot stress. It means that the 3rd method depends on time simulation results to estimate corresponding power spectral density. However, in the 2nd model, hot spot stress spectrum can be directly in frequency domain without time simulation data because non-linearity of Morison force is linearized through the proposed coefficients.

As shown in Fig. 87, time simulations are performed to calculate the hot spot stress located at bottom of the fixed cylinder. The cylinder is modeled as beam elements as shown in Fig. 90. The first step is calculating particle velocity and acceleration at center of each element. As explained in Eq. (7.3) and (7.4), particle velocity and acceleration are estimated through linear random wave theory and linear intermittent random wave theory depending on the relationship between surface elevation and z-coordinate of center of each element.

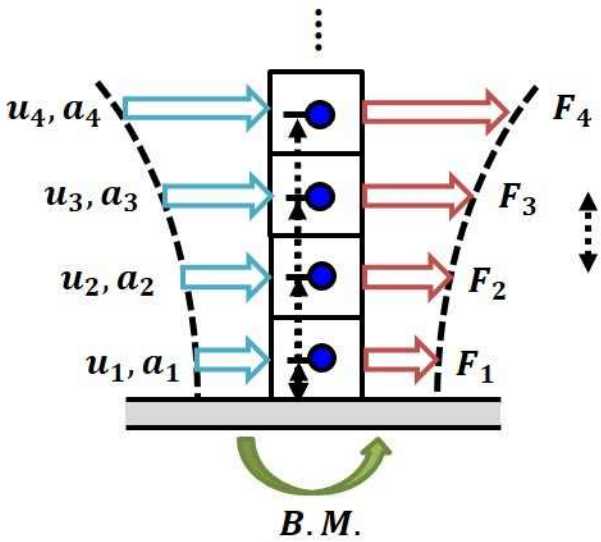

Fig. 90 Description of hot spot stress calculation through time simulation

The next step is calculating corresponding Morison force at each element. Non-linear Morison equation is used in time simulation and the element length should be considered when total Morison force at each element is evaluated. Bending moment at bottom induced by Morison force can be obtained by multiplying non-linear Morison force at each element and distances between bottom and centers of each element as shown in Eq. (7.41).

$$B.M.(t) = \sum_{i=1}^{n} F_i(t) \times l_i \tag{7.41}$$

where, $B.M.(t)$: Bending moment at bottom

n : number of elements

$F_i(t)$: Morison force acting at center of ith element

l_i : distance between bottom and center of ith element

Finally, hot spot stress can be evaluated by simple beam theory as shown in Eq. (7.42). The corresponding power spectral density of hot spot stress can be obtained through Wiener−Khinchin transformation explained in Eq. (3.2).

$$\sigma(t) = \frac{B.M.(t)y}{I} \tag{7.42}$$

where, $\sigma(t)$: hot spot stress, I: sectional moment of inertia

y: radius of cylinder

As mentioned above, hot spot stress spectrum is directly calculated in frequency domain in the 2nd model (D2). The Morison force spectral density explained in Eq. (7.11) and (7.13) can be easily evaluated by inputting the information of wave spectrum, some constants for Morison equation and linearization coefficient. Real and imaginary parts of Morison force spectral densities at each element should be classified to calculate bending moment spectrum that consists of summation on multiplication of force spectra with distance between bottom and center of each element as describe in Eq. (7.43).

$$S_{B.M.}(\omega) = \left[\sum_{i=1}^{n} \sqrt{S_{F_i}^{\text{real}}(\omega)} \times l_i\right]^2 + \left[\sum_{i=1}^{n} \sqrt{S_{F_i}^{\text{im ag}}(\omega)} \times l_i\right]^2 \tag{7.43}$$

where, $S_{B.M.}(\omega)$: Bending moment spectrum

$S_{F_i}^{\text{real}}(\omega)$: Real part of force spectrum (drag term)

$S_{F_i}^{\text{im ag}}(\omega)$: Imaginary part of force spectrum (inertia term)

Finally, power spectral density of hot spot stress can be obtained from Eq. (7.44).

$$S_{\sigma}(\omega) = \left(\frac{y}{I}\right)^2 \times S_{B.M.}(\omega) \tag{7.44}$$

Until now, the detail procedure of getting hot spot stress spectrum using linearization coefficient in the 2nd model (D2) is explained. The corresponding fatigue damage can be obtained by various approximate models such as the BT model. However, the non−normality properties represented by skewness and kurtosis are not reflected in this method because non−linear drag term is linearized in this approach using linearization coefficient. In short, the skewness and kurtosis of linearized Morison force must be always close to that of Gaussian processes. This fact causes a large error in assessment on fatigue damage. Thus, we introduce additional correction factor for reflecting the effect of non−normality on fatigue damage proposed by Winterstein (1988) as shown in Eq. (7.45).

$$\lambda_{nG}^{W}(\gamma_4, m) = 1 + \frac{m(m-1)(\gamma_4 - 3)}{24} \tag{7.45}$$

where, λ_{nG}^{W}: correction factor for non−normality (Winterstein)

γ_4: kurtosis, m: the slope of S−N curve

Finally, the corrected fatigue damages in the 2nd model is obtained by multiplying the correction factor in Eq. (7.45).

$$D_2^{nG} = \lambda_{nG}^{W} \times D_2^{G} \tag{7.46}$$

where, D_2^{nG}: fatigue damage considering non−normal effect in D2

D_2^{G}: fatigue damage calculated from Eq. (7.44)

7.4.2. Information of simulation

Simple configuration described in Fig. 91 is used in this time simulation. The detail information of some constants used in simulation is summarized in Table 11.

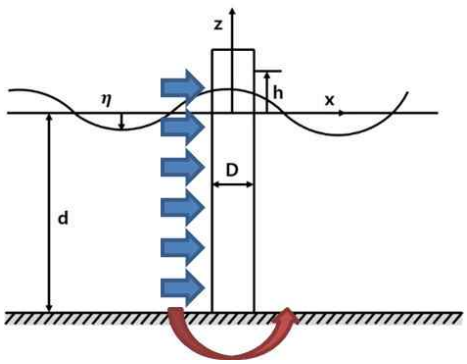

Fig. 91 Definition of coordinate system and variables

Table 11 Information of simulation constants

Water depth [m] (d)	300
Diameter of cylinder [m] (D)	1
Observation location [m] (h)	$0.5 \sim 3\sigma_\eta$ ($0.5\sigma_\eta$ step)
Simulation length [s]	10,800
Time step [s]	0.2

The coefficient of drag force (C_D)	1.4
The coefficient of inertia force (C_m)	2

The cylinder is modelled into total 36 number of beam elements. Below the free surface, the length of element is taken as 10 meters so total 30 number of beam elements are located in this region. Additional 6 elements located above the free surface are modelled to reflect the intermittent effect of Morison force in simulations. Vertical stretching method is applied to calculate particle velocity and acceleration observed in these elements.

The JONSWAP wave spectrum is used and total 10 number of sea states are selected within reasonable region for JONSWAP spectrum as summarized in Table 12.

Table 12 The information of sea state

Sea state condition (10 sea states) $\left[\boldsymbol{3.6 < T_p/\sqrt{H_s} < 5}\right]$	
(H_s, T_p)	(5,9), (5,11), (7,10), (7,12), (9,11), (9,14), (11,13), (11,16), (13,14), (13,17)

7.4.3. Results

The 1st and 2nd bandwidth parameters of simulated hot spot stresses are summarized in Fig. 92. The hot spot stresses in Morison force examples are close to narrow-banded process due to JONSWAP wave spectrum.

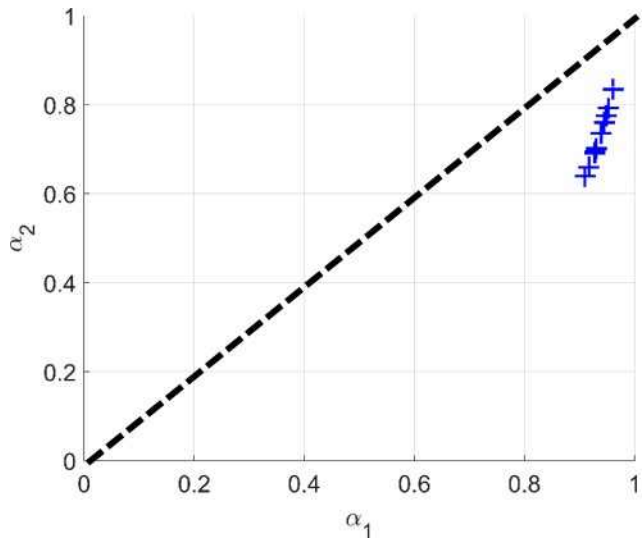

Fig. 92 Scatter plot of the 1st and 2nd bandwidth parameters of hot spot stresses in all sea states

The skewness and kurtosis values of hot spot stresses are summarized in Fig. 93 As we expect, the non-normality of hot spot stress increases when significant wave height is high. The intermittent effect also has a large effect on the non-normality of hot spot stress.

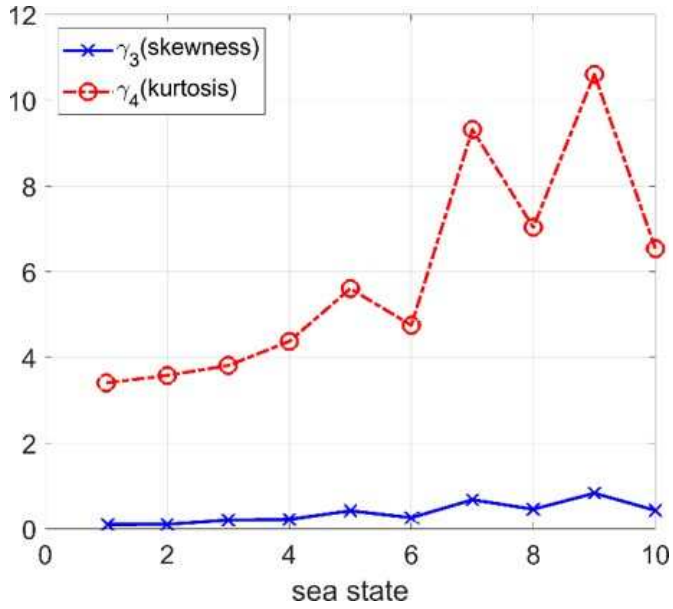

Fig. 93 Skewness and kurtosis of hot spot stresses

Two examples of hot spot stresses calculated from time simulation (D1 and D3) and frequency domain through the linearization (D2) are compared in Fig. 94. Although, slight differences are observed at peak frequency between two stress spectra, the power spectral density obtained through linearization seems to give a good agreement on the results of time simulation that considers non-linear drag term in Morison equation.

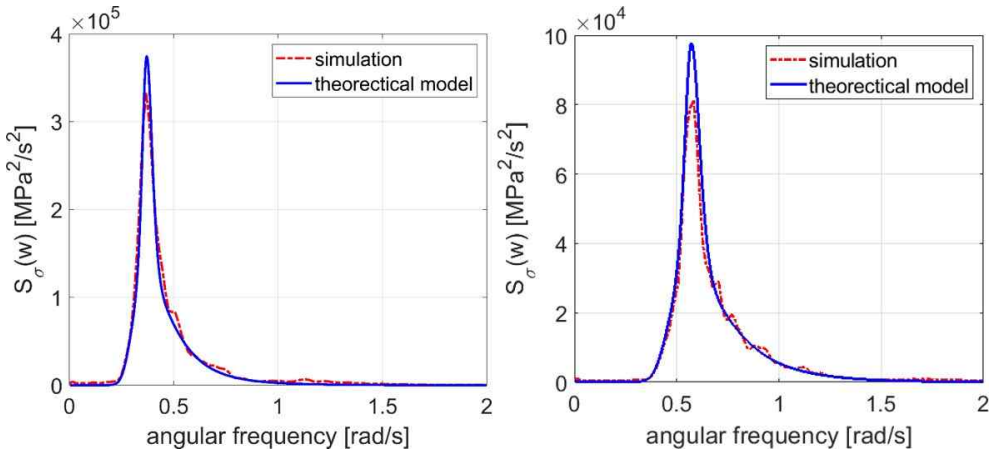

Fig. 94 Comparison between stress spectra obtained from time simulation (red dash line) and frequency domain through linearization (blue solid line) in two sea states: (Hs, Tp) = (9m, 11s) (left); (Hs, Tp) = (13m, 17s) (right)

Finally, the absolute value of errors of D2 and D3 compared to D1 are plotted in Fig. 95. In mildly non-Gaussian processes whose kurtosis values are close to 3, there is no significant difference between errors of three models. From the 7th sea state where the kurtosis value increases sharply, the BT model shows considerable errors in estimating fatigue damages. On the other hand, the proposed model expressed as blue bar in Fig. 95 gives the most accurate results among three models. The errors of D2 that utilizes hot spot stress spectra obtained from fully frequency domain method through linearization coefficient give accurate results until the 6th sea state. However, it tends to give large errors in severe sea condition where hot spot stresses are strongly non-Gaussian processes.

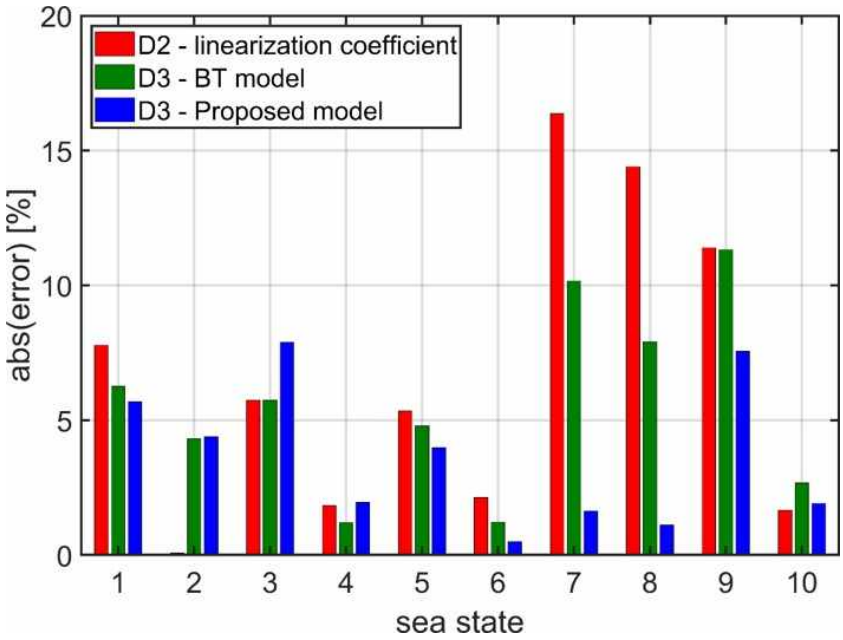

Fig. 95 The errors of three models in all load cases

7.5. Convergence problems in frequency domain approach

Although two time simulations are performed in the same condition, two time history data from these simulations, called $X_1(t), X_2(t)$, must not be exactly same due to inherent uncertainties. Thus, estimated fatigue damages from $X_1(t), X_2(t)$ are also different. On the other hands, statistical properties of them are the same theoretically based on the assumption that they are stationary ergodic processes. The spectral representations of them, $S_{X_1}(\omega), S_{X_2}(\omega)$, are identical theoretically. Thus, fatigue damages of them estimated by frequency domain approach that utilizes power spectral density of random processes are exactly same.

However, spectral representations obtained from time histories

are not exactly same in actual practice. When structural responses are close to Gaussian processes, differences between power spectral densities calculated from different simulation is not significant. On the other hands, in non-Gaussian problems, the differences seem to be considerable so estimated fatigue damages through frequency domain approach also varies depending on simulation results. In short, power spectral densities are different each other and the estimated fatigue damages can be unstable especially in wide-banded non-Gaussian problem.

In this chapter, convergence rates of estimated fatigue damages through time and frequency domain methods are compared to verify the efficiency of frequency domain method. The convergence tests are performed in wide-banded Gaussian and non-Gaussian examples.

7.5.1. Convergence test in Gaussian processes

Power spectral densities of random processes are basically estimated from time history of random processes through Wiener-Khinchin transformation as described in Eq. (3.2). The other method for obtaining power spectral densities is using a transfer function. Transfer function ($\Phi(\omega)$) is a relationship between spectral representations of input ($X(t)$) and output ($Y(t)$) random processes. It consists of real and imaginary part as shown in Eq. (7.47).

$$\Phi(\omega) = A(\omega) - B\ (\omega) \tag{7.47}$$

where, $A(\omega), B(\omega)$: real and imaginary parts of transfer function

Then, the magnitude of $\Phi(\omega)$, which is called response amplitude operator (RAO), is defined as in Eq. (7.48).

$$H_{X\to Y}(\omega) = |\Phi(\omega)| = \sqrt{A^2(\omega) + B^2(\omega)} \tag{7.48}$$

where, $H_{X\to Y}(\omega)$: RAO between $X(t)$ and $Y(t)$

From its definition, power spectral density of output random variable $Y(t)$ could be obtained by multiplying power spectral density of input random process $X(t)$ and the square of RAO as shown in Eq. (7.49).

$$S_Y(\omega) = S_X(\omega) \times |H_{X\to Y}(\omega)|^2 \tag{7.48}$$

The transfer function $\Phi(\omega)$ can only be defined when the relationship between input and output is linear. Transfer function between loadings and structural responses can be defined for most Gaussian processes in offshore engineering problems. In short, hot spot stress spectrum could be calculated by applying stress transfer function and additional time simulations are not needed in Gaussian problems.

The idealized stress spectra described in Fig. 17 are used to convergence test in Gaussian random processes. Fig. 96 shows estimated fatigue damage rate by time domain method with different

simulation time. It seems that estimated fatigue damage rate converges well within a range of ±3% of the damage rate obtained during 3-hour simulation in very short time. The results of damage rate predictions through time and frequency domain methods with different simulation trials are compared in Fig. 97. Due to inherent uncertainties in simulation, the estimated damage rates vary with different trials but the differences seem to be not significant in Gaussian problems (maximum difference is about 5%). Damage rate is also calculated by Benasciutti & Tovo model for wide-banded Gaussian processes. Because the power spectral density is assumed to be calculated from transfer function, estimated fatigue damages are always same in all trials.

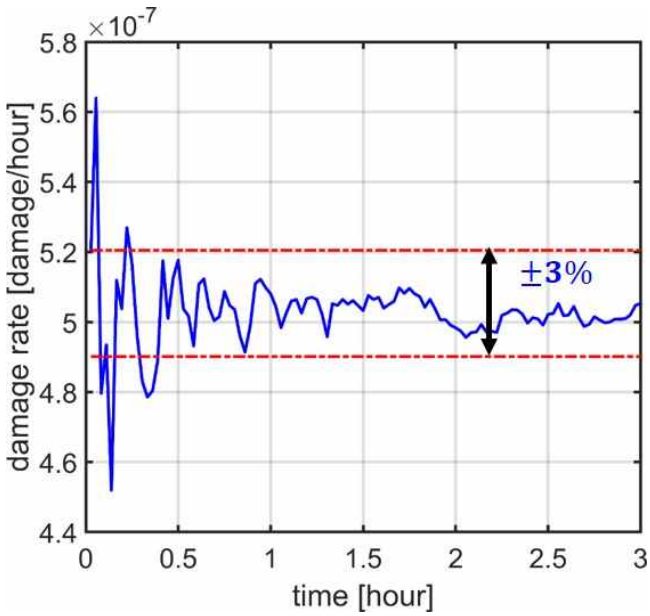

Fig. 96 Estimated damage rates through time domain method with different simulation length [Type 4 – (α_1, α_2) = (0.7, 0.3)]

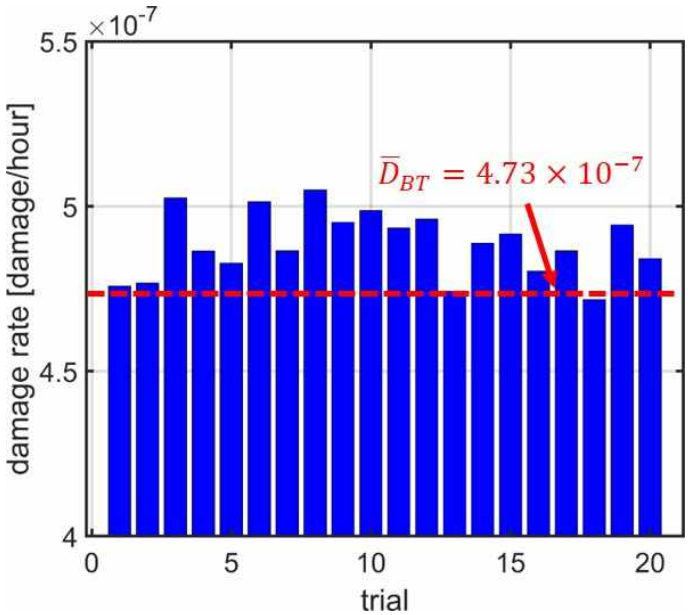

Fig. 97 Estimated damage rates obtained by time and frequency domain method in different trials [Type 4 − (α_1, α_2) = (0.7, 0.3)]

7.5.2. Convergence test in non-Gaussian process

The results of fatigue analysis on fixed cylinder structure under nonlinear Morison loads described in Chapter 7 are used to converge test in non−Gaussian processes. Unlike Gaussian problems, non−Gaussian properties of random processes are mostly related to non−linearities of random loadings. Due to these non−linearities, time domain approach requires a larger amount of simulation length to get stable results than in Gaussian problems. Fig. 98 shows estimated fatigue damage rate by time domain method in the 9th sea state with different simulation time. It seems that estimated fatigue damage rate

hardly converges within a range of ±3% of the damage rate obtained during 3-hour simulation.

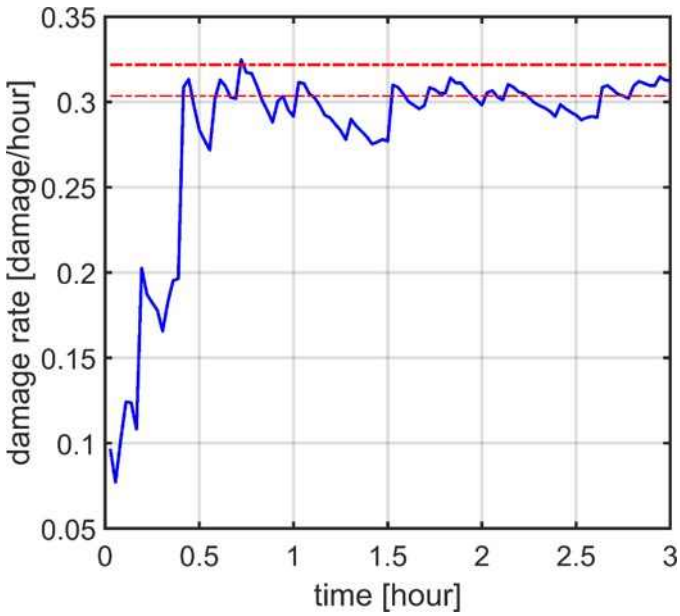

Fig. 98 Estimated damage rates through time domain method with different simulation length [(Hs, Tp) = (13m, 14s)]

To check stability of time domain method, time simulations are repeated 20th times in the same sea condition. The results of damage rate predictions through time domain method with different simulation trials are compared in Fig. 99. It seems that time domain results show large deviations each other even though they are performed in the same condition. Maximum difference is about 40%.

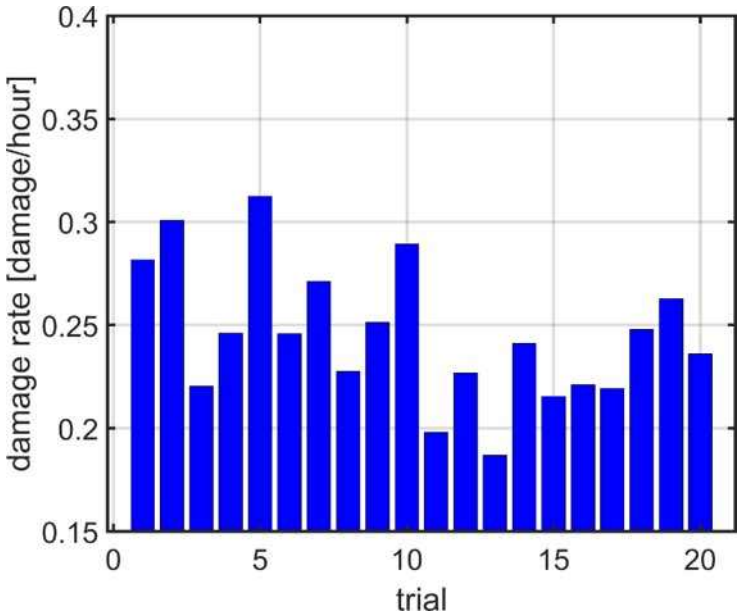

Fig. 99 Estimated damage rates obtained by time domain method in different trials [(Hs, Tp) = (13m, 14s)]

Unlike fatigue analyses for Gaussian random processes, transfer function can not be difined due to nonlinear properties of random loadings in non-Gaussian problems. In this case, time simulation results should be required to predict the corresponding power spectral estimates. In short, uncertainties in time simulation affects the accuracy of frequency domain method also. Fig. 100 shows four spectral parameters that are input variables of the proposed approximate model for joint probability distribution of mean and amplitude. Red dash lines in Fig. 100 also indicate ±3% range of estimated values from 3-hour simulation.

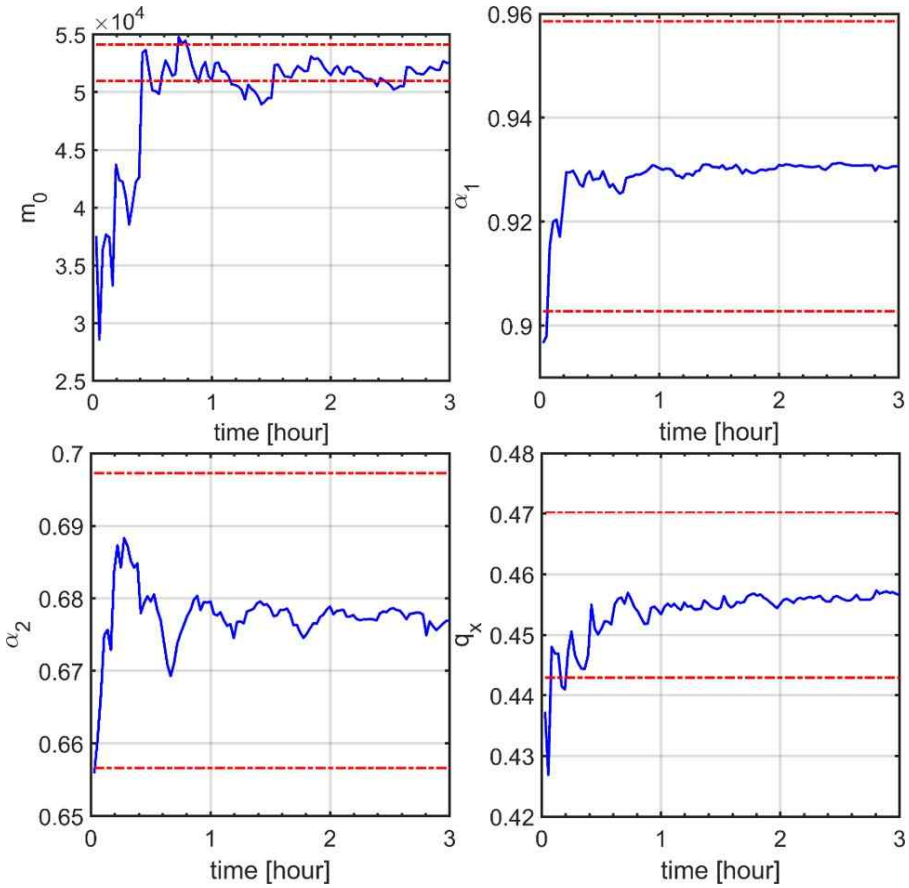

Fig. 100 Estimated spectral parameters with different simulation length [(Hs, Tp) = (13m, 14s)]

Three spectral parameters except the 0th spectral moment seem to converge well in very short simulation length even through hot spot stress follows non-Gaussian process. However, it seems that the 0th spectral moment hardly converges like estimated damage rates through time domain approach.

Fig. 101 gives the estimated damage rate through frequency domain method with different simulation length and trials. For non-Gaussian problems, the frequency domain method can also give unstable results like time domain methods because estimated

spectral density depends on time simulation results. Thus, frequency domain method also requires a large amount of simulation length to get stable power spectral densities estimate in this non-Gaussian examples.

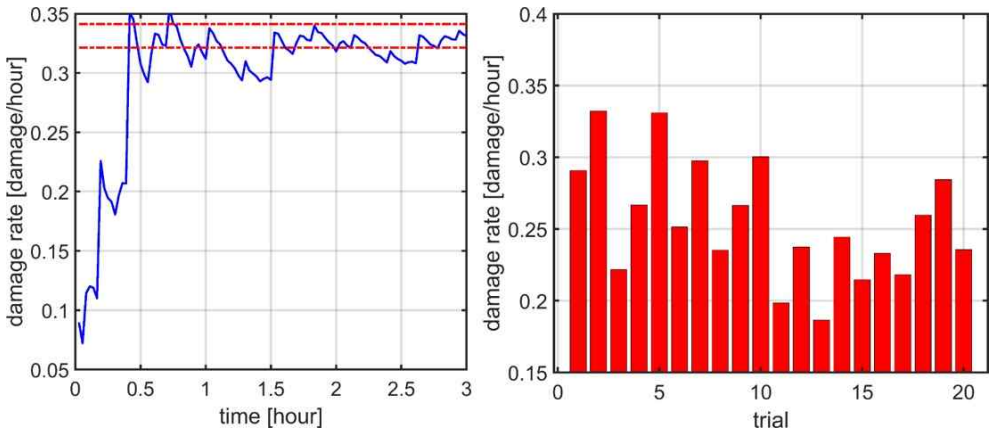

Fig. 101 Estimated damage rates with different simulation length (left) and different trials (right) through frequency domain method [(Hs, Tp) = (13m, 14s)]

In conclusion, additional methods should be required to enhance efficiency and stability of frequency domain method for non-Gaussian problems. In chapter 7.4, hot spot stress spectrum at bottom of fixed cylinder under non-linear Morison load is theoretically derived as Eq. (7.44) by introducing the linearization coefficient. Although it fails to reflect the non-normality of non-linear Morison load, the estimated stress spectrum is very close to the stress spectrum predicted by time simulation considering non-linear Morison load. An example of estimates of stress spectrum in the 9th sea state is given in Fig. 102. Among four input variables

shown in Fig. 100, only the 0th spectral moment tends to hardly converge. Therefore, by using the 0th spectral moment evaluated from the linearized stress spectra, it is expected that the frequency domain method give more stable results. As seen in Fig. 102, the 0th spectral moments estimated from the stress spectra from linearized and non−linear Morison loads seem to be very close.

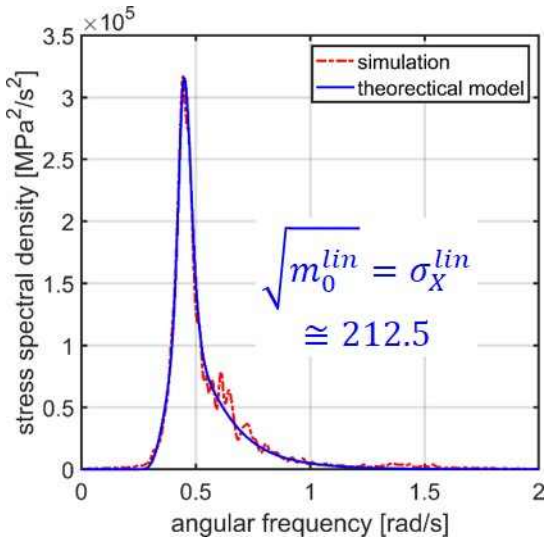

Fig. 102 Hot spot stress spectra predicted by time simulation (blue) and theoretical model with linearization coefficient (red) in the 9th sea state [(Hs, Tp) = (13m, 14s)]

Fig. 103 shows damage rates with different simulation length and trials through the frequency domain method using the information of expected value of the 0th spectral moments from linearized stress spectra. As we expected, it is observed that damage rates converge in very short time and the differences among damage rates from different trial seem to be smaller than the results shown in Fig, 101.

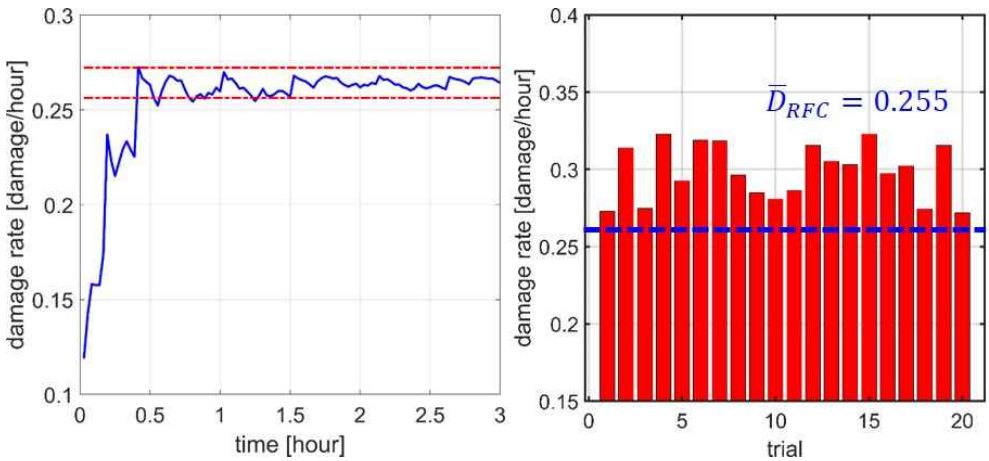

Fig. 103 Estimated damage rates with different simulation length (left) and different trials (right) through frequency domain method using the expected value of the 0th spectral moment from linearization technique [(Hs, Tp) = (13m, 14s)]

Chapter 8. Conclusion

8.1. Summary

This present work aims at modifying approximate model for joint probability distribution of stress mean and amplitude of rainflow-counted cycles.

The BT model ,which have been the most accurate model in evaluating fatigue damages under wide-banded Gaussian processes and could be extend to non-Gaussian problems through proper transformation technique, seems to distort the information of stress mean distribution especially in high amplitude region. It is not a big deal in Gaussian process without mean stress correction however; it has a significant effect on transformation process to non-Gaussian processes.

In this work, the conditional probability density function of stress mean given amplitude is approximated as a simple formula. The conditional PDF of stress mean is assumed as zero-mean Gaussian distribution. Non-linear regression analysis to obtain the approximate model for standard deviation of the normal distribution is performed. Three input variables ($\alpha_1, \alpha_2, q_{\dot{X}}$) are determined and the effects of each variable on the regression model are discussed. Finally, the modified joint probability distribution is defined as a product of marginal distribution of stress amplitude proposed by Benasciutti and Tovo and the proposed conditional probability density

function.

The accuracy of the proposed joint probability distribution is investigated in various case study. In the idealized stress spectra examples, the reason why the BT model tends to underestimate the fatigue damages for hardening non-Gaussian processes and overestimate the fatigue damages for softening non-Gaussian processes is discussed. The proposed model tend to show similar tendency to the BT model but it gives smaller errors in most stress spectra.

Two case studies are introduced to verify the accuracy and efficiency of the proposed model in real engineering problems. First case study is related to ECA on TLP tendon. The entire information of cycle distribution such as joint probability distribution of rainflow-counted cycles is required in crack propagation analysis if the crack closure effect is considered. In this example, the BT model, which concentrates on large probability at zero-mean cycles, seems to overestimate the crack growth rate. On the other hands, the proposed model is observed to give better representation of simulated crack growth rate in most sea state.

The second case study is a fatigue analysis on offshore floating wind turbine supporting structure. This study aims at verifying the performance of the proposed model in dealing with non-Gaussian random processes. However, unlike our expectation, simulated time history of hot spot stresses seem to be close to mild non-Gaussian processes whose kurtosis is near to three. The reason for this is seemed to be the effect of pitch control system. The proposed model

gives also better results than the BT model in estimating fatigue damages for wide-banded non-Gaussian random loadings through this case study.

It is difficult to obtain power spectral density of structural responses in frequency domain when the responses are non-Gaussian processes. In this case, the power spectral density should be estimated from time simulations. It requires additional computational time and cost so investigations for obtaining power spectral densities without time simulation should be performed to enhance the efficiency of frequency domain method for non-Gaussian process. In chapter 7, we derive a linearization coefficient to obtain the force spectral density directly in frequency domain without time simulation. The proposed linearization coefficient is derived including the intermittent effect near free surface. By using this coefficient, the hot spot stress spectrum could be calculated without time simulation and the accuracy of estimated stress spectrum shows very good agreements on simulated results. However, after linearization, the non-normality properties of non-linear Morison force no longer exist. Due to this, large errors could occur in fatigue damage calculation. An alternative method needs to be investigated to obtain skewness and kurtosis of hot spot stress without time simulations.

8.2. Future works

In this work, marginal distribution of stress amplitude is assumed to be given and the BT model is used to construct joint probability distribution of mean and amplitude. However, as discussed in chapter 5, the effect of marginal distribution of stress amplitude on estimation of fatigue damages under non-Gaussian random loading is still significant. Some literatures pointed out that the BT model gives poor representations of estimation on the shape of probabilistic models. Thus, more elaborate model for PDF of stress amplitude should be further investigated to enhance the accuracy of the proposed model for non-Gaussian random processes.

Skewness and kurtosis are important parameters which account for non-normal properties of random processes and theses parameters also have a large effect on fatigue damages. However, in most non-Gaussian problem, skewness and kurtosis values of random process are assumed to be given and additional time simulations are required to obtain the information of these parameters. Some literatures have proposed interesting approaches to reduce computational time and cost or to simplify process for obtaining the behavior of non-Gaussian processes [Braccesi & Cianetti (2011), Cianetti (2012), Annenkov (2014)]. However, these approaches can be applied in limited condition and it depends on still the time simulation to obtain this information.

As for the Morison force example, Najafian (2006) proposed a simple formula to estimate kurtosis and skewness of Morsion force. It seems to give very accurate results but it is limited in fully submerged cases. Additional simulated data should be also required

to extend this formula to intermittent condition. Thus, an alternative method for obtaining skewness and kurtosis of Morison force in intermittently submerged condition should be further investigated to eliminate the dependence on time simulation in frequency domain approaches.

Bibliography

[1] Åberg, S., Podgórski, K. & Rychlik, I., 2009. Fatigue damage assessment for a spectral model of non-Gaussian random loads. Probabilistic Engineering Mechanics, 24, 608–617.

[2] Amzallag, C., Gerey, J.P., Robert, J.L. & Bahuaud, J., 1994. Standardization of the rainflow counting method for fatigue analysis. International Journal of Fatigue. 16, 287-293.

[3] Anastasiou, K., Tickell, R.G. & Chaplin, J.R., 1982. The nonlinear properties of random wave kinematics. In: Proceedings of 3rd International Conference on the Behavior of Offshore Structure, USA, pp. 493–515.

[4] ASTM, 2005. ASTM E 1049-85: Standard Practices for Cycle Counting in Fatigue Analysis. West Conshohocken, PA, USA.

[5] Bae, Y.H., Kim, M.H., Yu, Q., 2014. The dynamic coupling effects of a MUFOWT (multiple unit floating offshore wind turbine) with partially broken blade. In: Proceedings of the Twenty-fourth International Ocean and Polar Engineering Conference, Busan, Korea, June 15–20, 317–324.

[6] Bannantine, J.A., Comer, J.J. & Handrock, J.L., 1990. Fundamentals of Metal Fatigue Analysis. Prentice Hall, Englewood Cliffs, New Jersey.

[7] Basquin, O. H. 1910. The Exponential Law of Endurance Tests. Page 625 of: American Society for testing of Materials, vol. 10. West Conshochocken: ASTM.

[8] Benasciutti, D. & Tovo, R., 2005. Cycle distribution and fatigue damage assessment in broad-band non-Gaussian random processes. Probabilistic Engineering Mechanics. 20, 115-127.

[9] Borgman, L.E., 1965. Wave forces on piling for narirow-band spectra. J. Water-ways Harb. Div. 91 (3), 65–90.

[10] Borgman, L.E., 1972. Statistical models for ocean waves and wave forces. Advanced Hydrodynamics. 8, 139.

[11] Braccesi C., Cianetti F., Lori G. & Pioli D., 2009. The frequency domain approach in virtual fatigue estimation of non-linear systems: The problem of non-Gaussian states of stress. International Journal of Fatigue, 31, 766-775.

[12] Brouwers, J.J.H. & Verbeek, P.H.J., 1983. Expected fatigue damage and expected extreme response for Morison-type wave loading. Appl. Ocean Res. 5 (3), 129–133.

[13] BSI, 2015. BS 7910: Guide to methods for assessing the acceptability of flaws in metallic structures, London, UK.

[14] Charkrabarti, S.K., 1980. Laboratory generated waves and wave theories. J. Waterw. Port, Coast. Ocean Eng. Div. 106 (3), 349–368.

[15] Cianetti, F., Palmieri, M., Braccesi, C. & Morettini, G., 2018. Correction formula approach to evaluate fatigue damage

induced by non-Gaussian stress state. Procedia Structural Integrity. 8, 390-398.

[16] Correia, J.A.F.O., Jesus, A.M.P., Moreira, P.M.G.P. & Tavares, P.J.S., 2016. Crack Closure Effects on Fatigue Crack Propagation Rates: Application of a Proposed Theoretical Model. Advances in Materials Science and Engineering. Vol 2016, Article ID 3026745, 11 page.

[17] Crandall, S.H. & Mark, W.D., 1992. Random vibration in mechanical systems. Academic Press. London, UK.

[18] Det Norske Veritas (DNV), 2011. DNV-RP-C203: Fatigue Design of Offshore Steel Structures. DNV: Oslo, Norway.

[19] Det Norske Veritas (DNV), 2012. DNV-RP-C103: Column-stabilised Units. DNV: Oslo, Norway.

[20] Ding, J. & Chen, X., 2014. Assessment of methods for extreme value analysis of non-Gaussian wind effects with short-term time history samples. Engineering Structures. 80, 75-88.

[21] Ding, J. & Chen, X., 2015. Fatigue damage evaluation of broad-band Gaussian and non-Gaussian wind load effects by a spectral method. Probabilistic Engineering Mechanics. 41, 139-154.

[22] Ding, J. & Chen, X., 2015. Moment-Based Translation Model for Hardening Non-Gaussian Response Processes. Journal of Engineering Mechanics, 142(2), 06015006.

[23] Dirlik, T., 1985. Application of computers in fatigue analysis. PhD Thesis, University of Warwick, UK.

[24] Donahue, R.J., Clark, H.M., Atanmo, P., Kumble, R. & McEvily, A.J., 1972. Crack Opening Displacement and the Rate of Fatigue Crack Growth. International Journal of Fracture Mechanics. Vol. 8, 209–219.

[25] Dowling, N.E., 1972. Fatigue Failure Predictions for Complicated Stress−Strain Histories. Journal of Materials JMLSA. 7(1), 71−87.

[26] Downing, S.D. & Socie, D.F., 1982. Simple rainflow counting algorithms. International Journal of Fatigue. 4(1), 31−40.

[27] Dowling, N.E., 2004. Mean Stress Effects in Stress−Life and Strain−Life Fatigue. 2nd SAE Brazil International Conference on Fatigue, Sao Paulo, Brazil, SAE Paper No. 2004−01−2227.

[28] Elber, W., 1971. The Significance of Fatigue Crack Closure. In: ASTM STP 486 Damage tolerance in aircraft structures. American Society for Testing and Materials.

[29] Fatemi, A. & Yang, L., 1998. Cumulative fatigue damage and life prediction theories: a survey of the state of the art for homogeneous materials. International Journal of Fatigue. 20(1), 9−34.

[30] Foreman, R.G., Keary, V.E. & Engle, R.M., 1967. Numerical Analysis of Crack Propagation in Cyclic−Loaded Structures. Journal of Basic Engineering. Vol. 89, 459–464.

[31] Forman, R.G. & Mettu, S.R., 1992. Behavior of Surface and Corner Cracks Subjected to Tensile and Bending Loads in Ti – 6Al – 4V Alloy. ASTM STP 1131, American Society for Testing and Materials, Philadelphia, PA, 519–546.

[32] Frendhal, M. & Rychlik, I., 1993. Rainflow analysis: Markov method. International Journal of Fatigue. 15, 265-272.

[33] Gall, D.S. & Hancock, J.W., 1985. Fatigue crack growth under narrow and broad band stationary loading.

[34] Gao, Z & Moan, T., 2007. Fatigue damage induced non-Gaussian bimodal wave loading in mooring lines. Applied Ocean Research. 29, 45-54.

[35] Gong, K. & Chen, X., 2014. Influence of non-Gaussian wind characteristics on wind turbine extreme response. Engineering Structures. 59, 727-744.

[36] Goodman, J., 1919. Mechanics Applied to Engineering. Longmans, Green and Co., London.

[37] Gray, T.G.F., 1992. Handbook of crack opening data (includes disk). Abington, Cambs: Abington Press.

[38] Griffith, A.A., 1920. The Phenomena of Rupture and Flow in Solids. Philosophical Transactions. 221, 163-198.

[39] Grigoriu, M., 1993. On the Spectral Representation Method In Simulation. Probabilistic Engineering Mechanics, 8, 75-90.

[40] Grigoriu, M., 1995. Applied Non-Gaussian Processes. PTR Prentice Hall, Englewood Cliffs, NJ.

[41] Gurley, K., 1997. Modelling and simulation of non-Gaussian processes.' PhD thesis, Dept. of Civ. Engrg. and Geological Sci., University of Notre Dame, Notre Dame, Ind.

[42] Hoh, H.J., Pang, H.L. & Tsang, K.S., 2016. Stress intensity factors for fatigue analysis of weld toe cracks in a girth-welded pipe. International Journal of Fatigue, 87, 279-287.

[43] Huston, W.B. & Skopinski, T.H., 1956. Probability and frequency characteristics of some flight buffet loads. NACA Technical Note 3733.

[44] Irwin, G.R., 1948. Fracture Dynamics. Fracturing of Metals, American Society for Metals, Cleveland, OH, 147–166.

[45] Irwin, G.R., 1956. Onset of Fast Crack Propagation in High Strength Steel and Aluminium Alloys. Sagamore Research Conference Proceedings, 2, 289–305.

[46] Isaacson, M. & Baldwin, J., 1990a. Measured and predicted random wave forces near the free surface. Appl. Ocean Res. 12 (4), 188–199.

[47] Isaacson, M. & Baldwin, J., 1990b. Random wave forces near free surface. J. Waterw. Port, Coast. Ocean Eng. 116 (2), 232–251.

[48] Isaacson, M. & Subbiah, K., 1991. Numerical simulation of random wave forces near the free surface. J. Offshore Mech. Arct. Eng. 113, 14–22.

[49] Jensen, J.J., 1990. Fatigue Analysis of Ship Hulls under Non-Gaussian Wave Loads. Marine Structures. 4, 279-294.

[50] Kanegaonkar, H.B. & Haldar, A., 1987. Non-Gaussian Response of Offshore Platforms: Fatigue. Journal of Structure Engineering. 113(9), 1899-1908.

[51] Kang, H.Y., Kim, M.H., Cho, J.Y., Kim, M.K., 2013. Time-domain hydroelastic simulations and structural analyses. In: Proceedings of the Twenty-third International Offshore and Polar Engineering, Alaska, USA, June 30–July 5, pp. 642–647.

[52] Klesnil, M. & Lukas, P., 1972. Influence of Strength and Stress History on Growth and Stabilisation of Fatigue Cracks. Engineering Fracture Mechanics. Vol. 4, 77–92.

[53] Kihl, D.P., Sarkani, S. & Beach, J.E., 1995. Stochastic fatigue damage accumulation under broadband loadings. International Journal of Fatigue. 17(5), 321−329.

[54] Kihm, F., Rizzi, S.A., Ferguson, N.S. & Halfpenny, A. 2013. UNDERSTANDIN HOW KURTOSIS IS TRANSFERRED FROM INPUT ACCELERATION TO STRESS RESPONSE AND ITS INFLUENCE ON FATIGUE LIFE. Proceedings of the 11th international conference on recent advances in structural dynamics, Pisa, Italy. July 1−3.

[55] Kim, J.J. & Kim, H.Y., 1994. Simple method for evaluation of fatigue damage of structures in wide−band random vibrations. Proceedings of the Institution of Mechanical Engineers, Part C Journal of Mechanical Engineering Science, 208(13), 65−68.

[56] Lawrance, A.J. and Lewis, P.A.W., 1985. Modelling and Residual Analysis of Nonlinear Autoregressive Time Series in Exponential Variables. Journal of the Royal Statistical Society. 47(2), 165−202.

[57] Lee, Y.L., Pan, J., Hathaway, R.B. & Barkey, M.E., 2005. Fatigue testing and analysis: theory and practice. 1st edition. Oxford, UK.

[58] Li, Y. & Kareem, A., 1993. Simulation of multivariate random processes: Hybrid DFT and digital filtering approach. Journal of engineering mechanics, ASCE, 119, 1078-1098.

[59] Lindgren, G. & Broberg, K.B., 2004. Cycle Range Distributions for Gaussian Processes - Exact and Approximative Results, Extremes, 7, 69-89.

[60] Lutes, L.D. & Larsen, C.E., 1990. Improved spectral method for variable amplitude fatigue prediction. Journal of Structural Engineering ASCE. 116(4), 1149-1164.

[61] Lutes, L.D. & Sarkani, S., 1997. Stochastic analysis of structural and mechanical vibrations. Englewood Cliffs: Prentice-Hall.

[62] Matsuishi, M. & Endo, T., 1968. Fatigue of metals subjected to varying stress, Japan Society of Mechanical Engineers. Jukvoka, Japan.

[63] Miner, M.A., 1945. Cumulative damage in fatigue. Journal of Applied Mechanics ASME. 67, 159-164.

[64] Moe, G., Crandall, S.H., 1978. Extremes of morison-type loading on a single pile. J. Mech. Des. 100 (1), 100–104.

[65] Mohammadi, S.F., Galgoul, N.S., Starossek, U. & Videiro, P.M., 2016. An efficient time domain fatigue analysis and its comparison to spectral fatigue assessment for an offshore jacket structure. Marine Structure. 49, 97-115.

[66] Morandi, A., Martinez, D. & Smith, C., 2004. STATISTICS OF TLP TENDON TENSION BEHAVIOUR DURING HURRICANE LILI. Proceedings of OMAE 23rd International

Conference on Offshore Mechanics and Arctic Engineering, Vancouver, British Columbia, Canada, June 20-25.

[67] Morrow, J., 1968. Fatigue Design Handbook, Pub. No. AE-4, Society of Automotive Engineers, Warrendale, PA.

[68] Murakami, Y., 1987. Stress intensity factor handbook. Vols. 1 and 2. Oxford: Pergamon Press.

[69] Newland, DE., 1984. An introduction to random vibration and spectral analysis. 2nd edition. Essex, England: Longmann Scientific and Technical.

[70] Newman, J. C., 1984. A crack opening stress equation for fatigue crack growth. International Journal of Fracture, 24, 131-135.

[71] Niesłony, A. & Böhm M., 2015, Mean Stress Effect Correction in Frequency-domain Methods for Fatigue Life Assessment. Procedia Engineering, 12(101), 347-354.

[72] Ochi, M.K., 1986. Non-Gaussian random processes in ocean engineering. Probabilistic Engineering Mechanics. 1(1), 28-39.

[73] Ochi, M.K. & Ahn, K., 1994. Probability distribution applicable to non-Gaussian random processes. Probabilistic Engineering Mechanics, 9, 255-264.

[74] Pajouhi, K. & Tung, C.C., 1975. Statistical Properties of Fluid Motion and Fluid Force in a Random Wave Field. Report No. 75-1. Center for Marine and Coastal Studies, North Carolina State Univ, Rayleigh, N.C.

[75] Park, J.B., Choung, J.M. & Kim, K.S., 2014. A new fatigue prediction model for marine structures subject to wide band stress process. Ocean Engineering, 76, 144-151.

[76] Peng, C., Mansour, A.M. & Sun, C., 2017. A damaged-based condensation method to condense wave bins for tendon fatigue analysis. Journal of offshore engineering and technology. 1(1), 33-39.

[77] Petrucci, G., Paola, M.D. & Zuccarello, B., 2000. On the characterization of dynamic properties of random processes by spectral parameters. Journal of Applied Mechanics. 67, 519–526.

[78] Petrucci, G. & Zuccarello, B., 2004. Fatigue life prediction under wide-band random loading. Fatigue & Fracture of Engineering Materials & Structures. 27(12), 1183-1195.

[79] Rice, J.R., 1972. Some Remarks on Elastic Crack-Tip Stress Fields. International Journal of Solids and Structures. Vol. 8, 751–758.

[80] Rice, J.R., 1989. Weight Function Theory for Three-Dimensional Elastic Crack Analysis. ASTM STP 1020, American Society for Testing and Materials, Philadelphia, PA, 29–57.

[81] Rizzi, S.A., Przekop, A. & Turner, T.L., 2011. On the response of a nonlinear structure to high kurtosis non-Gaussian random loadings. 8th International Conference on Structural Dynamics, Leuven, Belgium, July 4-6.

[82] Rooke, D.P. & Cartwrigth, D.J., 1976. The Compendium of Stress Intensity Factors. Pendragon House, Inc., Palo Alto, California, USA.

[83] Rychlik, I., 1987. A new definition of the rain-flow cycle counting method. International Journal of Fatigue. 9(2), 119-121.

[84] Rychlik, I., 1993. Note on cycle counts in irregular loads, Fatigue Fracture of Engineering Materials & Structures, 16(4), 377-390.

[85] Rychlik, I., 1993. On the 'narrow-band' approximation for expected fatigue damage. Probabilistic Engineering Mechanics. 8, 1-4.

[86] Rychlik, I., Lindgren, G. & Lin, Y.K., 1995. Markov based correlations of damage cycles in Gaussian and non-Gaussain loads. Probabilistic Engineering Mechanics, 10, 103-115.

[87] Rychlik, I., Johannesson, P. & Leadbetter, M.R., 1997. Modelling and statistical analysis of ocean-wave data using transformed Gaussian processes. Marine Structure, 10, 13-47.

[88] Sarkani, S., Kihl, D.P. & Beach, J.E., 1994. Fatigue of welded joints under narrow-band non-Gaussian loadings. Probabilistic Engineering Mechanics. 9, 179-190.

[89] Schijve, J., 2004. Fatigue of Structures andMaterials, Kluwer Academic Publishers, Burlington, Mass, USA.

[90] Schottler, J., Reinke, N., Holling, A., Whale, J., Peinke, J. & Holling, M., 2017. On the impact of non-Gaussian wind

statistics on wind turbines – an experimental approach. Wind Energy Science. 2, 1−13.

[91] Smith, K. N., Watson, P. & Topper, T. H., 1970. A StressStrain Function for the Fatigue of Metals. Journal of Materials ASTM, 5(4), 767−778.

[92] Spidsoe, N. & Karunakaran, D., 1997. Effects of Non−Gaussian Waves to the Dynamic Response of Jack−up Platforms. Marine Structures. 10, 131−157.

[93] Tada, H., Paris, P.C. & Irwin, G.R., 1973. The Stress Analysis of Cracks Handbook. Del Research Corporation, Hellertown, Pa.

[94] Tickell, R.G., 1977. Continuous random wave loading on structural members. Struct. Eng. 55 (5), 209–222.

[95] Tovo, R., 2002. Cycle distribution and fatigue damage under broad−band random loading, International Journal of Fatigue, 24, 1137−1147.

[96] Tung, C.C., 1974. Peak distribution of random wave−current force. J. Eng. Mech. Div. 100(5), 873–884.

[97] Tung, C.C., 1975. Statistical properties of the kinematics and dynamics of a random gravity−wave field. J. Fluid Mech. 70 (part 2), 251–255.

[98] Tung, C.C. & Huang, N.E., 1983. Statistical properties of the kinematics and dynamics of nonlinear waves. J. Phys. Oceanogr. 14, 594–600.

[99] Tung, C.C. & Huang, N.E., 1985. Covariances and spectra of the kinematics and dynamics of nonlinear waves. J. Geophys. Res. 90 (C6), 11911–11916.

[100] Tung, C.C., 1995. Effects of free surface fluctuations on total wave force on cylinder. J. Eng. Mechanics 121 (2), 274–280.

[101] Vanmarke, H., 1972. Properties of spectral moments with applications to random vibrations. Journal of the Engineering Mechanics Division, 98, 425–446.

[102] Walker, K., 1970. The Effect of Stress Ratio During Crack Propagation and Fatigue for 2024−T3 and 7075−T6 Aluminum. West Conshohocken, PA, 1−14.

[103] Wang, X. & Sun, J.Q., 2005. Effect of skewness on fatigue life with mean stress correction. Journal of Sound and Vibration, 282, 1231−1237.

[104] Winterstein, S.R., 1985. Non−normal responses and fatigue damage. Journal of Engineering Mechanics ASCE. 111(10), 1291−1295.

[105] Winterstein, S.R., 1988. Nonlinear vibration models for extremes and fatigue. Journal of Engineering Mechanics ASCE. 114(10), 1772−1790.

[106] Winterstein, S.R., Ude, T.C. & Kleiven, G., 1994. Springing and slow drift responses: predicted extremes and fatigue vs. simulation. Proceedings of the 7th International behaviour of Offshore structures BOSS, Cambridge, 3, 1−15.

[107] Wirsching, P.H. & Light, C.L., 1980. Fatigue under wide band random stresses. Journal of the Structural Division ASCE. 106(7), 1593-1607.

[108] Wolfram, J., 1999. On alternative approaches to linearization and Morison's equation for wave forces. Proc. R. Soc. A Math. Phys. Eng. Sci. R. Soc. Lond. 455, 2957–2974.

[109] Wolfsteiner, P., 2017. Fatigue assessment of non-stationary random vibrations by using decomposition in Gaussian portions. International Journal of Mechanical Sciences, 127, 10-22.

[110] Wöhler, A., 1870. Über die Festigkeitsversuche mit Eisen und Stahl. Zeitschrift für Bauwesen, 20, 73–106.

[111] Wu, Y., 1992. FATIGUE UNDER BROAD BAND RANDOM STRESS SPECTRUM. Proceedings of the 2nd International Offshore and Polar Engineering Conference, San Francisco, USA, 14-19, June. 301-305.

[112] Zhao, W. & Baker, M.J., 1992. On the probability density function of rainflow stress range for stationary Gaussian processes. International Journal of Fatigue. 14(2), 121-135.

[113] Zou, J. & Huang, E.W., 1999. Nonlinear and Non-Gaussian Effects on TLP Tether Responses. Proceedings of the Ninth International Offshore and Polar Engineering Conference, Brest, France, May 30 - June 4, 315-324.

감사의 글

2012 년도에 대학원에 입학한 이래, 어느 덧 박사 졸업 논문을 퇴고하는 시점이 왔습니다. 7 년 반 동안의 대학원 생활 속에서 제 연구 활동과 생활에 도움을 주셨던 분들께 감사의 인사를 짧게나마 올리고자 합니다.

먼저 제 석사 학위를 지도해 주셨던 양영순 교수님께 감사의 인사를 올립니다. 항상 조선해양 공학의 미래와 이를 대비하기 위해 새로운 분야에 대한 시도와 노력을 아까지 않으셨던 교수님의 모습에서 수많은 말보다 많은 가르침을 받았습니다.

그리고 제 박사 학위를 위해 많은 가르침을 주셨던 장범선 교수님께 감사의 말씀을 올리고 싶습니다. 연구실에 박사 과정으로 들어오기는 했지만, 구조 분야의 박사 과정으로서 요구되는 지식을 갖추지 못한 제게 장범선 교수님께서 관련 분야에 대해 공부할 수 있었던 많은 기회를 주셨기에 구조 분야에 박사로서 좋은 결실을 맺을 수 있었던 것 같습니다.

기나긴 대학원 생활을 같이 했었던 연구실 선후배 그리고 동기들이 있었습니다. 연구실 초반에 구조공학 이라는 생소한 분야에서 처음으로 박사 과정을 시작했을 때, 구조 해석의 기본과 연구 과제의 진행에 많은 도움과 가르침을 주셨던 동범이형, 운동 해석에 대해서 항상 든든하게 조언을 주셨던 기호형, 그리고 연구실 생활에 대해서 많은 도움을 주셨던 성욱이 형께 먼저 인사를 드리고 싶습니다.

그리고 제겐 동생이지만, 연구실 동기이자 졸업 선배로서 많은 조언과 도움을 주었던 연림이, 그리고 연구실 입학 동기로 5 년 반이라는 시간을 함께 해준 정두와 준환이 에게도 고맙다는 인사를 하고

싶습니다. 긴 연구실 생활 동안에 항상 함께 해주는 동기들이 있었기에 때로는 지치고, 힘들어도 서로가 위로가 되어 다시 힘을 낼 수 있었던 것 같습니다. 그리고 제 연구 활동과 과제 수행에 있어서 많은 도움을 주셨던 한상웅 선임님. 선임님께 과제 초기에는 다소 불친절하게 말씀을 드렸던 적도 있었는데, 제가 도움을 요청 드릴 때에는 항상 웃는 얼굴로 친절하게 대답해 주셔서 미안하다는 말씀과 감사하다는 말씀을 함께 드리고 싶습니다. 그리고 차후 저희 연구실에 기둥이 될 아니 이미 기둥이 된, 박사가 될 수 있는 충분한 인성을 갖춘 한백이에게 응원의 말을 남깁니다. 그리고 곧 졸업을 앞둔 채원이, 그리고 갓 연구실에 들어왔지만 누구보다도 연구실에 늦게까지 남아서 공부하고 있는 효철이에게도 응원의 메시지를 남깁니다. 끝으로 행정적 업무를 도와주셨던 경은 선생님, 타지에서 고생하고 계시는 트롱 박사님께도 감사하다는 말씀을 드립니다. 이외에도 다 적지 못했지만, 연구실을 앞서서 졸업한 다른 후배들과 동기 에게도 감사의 말을 드립니다.

무엇보다도 끝이 안보이는 대학원 생활에서 제게 묵묵히 응원과 격려를 해주셨던 제 아버지와 어머니 덕에 제가 힘을 얻고 졸업을 마무리 할 수 있었던 것 같습니다. 항상 제 선택에 대해서 인정해 주시고, 뜻하지 않은 어려움이 있을 때에 그럴 수 있다고 다독여 주셨던 부모님께 정말 큰 감사의 인사를 드리고 싶습니다. 제가 부모님을 존경하고 사랑하는 만큼 저도 두 분께 자랑스런 아들이도록 앞으로도 노력하도록 하겠습니다.

끝으로 제가 연구 활동을 웃으면서 할 수 있게 해준 제 단짝 세원이에게 고맙다는 인사를 남기고 싶습니다. 연인이자 같은 연구를 하는 대학원생으로서 누구보다 제 입장을 잘 이해해 주고, 졸업 논문을 준비하는 과정에서 졸업 주제 선정에 어려움을 겪고 힘들어 하고 있는 저를 세원이가 항상 따뜻하게 감싸 주었기에 끝까지 포기하지 않고

연구실 생활을 마무리 할 수 있었습니다. 그리고 세원이와 함께 발표 준비와 졸업 논문 준비에 지쳐 있었던 제게 물적 심적으로 응원과 격려를 해주셨던 장인, 장모님께도 정말 감사하다는 말씀을 올리고 싶습니다. 베풀어 주셨던 관심과 배려를 꼭 잊지 않고, 세원이와 함께 보답 드리며 살 수 있도록 노력하겠습니다. 제게 도움을 주셨던 모든 분들이 행복하시길 바라며 마치겠습니다.

김현진 올림

초록

선박과 해양 구조물들은 풍력, 파랑 및 조류와 같은 다양한 환경 하중을 생애 주기 동안에 반복적으로 받고 있다. 이와 같은 반복하중들은 그 크기가 항복 응력에 도달하지 않더라도, 구조물에 지속적으로 손상을 입히며 누적 손상도가 임계점에 도달할 때, 취약 부위에 피로 파괴 (fatigue failure) 현상이 발생할 수 있다. 극한 하중에 대한 구조물의 안전성을 평가하는 극한 강도 해석과는 달리, 피로 강도 해석의 경우 제품의 생애 주기 동안에 발생할 수 있는 모든 환경 하중을 고려해야 하므로, 많은 해석 시간을 요구한다는 특징이 있다. 보다 효율적으로 선박과 해양 구조물의 피로 수명을 평가하기 위해서 주파수 영역 기반의 스펙트랄 피로 해석 기법 (spectral fatigue analysis)이 꾸준히 연구되어 왔다.

스펙트랄 피로 해석 기법은 제품의 취약 부위인 핫 스팟(hot spot)에 작용하는 응력 스펙트럼으로부터 계산되는 스펙트랄 모멘트를 이용해서, 응력 진폭에 대한 확률 밀도 함수를 1 차적으로 추정한다. 그리고 이를 S-N 선도와 Miner 누적 식에 대입함으로써, 핫 스팟의 피로 수명을 추정한다. 현업에서는 과정을 단순화하기 위해서, 핫 스팟에 작용하는 응력들이 협대역 정규 과정을 따른다고 가정하며, 이 가정 하에 응력 진폭에 대한 확률 밀도 함수를 레일리 분포(Rayleigh distribution)로 이론적으로 유도할 수 있다. 하지만, 실제로 많은 엔지니어링 문제에서 하중의 비선형성, 구조물 형상의 복잡성 및 복합 하중과 같은 다양한 이유로 핫 스팟에 작용하는 응력이 위와 같은 가정에 위배되는 경우가 많다. 이러한 경우 기존 스펙트랄 피로 해석

기법은 피로 손상도를 과도하게 평가하는 경향이 있으므로, 이를 보완하고자 많은 연구가 이뤄졌다.

밴드폭 효과(bandwidth effect)는 핫 스팟 응력이 협대역 과정을 따르지 않기 때문에 발생한다. 밴드폭 효과가 피로 손상도에 미치는 영향을 반영하기 위해서, 다수의 연구 모델들이 제시되었다. 이들 중 몇 개의 모델은 성공적으로 밴드폭 효과를 다루는데 성공하였지만, 이들은 광대역 정규과정에서 응력 진폭에 대한 확률 밀도 함수와 이에 대응하는 피로 손상도를 유도하는 데 그치고 있으며, 광대역 비정규 과정으로 확장할 수 없다는 한계점이 있다.

비정규성(non-normality)은 밴드폭 효과와 마찬가지로 피로 손상도에 영향을 미치는 중요한 인자다. 비정규성을 다루기 위해서, 기존 연구 기법들은 광대역 정규 과정에서 유도된 응력 사이클의 확률 밀도 함수를 비선형 변환 함수(transformation function)를 통해 확장하는 방법을 제안하였다. 하지만, 이 변환 함수를 이용하기 위해서는 1 차적으로 가공된 응력 진폭에 대한 확률 밀도 함수가 아닌, 사이클에 대한 온전한 정보인 사이클을 구성하고 있는 피크(peak)와 밸리(valley) 또는 진폭 및 평균에 대한 결합밀도함수가 필요하다. 하지만, 기존에 광대역 정규 과정에서 제안된 확률 모델들 중 극히 일부만이 이 결합 밀도에 대한 근사 모델을 제공하고 있다. 더구나 이 근사 모델들도 부정확한 결합 밀도 함수를 제공하거나, 정확한 결과를 제공하더라도 이를 위해서 많은 시간을 요구하는 다차원 수치 적분이 필요하다는 한계점이 있다.

본 연구에서는 광대역 정규 과정에서, 사이클의 진폭과 평균에 대한 결합 밀도 함수를 예측하는 모델을 제안하였다. 응력 평균에 대한 정보를 왜곡하는 기존 모델을 보완하기 위해, 결합 밀도 함수를 응력 진폭에 대한 주변확률분포(marginal probability distribution)와 응력

평균에 대한 조건부 확률 분포 (conditional probability distribution)으로 분리하였다. 그리고 이 중 응력 평균에 대한 조건부 확률 분포에 대한 정교한 근사 모델을 회귀 분석을 통해 제안하였다.

광대역 정규 과정에서 제안된 결합 밀도 함수를 에르마이트 (Hermite) 변환 함수를 이용하여 광대역 비정규 과정으로 확장하였다. 비정규 과정에서 대상 모델을 통해 예측된 피로 손상도의 정확도는 이상화된 응력 스펙트럼을 통해 1 차적으로 검증하였다. 이를 기존 모델과 비교한 결과, 응력 평균에 대한 정보를 보정한 제안된 모델이 보다 정확하게 시뮬레이션 결과를 모사하고 있음을 확인하였다.

제안된 모델에 대한 적용성을 검토해 보기 위해, TLP tendon 에 대한 균열 해석과 풍력 터빈에 대한 피로 해석에 각각 제안된 모델과 기존 모델을 적용해 보았다. 두 개의 예제를 통해, 제안된 모델은 간단한 수식을 통해 진폭과 평균에 대한 결합밀도함수를 추정함으로써, 이상화된 예제와 마찬가지로 효율적으로 피로 손상도와 균열 성장 곡선을 예측할 수 있음을 확인하였다. 또한 기존 모델과 비교했을 때, 높은 정확도로 시뮬레이션 결과를 모사하고 있음을 확인하였다.

끝으로, 본 연구에서는 모리슨 하중 (Morison load)에 대한 선형화 계수에 대한 연구를 추가로 수행하였다. 비선형 항력으로 인해 모리슨 하중에 지배적인 영향을 받는 세장 부재들에 작용하는 핫 스팟 응력들은 광대역 비정규 과정을 따르며, 때문에 기존 스펙트랄 피로 해석 기법을 통해 피로 손상도를 예측할 수 없다. 이를 극복하기 위해, 선형화 계수가 제안되었다. 기존 선형화 계수는 물체가 완전히 물속에 잠겼을 때만 적용이 가능하며, 때문에 자유 수면 근처에 위치한 부재에는 적용할 수 없다는 한계가 있다. 이와 같은 부재는 자유 수면의 높낮이에 따라 하중이 불연속적으로 작용하므로, 이 부재에 적합한 선형화 계수를 새로이 유도할 필요가 있다. 본 연구에서는 간헐적 효과 (intermittent

effect)를 고려한 선형화 계수를 유도하고 이를 통해 모리슨 하중을 받는 부재의 피로 해석을 주파수 영역에서 수행하는 절차를 제안하였다. 선형화 계수를 통한 피로 해석은 비정규성을 반영할 수 없다는 한계는 있지만, 응력 스펙트럼을 계산하는 절차를 단순하게 할 수 있는 효용이 있음을 확인하였다.

Keyword : 피로 해석, 결합 밀도 함수, 랜덤 프로세스, 스펙트럼 , 에르마이트 함수, 비정규성, 밴드폭 효과

Student Number : 2014-30334